UNIVERSITEIT VAN PRETORIA
UNIVERSITY OF PRETORIA
YUNIBESITHI YA PRETORIA

Development of kinetic parameters for the leaching of phlogopite and characterisation of the solid residue

Cheri M. Favel

November 2020

UNIVERSITEIT VAN PRETORIA
UNIVERSITY OF PRETORIA
YUNIBESITHI YA PRETORIA

Development of kinetic parameters for the leaching of phlogopite and characterisation of the solid residue

by

Cheri M. Favel

14167990

A dissertation submitted in partial fulfilment
of the requirements for the degree

Master of Engineering (Chemical Engineering)

Department of Chemical Engineering

Faculty of Engineering, the Built Environment and Information Technology

University of Pretoria

Pretoria

November 2020

Development of kinetic parameters for the leaching of phlogopite and characterisation of the solid residue

Synopsis

The development of an appropriate solid-state kinetic model which represents the leaching process of phlogopite was investigated. Phlogopite samples were leached with nitric acid solutions of different concentrations, at different temperatures and for different reaction times. Leach liquors were analysed by ICP-OES for concentration, while the raw phlogopite and the acid-leached solid residues were analysed by XRF, XRD, ATR-FTIR, BET, TGA-DTG and SEM-EDS for characterisation to support the reaction rate model selection.

It was found that the reaction was diffusion-controlled and the model which represents one-dimensional diffusion through a flat plate (model D1) most accurately predicts the leaching behaviour. The observed activation energies and preexponential constants varied with initial acid concentration. The observed activation energies decreased from 98.8 – 88.9 kJ mol^{-1} as the initial acid concentration increased from 2 – 4 M, while the observed preexponential constants decreased from 3.30 x 10^{+12} – 2.30 x 10^{+11} min^{-1}.

Additional experiments were conducted at different temperatures, using different initial acid concentrations and over different reaction times to test the model. The experimental data points obtained ("testing data") were in agreement with the predicted values. Analyses of the solid residues also revealed complementary results with respect to the leaching model selection. The raw phlogopite was found to be highly crystalline (XRD). Therefore, the absence of defects in the lattice means that the motion of H^+ ions permeating into the lattice is restricted (Ropp, 2003; Schmalzried, 1995). This confirms that the leaching is internal diffusion-controlled since the mobility of constituents into the system is the controlling factor, and since the phlogopite particles are plate-like (SEM-EDS, BET) in shape, the use of the D1 model for one-dimensional diffusion through a flat plate is the recommended model to represent the leaching process. Furthermore, results obtained from the different analytical techniques were supportive of each other.

It was also found that the amount of acid consumed is inequivalent to the amount theoretically required. Using the theoretically required acid concentration (2.45 M) results in incomplete conversion (< 80 % according to Kgokong (2017)). When initial acid concentrations between 2.4 – 2.6 M were used, only 88 – 91 % conversion was obtained after 6 hours of leaching at 65 °C, leaving behind excess H^+ in solution. If fertiliser is the desired end product, it would be favourable to minimise the H^+ concentration of the leach liquor. Therefore, the leaching process should be optimised so that the acidity of the leach liquor is minimised while obtaining complete leaching of all cations from the phlogopite particles into solution. Furthermore, since the SiO_2 by-product is highly porous (surface area of 517 m^2 g^{-1}), its application in industrial adsorbents, catalysts, polymers, pigments, cement, etc. should be further explored.

Keywords: model, leaching, phlogopite, analyses, one-dimensional diffusion

Contents

List of Figures

List of Tables

Nomenclature

Symbol	Description	Units
a, b, c, s	Stoichiometric coefficients	-
m_0	Initial mass of raw phlogopite used for leaching	kg
m_t	Mass of dried solids leached after a specified time	kg
m_∞	Mass of the insoluble fraction of the original solid sample	kg
t	Time	s
$C_{i,t}$	Concentration of cation i in solution at a specified time	kg L^{-1}
$C_{i,TOTAL}$	Concentration of cation i present in the original sample	kg L^{-1}
V_t	Volume of leach liquor obtained after a specified time	L
V_{TOTAL}	Volume of leach liquor obtained after complete conversion	L
e, f, g, y, z	Constants	-
r_A	Rate at which reactant A is consumed	mol L^{-1} s^{-1}
C_A	Concentration of reactant A	mol L^{-1}
C_B	Concentration of reactant B	mol L^{-1}
k	Reaction rate constant	m^2 s^{-1} or s^{-1}
k_0	Pre-exponential constant/ frequency factor	s^{-1}
Ea	Activation energy	kJ mol^{-1} or J mol^{-1}
R	Universal gas constant	J mol^{-1} K^{-1}
T	Absolute reaction temperature	K
x	Distance travelled through product layer AB	m
l	Product layer thickness	m
D	Diffusion coefficient	m^2 s^{-1}
M_{AB}	Molecular weight of product layer AB	kg mol^{-1}
M_B	Molecular weight of reactant B	kg mol^{-1}
C	Concentration of B in AB	kg m^{-3}
C_{BP}	Concentration of B at interface P	kg m^{-3}
C_{BQ}	Concentration of B at interface Q	kg m^{-3}
$[H^+]$	Hydrogen ion concentration	mol L^{-1}
$[H^+]_0$	Hydrogen ion concentration of the initial acid before leaching	mol L^{-1}
$m_{i,t(s)}$	Mass of element i present in the acid-leached solid residues	kg
d	Interplanar spacing	Å or nm
n	Order of reflection (XRD)	-

Greek symbols

Symbol	Description	Units
α_G	Gravimetric conversion fraction	-
α_V	Volumetric conversion fraction	-
α_i	Conversion (recovery) fraction based on XRF results	-
ρ	Density of product layer AB	kg m^{-3}
λ	Wavelength of the incident x-radiation	Å or nm
θ	X-ray diffraction angle	radians
ν	Stretching vibrations	-
δ	Bending vibrations	-

1. Introduction

Phlogopite, also referred to as magnesium mica (Schipper & Cowan, 2018, p. 26), is a phyllosilicate mineral with the empirical formula $KMg_3AlSi_3O_{10}(F, OH)_2$ (Rieder *et al*., 1998). It contains valuable elements such as potassium, aluminium, magnesium, iron and silicon and may be contaminated by impurities such as calcium and titanium (Ganie, 2018), depending on the composition of the ore from which it was mined. The Mg^{2+}, Al^{3+}, Fe^{3+} and Si^{4+} compose layered silicate sheet structures which are weakly bonded by a cation interlayer (usually K^+) to supply the ideal cleavage. This enables the extraction of valuable cations by acid leaching (Kuwahara & Aoki, 1995; Mamy, 1970; da Silva *et al*., 2008; Woest, 2016).

Despite the presence of these valuable elements within the mineral, it is treated as waste material and is discarded in large quantities from various locations including the Palabora Igneous Complex (PIC) (van Straaten, 2002; Porteus, 2018; Schoeman, 1989). According to van Straaten (2002), about 1.5 million tons of phlogopite are discarded yearly at the PIC. Therefore, converting this abundance of waste material into economically viable products not only reduces the amount of waste accumulated during mining operations but also provides significant potential for profit.

Härkönen and Keiski (1984), Kaviratna and Pinnavaia (1994), Kuwahara and Aoki (1995), and Okada *et al. (2002)* have reported that leaching phlogopite with a strong acid and high temperatures results in the extraction of virtually all cations into solution, leaving only insoluble SiO_2. The porosity and applications of the SiO_2 residue have been studied by Deysel *et al*. (2020), Härkönen and Keiski (1984), Kraevskaya *et al*. (1985), Okada *et al*. (2002), and Wypych *et al*. (2005). da Silva *et al*. (2008) and Said *et al*. (2018) and reported that the solubility of K^+ from the interlayers of phlogopite in H_2O, is low. Acid extraction is required to extract all the K^+ from the layered structure. Therefore, to maximise the cation exploitation of phlogopite, the acid leaching process must be thoroughly understood.

The primary objective of this study was to develop a solid-state kinetic model which accurately represents the leaching process. Balland *et al*. (2010), Kalinowski and Schweda (1996), Lin and Clemency (1981), and Taylor *et al*. (2000) studied the cation extraction from phlogopite using mild conditions: pH 1-7, time in days or weeks, and low solid to liquid ratios. Their studies showed that potassium is not leached selectively; hence, for maximum potassium recovery, all the leachable cations should be removed, leaving only the insoluble SiO_2. Neither a kinetic model for leaching phlogopite with concentrated nitric acid and at high solid to liquid ratios nor a characterisation study of the leached products is available in the literature.

In this study, cation extraction was accelerated by leaching phlogopite samples with nitric acid solutions of different concentrations, over different reaction times and at different temperatures. Temperature and stirring speed were controlled using benchtop hotplate stirrers. All leaching experiments were conducted batchwise, in a closed system. The gravimetric data obtained from the acid-leached solid residues were used to determine the overall kinetics of the system. Leach liquors were analysed by ICP-OES for concentration, while the raw phlogopite and the acid-leached solid residues were analysed by XRF, XRD, ATR-FTIR, BET, TGA-DTG and SEM-EDS for characterisation and to support the reaction rate model selection.

The results are based on observations from experimental data and because internal diffusion limitations are present, the kinetics reported in this study are “apparent or disguised kinetics”. Therefore, the established kinetics should be used for reactions operated in the same regime as the “disguised regime” of this study to ensure accurate results (Fogler, 2006, p. 835).

The subsequent chapter details a literature review about phlogopite, the leaching process, modelling and characterisation techniques. Chapter 3 outlines the experimental work conducted in this study. The results are presented in Chapter 4, with a discussion to justify the significance of the results. Chapter 5 highlights the main conclusions of the work and recommendations for future scientific study. References and appendices are provided towards the end of the report.

2. Literature Review

This chapter aims to provide a comprehensive background of the dissertation topic. It includes a review of relevant literature to guide the reader in understanding the results and justification for the investigation. In this chapter, the raw material (phlogopite), and experimental methods (leaching and characterisation techniques) under investigation are described.

2.1. **Phlogopite**

2.1.1. Structure, appearance and composition

Phlogopite is the Mg end-member of the biotite mica group. Its structure is comprised of alternating silicon tetrahedral and octahedral (T-O-T) layers. It is characterised as a 2:1 clay since each octahedral sheet is sandwiched between two tetrahedral sheets. The octahedral sheets are occupied by divalent and trivalent cations (mainly Al^{3+}, Fe^{3+} and Mg^{2+}) and the tetrahedral sheets contain four O^{2-} ions bonded to Si^{4+} and Al^{3+} (Ciullo, 1996, p. 45; Grim, 1968). The layers are ~1 nm thick and are weakly adhered together by a cation interlayer of typically K^{+} to supply the ideal cleavage (Rieder *et al.*, 1998). The metal cations may be extracted from the structure through ion exchange of H^{+} from acids (Härkönen & Keiski, 1984; Kuwahara & Aoki, 1995; Mamy, 1970; da Silva *et al*., 2008; Woest, 2016). The general structure of trioctahedral micas such as phlogopite or biotite is illustrated in Figure 1 (Biedermann *et al*., 2014).

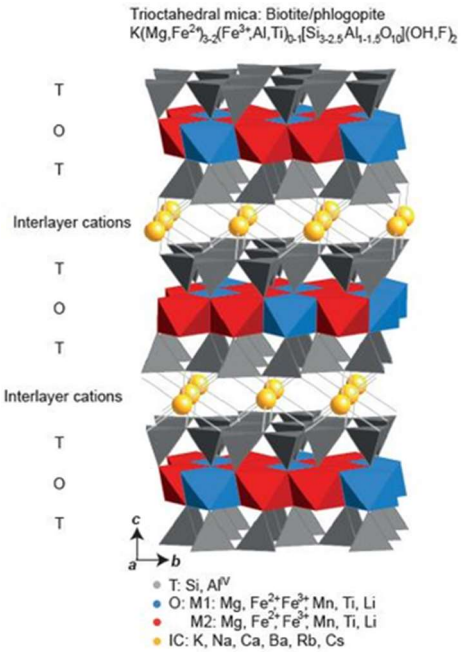

Figure 1: Schematic of the structure of phlogopite/biotite (Biedermann *et al*., 2014).

The K^{+}, Al^{3+}, Mg^{2+} and Fe^{3+} present in phlogopite may occur as oxides (Eriksson, 1982), however, the phlogopite may also contain some impurities. The precise chemical composition of phlogopite is region-specific and varies according to the geology of the location from which the ore was mined. Based on information gathered from Baksheev *et al*. (2016), Deysel *et al*. (2020), Kalinowski and

Schweda, (1996), Khalighi and Minkkinen (1989), Mamy (1970), Porteus (2018), Reguir *et al*. (2009), Schoeman (1989), da Silva *et al*. (2008), and Üçgül and Girgin (2002), Table 1 shows the composition range, with associated average values for some of the main constituents present in phlogopite.

Table 1: Composition ranges and average values of constituents present in phlogopite.

Phlogopite constituents	wt. % range	Average
SiO_2	38.7 – 43.0	40.6
K_2O	8.00 – 11.2	9.79
MgO	17.5 – 28.8	23.2
Fe_2O_3	0.00 – 10.0	3.31
Al_2O_3	9.88 – 24.9	15.0
TiO_2	0.00 – 3.26	0.93
CaO	0.00 – 5.51	0.64
P_2O_5	0.00 – 1.82	0.36
F	0.00 – 5.85	1.39
H_2O	0.00 – 3.91	1.57
MnO	0.02 – 0.16	0.07
Na_2O	0.11 – 2.04	0.59

2.1.2. Properties and uses

Phlogopite may be considered non-porous, with surface areas of ~1 $m^2 g^{-1}$ when untreated (Härkönen & Keiski, 1984). It is relatively non-hygroscopic, highly dielectric and alkali resistant with excellent thermal stability and ion-exchange capacity (Foster, 1960; Kraevskaya *et al*., 1985; da Silva *et al*., 2008). These properties allow the mineral to be exploited for various potential purposes ranging from joint filling in the construction industry to glass, paint and plastic manufacture (Ciullo, 1996, p. 47; del Rey-Perez-Caballero & Poncelet, 2000; Dye & Hartshorn, 1924; Friedman, 2019; Heckroodt, 1991; Kraevskaya *et al*., 1985; Verbeek, 2002).

Due to the presence of K and other plant nutrients, phlogopite may successfully be exploited in the fertiliser industry (da Silva *et al.*, 2008; Said *et al.*, 2018; van Straaten, 2002). In order to produce fertiliser, the potassium must be extracted from the phlogopite.

2.2. **Leaching**

Leaching is a chemical process involving the preferential dissolution of one or more constituents from the solid phase by contact with a solvent (Seader & Henley, 2006, p. 650; Treybal, 1980, p. 717). Three primary processes concerned with leaching operations include (a) solute dissolution, (b) separation of the solution from the insoluble solid residue, and (c) washing the solid residue to remove unwanted soluble material or to maximise the soluble material product yield (IAEA, 1993; Richardson *et al*., 2002; Seader & Henley, 2006). Leaching forms part of hydrometallurgy, whereby valuable metals are separated from mixtures of undesirable constituents and gangue by removing the metals as soluble salts (Apua *et al*., 2013; IAEA, 1993; Sahoo *et al*., 2001; Udupa *et al*., 1990; Whittington & Muir, 2000; Yoshida, 2003). The resultant solution is known as the leach liquor (Seader & Henley, 2006, p. 665; Woollacott & Eric, 1994, p. 329). Chemistry, processes and techniques associated with the leaching of ores are reviewed by Bautista (1974).

As described above, the extraction of metals from mineral ores generally occurs through heterogeneous processes (Sohn & Wadsworth, 1979). Many types of heterogeneous reactions exist, however, this study will focus on reactions in the form of equation 1 (Sohn & Wadsworth, 1979: 9),

$$a\mathrm{A}_{(\mathrm{solid})} + b\mathrm{B}_{(\mathrm{solvent})} \rightarrow c\mathrm{C}_{(\mathrm{leach\ liquor})} + s\mathrm{D}_{(\mathrm{insoluble\ solid})} \quad (1)$$

where a, b, c and s are stoichiometric coefficients. In a typical leaching operation, the solid to be leached (A) often contains soluble material and inert insoluble material (D). The solvent (B) is added to the mixture to selectively dissolve the solutes contained in A. The fluid product (C), or leach liquor, is a mixture of the solvent and dissolved solutes and should be separated from the solid product (D) (Adebayo, 2014). Härkönen and Keiski (1984), Kaviratna and Pinnavaia (1994), Kuwahara and Aoki (1995), Okada *et al*. (2002), and Woest (2016) have reported that leaching phlogopite (A) with a strong acid (B) and at high temperatures results in the extraction of virtually all cations into solution, leaving SiO_2 residue (D) and a leach liquor (C) with a pH < 0.

Okada *et al.* (2006) reported that the leaching rates of T-O-T minerals strongly depend on the nature of cations in the tetrahedral and octahedral sheets, the surface area of the solids being leached, and the ratio of expandable sheets. According to Härkönen and Keiski (1984), and Wypych *et al*. (2005), HNO_3 initially dissolves interlayer K^+ before penetrating the octahedral sheets occupied by Mg^{2+}, Al^{3+}, and Fe^{3+}. Temuujin *et al*. (2003) reported that the interlayer ions are preferentially leached and the ions in the tetrahedral sheets are leached less rapidly. This could be due to the fact that elements with higher dissolution rates are more rapidly extracted, and since the K^+ ions are weakly bonded to the interlayer of the phlogopite structure (Rieder *et al*., 1998), they are more prone to acid attack and are readily available for extraction. This is further confirmed by Kuwahara and Aoki (1995), who found that the increasing dissolution order of the elements present in phlogopite is $Si^{4+} < Al^{3+}$, $Mg^{2+} < Fe^{3+} < K^+$ when leached with HCl, and Kaviratna and Pinnavaia (1994) who found that acid attacked the phlogopite particles predominantly by an edge attack mechanism. Kalinowski and Schweda (1996) determined the dissolution kinetics of phlogopite in aqueous solutions of HCl and H_2SO_4 at various pHs (1 – 4) and room temperature and found that interlayer K^+ was preferentially released without significant modification of the cation content in the 2:1 layers.

2.2.1. Preparation of solids for leaching

The nature of the solids, the portion of soluble material and its distribution throughout the original solid, and the particle size of the original solid influences its preparation. The solvent may be inhibited by insoluble material of the particles, which obstructs solute-solvent contact, thereby delaying diffusion and extraction rates (Geankoplis, 1993, p. 724). This is common in various hydrometallurgical processes where metal salts are leached from mineral ores (Seader & Henley, 2006, p. 651). Therefore, in order to accelerate the leaching rate, the ores may require crushing and grinding which enhances the accessibility of the solvent to the soluble fraction. Grinding becomes unnecessary if the soluble material is widely distributed throughout the whole solid, or if the solid is bonded to a solution in which the soluble matter is dissolved. In the latter case, washing can simply be utilised (Geankoplis, 1993, p. 724; Seader and Henley, 2006, p. 641; Treybal, 1980, p. 719; Van Arsdale, 1953). Various grinding, milling, flaking and slicing techniques and their effects on particle properties are discussed in Barabaszová and Valášková (2013), Ciullo (1996), IAEA (1993), Porteus (2018), and Treybal (1980). Generally, finely ground particles (< 0.1 mm) are associated with increased costs, yet more rapid and thorough agitated leaching. Coarse grinding results in slower leaching with improved drainage, and thus, less washing is required. Therefore, the use of coarse particles reduces grinding costs and

simplifies filtration. Coarse solids are commonly leached in fixed beds by percolation (Basmadjian, 2007, p. 335; Derry, 1978; Schweitzer, 1979; Seader and Henley, 2006, pp. 652–653; Treybal, 1980, p. 731).

2.2.2. Leaching rates

Reaction rates, in general, are often expressed in terms of concentration according to equation 2 (Levenspiel, 1999), and chemical species are related by stoichiometry.

$$-r_A = kC_A^y C_B^z \tag{2}$$

A and B represent arbitrary reactants, r_A is the rate at which reactant A is consumed, CA and AB represent the concentrations of reactants A and B, respectively, and y and z are the reaction orders.

The use of concentration to study reaction rates is common in solution kinetics. However, it is not an accurate representation of reactivity in solid-state kinetics since the reaction is not homogenous and is non-isotropic (irregular distribution of reaction sites), therefore, reactivity varies throughout the sample (Khawam, 2007). Solid-state kinetics can more accurately be determined by studying the weight loss of a solid sample. Weight loss data can be converted to a standardised form known as the conversion fraction (α_G).

2.2.2.1. Conversion

Gravimetric (overall) conversion

For isothermal gravimetric analyses, the conversion fraction represents the progress of the reaction over time as shown in equation 3 (Khawam & Flanagan, 2006).

$$\alpha_G = \frac{m_0 - m_t}{m_0 - m_\infty} \tag{3}$$

where α_G represents the gravimetric conversion fraction, m_0 is the initial mass of raw phlogopite used for leaching, m_t is the mass of dried solids leached after a specified time (t), and m_∞ is the mass of the insoluble fraction of the original solid sample (i.e., the mass of solids remaining after complete conversion is obtained).

Elemental (cationic) conversion

The conversion of individual cations can be calculated using the fraction of cation (i) in solution at a specified time with respect to the total amount of that specific cation present in the original sample (i.e., the amount of that cation in solution after complete conversion is achieved) as shown in equation 4.

$$\alpha_i = \frac{C_{i,t} V_t}{C_{i,TOTAL} V_{TOTAL}} \tag{4}$$

$C_{i,t}$ is the concentration of element i in solution at time (t), V_t is the volume of leach liquor obtained at that time, $C_{i,TOTAL}$ is the concentration of i leached after complete conversion and V_{TOTAL} is the volume of leach liquor obtained after complete conversion.

Volumetric conversion

When gravimetric data is unavailable, then volumetric conversion (α_V) can be calculated from concentration data. α_V can be expressed in terms of the total elemental mass in solution at time, t with respect to the total elemental mass leachable after complete conversion is achieved. This is represented by equation 5,

$$\alpha_V = \frac{\Sigma C_{i,t} V_t}{\Sigma C_{i,TOTAL} V_{TOTAL}} \quad (5)$$

where i represents the individual cations in solution.

2.2.2.2. Modelling

Understanding reaction dynamics relies on the attainment of all kinetic parameters. For example, in order to design an efficient plant for the industrial-scale production of fertiliser from phlogopite, the leaching reaction must be thoroughly understood, and therefore, the solid-state kinetics must be determined. An effective method for obtaining kinetic parameters is through identifying suitable reaction models. Models are mathematical, theoretical representations of real phenomena which can be used to explain or predict system behaviours. They are approximations of experimental observations (Rogers, 2012). In solid-state kinetics, models can be used to develop rate equations. Currently, various models exist which represent solid-state kinetics, many of which are founded on mechanistic assumptions, while others may be empirical (Brown, 2005). The selected model should be substantiated by additional complementary analytical techniques (Khawam & Flanagan, 2005).

The rate laws of solid-state reactions are affected by the type of reaction mechanism occurring in the system. Šesták and Berggren (1971) proposed a combined differential equation form for the preliminary appraisal of possible mechanisms in solid-state reactions as shown in equation 6,

$$\frac{1}{k}\frac{d\alpha}{dt} = g(\alpha) = \alpha^e(1-\alpha)^f(-\ln(1-\alpha))^g \quad (6)$$

where e, f and g are constants.

Typical reaction mechanisms associated with solid-state kinetics include nucleation, geometric shape, diffusion and reaction order. Khawam and Flanagan (2006) derived models based on these mechanisms in terms of fractional gravimetric conversion and applied them to desolvation reactions. These models are listed in Table 2 and can be implemented in the current study to determine the kinetics of the leaching reaction. The derivations, classifications and theoretical backgrounds of these reaction models are given by Khawam and Flanagan (2006).

The simplest models are order-based since they resemble those employed in homogenous kinetics. For the order-based models, z = 0 in equation 2, while y = 0, 1, 2, or 3 (Khawam & Flanagan, 2006). The derivation of the nucleation models are more complex and are usually applied to crystallographic transition (Burnham *et al*., 2004); adsorption (Wu *et al*., 2005); crystallisation (Yang *et al*., 2005); decomposition (Graetz & Reilly, 2005); desolvation (Khawam & Flanagan, 2005); and hydration (Peterson *et al.*, 2005) reactions.

It should be noted that the diffusion models are identical in form to the diffusion-controlled shrinking core models through the ash layer (Levenspiel, 1999) for flat plates (D1), and cylindrical particles (D2), and are quite similar for spherical particles (D3/ D4). Similarly, the geometric contraction models are

representative of the reaction controlled shrinking core models for spherical particles (R3), cylindrical particles (R2) and flat plates (R1/ F0).

Table 2: Rate expressions for various solid-state reaction models (Khawam & Flanagan, 2006).

Model	Shorthand notation	Differential form $f(\alpha) = \frac{1}{k}\frac{d\alpha}{dt}$	Integral form $g(\alpha) = kt$
Nucleation models			
Power law	P2	$2\alpha^{(1/2)}$	$\alpha^{(1/2)}$
Power law	P3	$3\alpha^{(2/3)}$	$\alpha^{(1/3)}$
Power law	P4	$4\alpha^{(3/4)}$	$\alpha^{(1/4)}$
Avarami-Erofeyev	A2	$2(1-\alpha)[-\ln(1-\alpha)]^{1/2}$	$[-\ln(1-\alpha)]^{1/2}$
Avarami-Erofeyev	A3	$3(1-\alpha)[-\ln(1-\alpha)]^{2/3}$	$[-\ln(1-\alpha)]^{1/3}$
Avarami-Erofeyev	A4	$4(1-\alpha)[-\ln(1-\alpha)]^{3/4}$	$[-\ln(1-\alpha)]^{1/4}$
Geometric contraction models			
Contracting area	R2	$2(1-\alpha)^{1/2}$	$\left[1-(1-\alpha)^{1/2}\right]$
Contracting volume	R3	$3(1-\alpha)^{2/3}$	$\left[1-(1-\alpha)^{1/3}\right]$
Diffusion models			
1-D Diffusion	D1	$1/(2\alpha)$	α^2
2-D Diffusion	D2	$[-\ln(1-\alpha)]^{-1}$	$[(1-\alpha)\ln(1-\alpha)] + \alpha$
3-D Diffusion-Jander	D3	$\frac{\left[3(1-\alpha)^{2/3}\right]}{\left[2(1-(1-\alpha)^{1/3})\right]}$	$\left[1-(1-\alpha)^{1/3}\right]^2$
Ginstling-Broushtein	D4	$3/\left[2\left((1-\alpha)^{-1/3}-1\right)\right]$	$1-(2\alpha/3)-(1-\alpha)^{2/3}$
Reaction-order models			
Zero-order	F0/R1	1	α
First-order	F1	$(1-\alpha)$	$-\ln(1-\alpha)$
Second-order	F2	$(1-\alpha)^2$	$(1-\alpha)^{-1}-1$
Third-order	F3	$(1-\alpha)^3$	$0.5[(1-\alpha)^{-2}-1]$

The temperature dependence of the rate constant is usually represented by the Arrhenius equation (Fogler, 2006: 92),

$$k = k_0 e^{-\frac{Ea}{RT}} \tag{7a}$$

where k_0 is the pre-exponential (frequency) factor, Ea is the activation energy (in J mol^{-1}), R is the universal gas constant (8.314 J mol^{-1} K^{-1}) and T is the absolute temperature of the reaction (in K). Ganie and du Plessis (2015) found the activation energy for leaching phlogopite with HNO_3 to be 59.5 kJ mol^{-1} and the pre-exponential constant was 5.88 x 10^{-7} min^{-1}.

The Arrhenius equation can be rearranged into its linear form,

$$\ln k = \ln k_0 + \left(-\frac{Ea}{R}\right)\left(\frac{1}{T}\right) \tag{7b}$$

to simplify the establishment of kinetic parameters. k_0 can be calculated from the intercept of a lnk versus 1/T plot, and the activation energy can be calculated from the slope.

The kinetic triplet (k_0, Ea, and model) could, therefore, be determined experimentally using conversion data over time from several isothermal experiments. Conventional model-fitting methods could be

employed, whereby the experimental data points are compared to various reaction models and the model which most closely resembles or "fits" the experimental data is selected. The activation energy and pre-exponential constant can be calculated from this model (Khawam & Flanagan, 2006).

Diffusion Models

When leaching solutes from within a particle, the solvent rapidly progresses from the bulk solution to the particle surface where it diffuses into the particle. Thereafter, the solute dissolves into the solvent and progresses to the particle surface. This step often limits the rate of the total leaching process and is a function of various factors (particle porosity, effective diffusivity, tortuosity, etc.). Eventually, the solute is transferred to the bulk solution. If the solid is dissolved into the solvent solution, the mass transfer rate from particle surface to the bulk liquid is the controlling factor (Geankoplis, 1993, p. 725; Seader and Henley, 2006, p. 665; Smit, 2001, p. 9). Based on this mechanism, diffusion control models are expected to provide somewhat accurate predictions of system behaviours when leaching clay particles such as phlogopite.

Several studies have confirmed that the amounts of potassium extracted from mica materials during leaching and the boundary distance are linearly affected by the square root of the reaction time. This is indicative that the rate of exchange is diffusion-controlled (Chute & Quirk, 1967; Giletti & Anderson, 1975; Kalinowski & Schweda, 1996; Kuwahara & Aoki, 1995; Leonard & Weed, 1970; Lin & Clemency, 1981; Mamy, 1970; Mortland, 1958; Rausell-Colom *et al*., 1965; Reed & Scott, 1962; Taylor *et al.*, 2000; von Reichenbach, 1969; Woest, 2016).

Diffusion models are associated with the mobility of constituents in a system. Defects in solids enable solid-state reactions to occur, usually intramolecularly where motion is restricted or between crystal lattices (Bybkov, 2002; Ropp, 2003). According to Levenspiel (1999), the transport of reacting species from reaction sites could result in the formation of a product boundary layer that thickens as the reaction progresses, thereby decreasing the product formation rate. This is illustrated in Figure 2 (Booth, 1948), whereby a solid reactant (A) is attacked by a gas or liquid reactant (B) resulting in the development of product layer (AB) of thickness, l. The reaction proceeds due to diffusion through this layer.

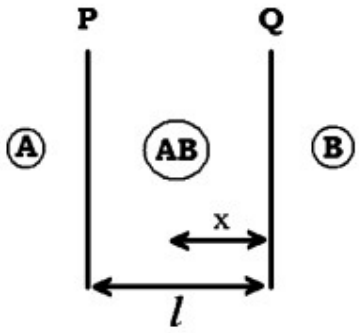

Figure 2: Illustration of one-dimensional diffusion through a flat plane (Booth, 1948).

In Figure 2, P and Q are the product layer interfaces and x represents the distance travelled through AB from Q in time, dt. The mass of B as it diffuses through AB to interface P (per unit area) in time, dt, is represented by equation 8,

$$-\mathrm{D}\frac{\mathrm{dC}}{\mathrm{dx}}\mathrm{dt} = \frac{\mathrm{M_B}}{\mathrm{M_{AB}}}\rho \mathrm{d}l \tag{8}$$

where D is the diffusion coefficient, M_{AB} and M_B are the molecular weights of AB and B, respectively, ρ is the density of AB, and C is the concentration of B in AB.

For a linear concentration gradient of B in AB,

$$\frac{\mathrm{dC}}{\mathrm{d}x} = -\frac{\mathrm{C_{BP}} - \mathrm{C_{BQ}}}{l} \tag{9}$$

where C_{BP} and C_{BQ} are the concentrations of B at interfaces P and Q, respectively. After substituting equation 9 into equation 8, followed by variable separation and integration, the parabolic rate law (equation 10) is formed (Booth, 1948),

$$l^2 = \mathrm{kt} \tag{10}$$

with

$$\mathrm{k} = \frac{2\mathrm{DM_{AB}}\left(\mathrm{C_{BP}} - \mathrm{C_{BQ}}\right)}{\mathrm{M_B}\rho}$$

According to Khawam and Flanagan (2006), diffusion occurs in one dimension for infinite flat planes, therefore, conversion (α) is directly proportional to the product layer thickness (l) as shown in equation 11,

$$\alpha^2 = \mathrm{k't} \tag{11}$$

with k' being constant. Equation 11 represents the one-dimensional diffusion (D1) model.

Since phlogopite are sheet (or phyllo) silicates, they have a flat platy morphology (Benedictus *et al*., 2008; Deer *et al*., 1992) and can, therefore, be described by one-dimensional diffusion. Diffusion model D2 is applied to cylindrical particles where only radial diffusion occurs (two-dimensional), and models D3 and D4 represent diffusion through spherical particles (three-dimensional).

Statistical Analyses

The coefficient of determination (R^2) is a statistical measure of the proportion of the dependent variable variance predicted from the independent variable(s). If the regression function is to be used for making predictions, it is preferable to have a high R^2 value which means that there is a smaller variation in the data (Joseph, 2019; McDonald, 2020). Goodness of fit can also be explained using the 1:1 line, whereby only one specific linear correlation between the predicted and observed values is considered (Wright & Stone, 1999).

2.2.2.3. Factors influencing the rate of extraction

Various factors may be responsible for limiting the overall rate of extraction during leaching, which ultimately influences the equipment selected for the process operation. The primary factors for consideration are listed below (Chezom *et al*., 2013; Kim, 2002; Richardson *et al*., 2002; Sethurajan *et al*., 2019; Tiwari *et al*., 2015).

Temperature

An increased temperature usually results in increased solubility of solutes and an increased diffusion coefficient, thereby increasing the extraction rate (Richardson *et al*., 2002; Treybal, 1980, p. 719). As shown by the Arrhenius equation (equation 7a), temperature has an exponential effect on the reaction rate. However, the temperature should be limited in order to avoid undesirable side reactions (Treybal, 1980; 719; Richardson *et al.*, 2002).

Okada *et al* (2002) reported an accelerated leaching rate as temperature was increased from 5 – 150°C. It took Favel (2018) 70 minutes longer to completely extract the soluble matter from within the phlogopite at 65 °C as opposed to 75 °C. Üçgül and Girgin (2002) achieved maximum swelling during chemical exfoliation of phlogopite at room temperature for 30 hours as opposed to 70 minutes when the temperature was increased to 60 °C. The material began decomposing for temperatures > 60 °C, and completely lost its characteristics above 80 °C. Härkönen and Keiski (1984) reported a 44 % increase in K recovery for a temperature increase from 25 °C to 100 °C in less than 2 hours. According to Kuwahara and Aoki (1995), ion dissociation increases with an increase in temperature, resulting in maximised metal recovery from the octahedral layer and the interlayer. Woest (2016) reported that temperature has a more significant influence over the leaching process than other factors. It affects the selectivity (∼25 – 45 % at 30 – 50 °C, respectively) and recovery of K (50 – 90 % at 30 – 50 °C, respectively). The overall conversion when leaching phlogopite with HNO_3 increases drastically from ∼22 % at 30 °C to ∼80 % at 50 °C (Woest, 2016).

Solvent

The effectiveness of leaching processes are typically characterised by the ability of a chemical reagent to solubilise and extract elements from a particle in the solid phase (Mgbeahuruike *et al.*, 2019), therefore, the type of leaching acid used, and its concentration should carefully be considered. The most suitable leaching solvent should be selective, with sufficiently low viscosity to enable free circulation. As the solute concentration increases within the solvent, the leaching rate progressively decreases due to a reduction in the concentration gradient and an increase in the solution viscosity (Richardson *et al.*, 2002).

da Silva *et al.* (2008) reported that the efficiency of potassium extraction in acidic media (0.01 M HNO_3), for different particle sizes, were around three times higher than the same process run with distilled water. According to Castilhos and Meurer (2001), acids can improve mineral weathering and make the K^+ release easier. Common acidic solvents used to leach phlogopite include HCl, HNO_3 and H_2SO_4 (Härkönen & Keiski, 1984; Okada *et al.*, 2005). According to Okada *et al.* (2005), H_2SO_4 was the most effective acid for leaching chlorite, followed by HNO_3 and then HCl. Härkönen and Keiski (1984) found that leaching phlogopite with HNO_3 yielded silica products of greater surface areas than those produced when the other acids were used. This was further confirmed by Venter (2015), who compared the effects of HNO_3, aqua regia and HCl on the surface areas of the leached products. She found that aqua regia and HNO_3 were more effective than HCl and yielded similar surface area values. According to Kaviratna and Pinnavaia (1994), the crystallinity of 2:1 structures decreases with acid treatment, while the BET surface areas increase. Woest (2016) reported that HNO_3 achieved superior cationic conversions and potassium selectivity compared to HCl, H_2SO_4, citric acid and acetic acid when leaching phlogopite.

Woest (2016) also found that SiO_2 with higher surface areas were produced with higher acid concentrations, however, the acid concentration effects on the recovery of K is less significant than the temperature effects. Complimentary results were found by Lammers *et al.* (2017) who observed

increased muscovite dissolution rates with increased pH within the temperature range of 100 – 280 °C, however, the rates showed minimal variation with pH above 150 °C. This is somewhat justified by Kalinowski and Schweda (1996), who reported that the dissolution rates of micas exhibit fractional reaction orders with respect to hydrogen ion activity. Okada *et al.* (2002) also achieved improved leaching with higher acid (HNO_3) concentrations (> 1M) with all components, except SiO_2 completely leached from the product. Furthermore, acid concentration influences the chemical exfoliation of phlogopite (49-fold increase in swelling after 30 hours with an increase in acid concentration) (Üçgül and Girgin, 2002). According to Temuujin *et al.* (2003), the acid concentration exhibits a less prominent influence as the concentration increases. This may be due to internal mass transfer limitations of the products or inhibition effects of extracted ions in solution.

The presence of various ions (K, Cs, Rb, NH_4) within the leaching acid may inhibit the discharge of K^+ from the interlayer, however, others (Na^+, H^+) may induce potassium diffusion (Mamy, 1970). Extraction could be suppressed by the formation of Fe and Al complexes during leaching, which may inhibit internal diffusion rates of products and reactants (Kuwahara & Aoki, 1995).

Particle size

A reduction in particle size increases the mass transfer rate both internally (reduced solute diffusion travel distance within the solid) and externally (increased solid-liquid interfacial area). Very fine particles may remain in suspension with minimal agitation, however, they are more difficult to separate and wash due to their low settling velocities and their large surfaces (Derry, 1978; Richardson *et al*., 2002).

According to Ross and Rich (1973), thicker particles are more subject to layer deformation and bending, unaccompanied by splitting, thereby increasing K^+ substitution and decreasing selectivity. They also found that thinner particles were more prone to splitting rather than bending, which led to improved K^+ selectivity. In addition, they also documented that particle size and the extent of K^+ exhaustion may influence the ability of K^+ to be resorbed into the phlogopite. They concluded that the K^+ sorption rate is greater for larger particles with complete K^+ depletion over smaller, partially depleted particles.

The amount of K-depleted interlayers on particles increases with a decrease in particle size (Gilkes & Suddhiprakarn, 1975; Rausell-Colom *et al*., 1965). da Silva *et al* (2008) found that leaching finer fractions of phlogopite (-37 µm) resulted in more than double the extraction efficiency when compared to fractions +37 µm. They suggested that this is due to the higher surface areas associated with the finer particles. However, Kalinowski and Schweda (1996) reported contradictions of direct proportionality between the dissolution rates of micas and their total surface areas.

Härkönen and Keiski (1984) found very slight differences in the recovery of K in the leach liquor for different grain sizes smaller than 550 µm. This suggests that the particle size of phlogopite, within a certain range, has a minimal effect on extraction rates. Similar results were obtained by Woest (2016), who leached particles smaller than 250 µm with HNO_3.

Solid:liquid (S:L) ratio

Solid:liquid ratios are often used in extractive metallurgy to quantify the leachate volume in relation to the solid sample proportion, usually in units of g mL^{-1} or kg L^{-1} (Tiwari *et al*., 2015). The effect of the S:L ratios on the leaching rate can generally be related to acid concentration effects. An increase in the volume for the same molar amount of H^+ ions would enable the solvent to accommodate more

extracted cations in solution with a reduced effect on solution viscosity due to dilution, which would improve mixing, and thus, external mass transfer diffusion rates. Since there would be fewer cations occupying each unit of volume in the solution, the concentration gradient between the particles and the solvent would be greater than that of a more saturated solution (Richardson *et al*., 2002, p. 503).

According to Kuwahara and Aoki (1995), extraction rates may be improved when using larger volumes of leaching solutions. They suspended 20 mg phlogopite in 100 mL or 20 mL leaching solutions and found incongruent dissolution, with the release order Mg < Fe < K, and Si < Al (for 100 mL experiments), and virtually congruent release rates of all elements, excluding K (for 20 mL experiments). Venter (2015) and Woest (2016) also found that leaching improved with larger volumes, however, the effect was found to be minimal or negligible. Woest (2016) observed that leaching phlogopite with HNO_3 (5.8 M), at 50 °C and with an S:L ratio of 0.1 g mL^{-1} resulted in a potassium recovery of > 98 %, and overall gravimetric conversion of 85 %. He also observed that by doubling the mass of phlogopite used (i.e., S:L = 0.2 g mL^{-1}), the potassium recovery was increased by only 2 %, indicating that the S:L ratio has a minimal or negligible effect on the leaching rates. Similar results were obtained by Venter (2015) who leached phlogopite with different acids using different S:L ratios (0.025, 0.05 and 0.1 g mL^{-1}). She found that leaching 20 g phlogopite with 200 mL acid (S:L = 0.1 g mL^{-1}) produced silica products with slightly higher surface areas than those obtained from the other S:L ratios. Üçgül and Girgin (2002) reported that S:L ratios for chemical exfoliation tests on phlogopite were of minor importance in comparison to acid concentration, temperature and reaction time.

Fluid agitation

Solvent agitation affects the eddy diffusion and thus, the external mass transfer rate (from solid surface to the bulk solution). It also prevents sedimentation, distributes the temperature throughout the solution and the interfacial surface is utilised more effectively. Stirring must be carried out correctly in order to maximise the solid-liquid contact (Mgbeahuruike *et al*., 2019; Richardson *et al*., 2002). Based on experience, the degree of agitation necessary for the leaching of phlogopite has a minimal impact on the reaction rate. Different stirring speeds are required for different reactor and stirrer types and sizes. Sufficient agitation is achieved when all particles are observed to circulate the reactor, without settling (Richardson *et al.*, 2002). Woest (2016) found that when leaching phlogopite with HNO_3, the agitation had no major influence on the recovery of K into solution.

2.3. **Characterisation techniques**

Analytical models are quantitative in nature and are used to make estimated predictions of system behaviours. To ensure that the selected model is expressed with sufficient precision, it should be substantiated by additional complementary analytical techniques including spectroscopy, XRF, XRD, microscopy, etc. (Baedecker, 1987; Khawam, 2007). These “model checkers” are required to ensure the analytical model is well-formed, so it can provide a reliable representation of the experimental procedure. Some common analytical techniques used for characterising sample materials are described below.

2.3.1. Inductively coupled plasma optical emission spectroscopy (ICP-OES)

ICP-OES is a trace-level analytical technique capable of identifying and quantifying elemental compositions of samples based on their characteristic optical emission spectra and the intensities of

these lines. The sample being analysed (usually liquid) is nebulised before being injected into the plasma (usually Ar) which atomises the test sample and excites the atoms (Boss & Fredeen, 2004; Skoog *et al*., 2007, p. 266).

2.3.2. X-ray fluorescence (XRF)

The instantaneous emission of absorbed electromagnetic radiation by an ionised atom is termed 'fluorescence', or 'x-ray fluorescence' when x-rays are used as the electromagnetic source. X-ray fluorescence (XRF) spectroscopy is an effective non-destructive technique used for the qualitative and quantitative determination of elements in a sample. Characteristic x-ray spectra are generated by irradiating a sample with a beam of primary x-rays. The emitted energy and its corresponding intensity are respectively dependent on the atomic number of the atom and its concentration within the sample (Khandpur, 2006). XRF has been employed extensively in the mineralogy industry to determine the chemical compositions of various materials (Baedecker, 1987).

2.3.3. X-ray diffraction (XRD)

XRD is a non-destructive analytical technique used for characterising crystalline materials by providing information about the crystallographic structure, physical properties and chemical composition of a sample. In an XRD analysis, a monochromatic beam of x-rays irradiates a sample over a variable incident angle range. Interaction of incident x-rays with atoms in the sample causes diffraction of the x-rays according to Bragg's Law (equation 12). Interference of the diffracted radiation is detected, resulting in the formation of diffractograms which are plots of intensity or counts as a function of the angle between the incident beam and the diffracted beam (2θ). Constructive interference of diffracted beams results in the formation of diffractogram peaks. The peak intensities depend on where atoms occur within the lattice planes and are proportional to the fraction of the material in the mixture. Consequently, the diffractograms are fingerprints of periodic atomic arrangements within a sample. The technique can be used to identify and quantify phases occurring within a material, to determine the crystallinity of a material (structure, quantity and crystallite size), and to determine unit cell size and lattice parameters (Khandpur, 2006; Qiao *et al*., 2017; Skoog *et al*., 2007).

XRD patterns of layered silicates generally display peaks at 2θ angles corresponding to (00*l*) basal reflections. The primary peak of phlogopite corresponds to a (001) basal reflection at a 2θ value of ~10.1° (Co Kα) (Brindley, 1952). The general XRD pattern of phlogopite is presented in Figure 3.

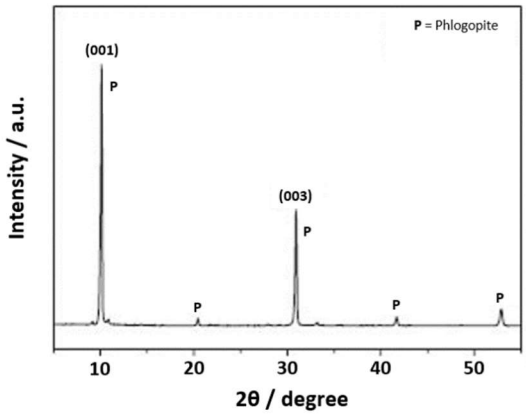

Figure 3: XRD pattern of raw phlogopite, redrawn from (da Silva *et al*., 2013).

High crystallinity would result in a high degree of constructive interference and thus, a large amplitude of the reemitted x-rays. Consequently, the intensity of XRD peaks is considered to be proportional to the crystallinity (Cullity, 1956). The position of the peaks can be related to the interplanar spacing (d), which is the fundamental repeating span between the perpendicularly stacked 2:1-layered structure by the Bragg equation,

$$n\lambda = 2d\sin\theta \tag{12}$$

where n is the order of reflection (n = 1), the diffraction angle (angle between the diffracted beam and the transmitted beam) is 2θ (in radians), and λ is the wavelength of the incident x-ray (0.179 Å for CoKα) (Cullity, 1956, p. 84). Therefore, a shift of the primary peak to larger angles corresponds with a decrease in interplanar spacing, and vice-versa.

2.3.4. Attenuated total reflectance Fourier transform infrared spectroscopy (ATR-FTIR)

Infrared (IR) spectroscopy is undoubtedly one of the most valuable and convenient analytical techniques available for scientific research. Virtually any sample, regardless of state or chemical composition, may be studied with a sensible sampling technique. Therefore, it has proven effective for the determination of local cationic environments and fine structural features (Besson & Drits, 1997) and is commonly used as a complementary technique for various analysis methods including XRD when investigating clay minerals (Madejová & Komadel, 2001).

Infrared absorption by a sample emerges due to the vibrations of its constituent atoms after being struck by a beam of infrared radiation. The frequencies of these vibrations are functions of the mass of the atoms, the restraining forces of the bonds, and the structural geometry. The resultant spectrum of absorption frequencies is a characteristic property of the mineral which suffices as a fingerprint for its identification and provides distinctive information on the structural features of the sample (Farmer, 1974; Stuart, 2004). Fourier-transform infrared (FTIR) spectrometers continuously detect transmitted energies using interferometers and swift Fourier transformation of the interferogram into a spectrum (Russell & Fraser, 1994).

Researchers have extensively exploited the use of infrared spectroscopy in mineralogy. As a result, a plethora of relationships have been established between structure, composition and IR spectra making identification of individual absorption bands simpler, faster and reliable (Besson & Drits, 1997). Variations in positions and amounts of IR absorption bands are often utilised to identify structural changes in a sample. The relationship between absorption spectra and sample structure is determined based on the atomic displacements pertaining to each vibrational mode, which can be determined by relating empirical observations to theoretical aspects of species similar in structure. The shape and position of the vibration band will be altered based on elemental substitutions within the sample structure. The position of the band shifts depends on the weights and bonding behaviour of the substituted species (Beran, 2002).

The vibration bands of mica group minerals are generally distinguished by vibrations in the hydroxyl group region and the lattice vibrations of the $Si(Al)O_4$ tetrahedra, the octahedral cations, and the interlayer cations (Beran, 2002). Common absorption bands associated with the IR spectra of phlogopite and their corresponding wavenumber positions were obtained from various sources and are summarised in Table 3 (Farmer & Russell, 1964; Jenkins, 1989; Procópio *et al*., 2020; Sijakova-Ivanova & Cukovska, 2016; Šontevska *et al*., 2008; Stubičan & Roy, 1961; Vedder, 1964; Wypych *et al*., 2005; Zeller & Juszli, 1975).

Table 3: Observed absorption bands for phlogopite in the fingerprint region of the mid-IR spectrum.

Wavenumber (cm^{-1})		Band intensity	Tentative assignment
Range	Average		
1011 - 995	1003	VS	*v*(Si–O–Si)
977 - 915	954	S – VS, SH	*v* (Si–O–Si)
899 - 799	823	W – S	*v*(Al–O–Al)
748 - 725	731	VW – M, SH	*v*(Al–O–Si)
708 - 672	690	VW – S	*v*(Si–O–Si)
536 - 495	511	SH, VS	δ(Si–O–Si)
480 - 450	464	S – VS	δ(Si–O–Si)

v: stretching; δ: bending, W: weak; VW: very weak; M: medium; S: strong; VS: very strong; SH: shoulder

2.3.5. Brunauer-Emmett-Teller (BET) Analysis

Physical properties (i.e. surface area and porosity) influence the quality and character of solid-phase materials (Thommes *et al.*, 2015). A BET analysis could prove valuable when studying reactivity, dissolution, separation or any other properties associated with surface area (Michot & Villiéras, 2013). The BET specific surface area (SSA) is calculated based on the amount of adsorbate gas (usually N_2) corresponding to a monomolecular layer on a sample's surface measured at the boiling point of the adsorbate (-196 °C for N_2). The technique is founded on the BET theory (Brunauer *et al*., 1938). To ensure the required accuracy and precision during BET analysis, vapours and gases which had previously been physically adsorbed onto the surfaces of particles during treatment, handling and storage must be removed. The process of removing moisture and any other extraneous materials from the surface of the particles is called degassing or out-gassing. Ultimately, the BET analysis ensures a rigorous SSA assessment of a sample by gaseous adsorption as a function of relative pressure (p/p_0), presented as adsorption-desorption isotherms (Micromeritics, 2016).

The shapes of N_2 adsorption-desorption isotherms are useful when investigating pore morphology of the sample material (Bardestani *et al*., 2019; Zeng *et al.*, 2017; Wang *et al.*, 2018; Chen *et al.*, 2018). Pores are commonly characterised by the International Union of Pure and Applied Chemistry (IUPAC) classification standard (Sing, 1985), which is predicated on the capillary condensation theory and physical adsorption characteristics (Tuller *et al*., 1999; Rouquerol *et al.*, 1994; Brunauer *et al*., 1938). According to the IUPAC classification standard, there are six types of N_2 adsorption isotherms (Figure 4). Furthermore, pore structures can be classified according to pore size (diameter or width) as either micropores (<2 nm), mesopores (2-50 nm), or macropores (>50 nm) (Rouquerol *et al*., 1994).

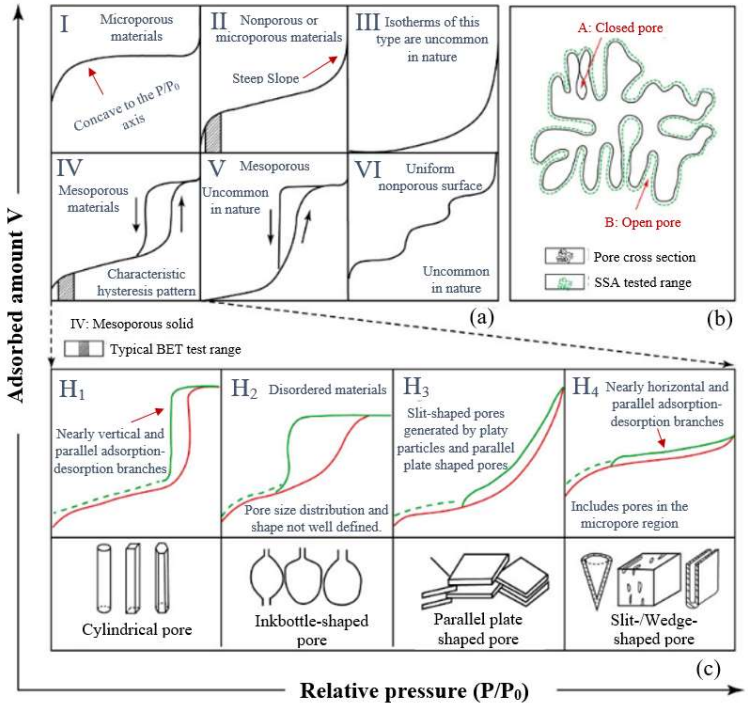

Figure 4: Adsorption isotherms and pore types: (a) IUPAC classification of adsorption isotherms; (b) illustration of pore cross-section; (c) IUPAC classification of hysteresis loops with corresponding pore shapes. (Redrawn from Wang *et al*. (2020)).

2.3.6. Thermal analysis (TGA-DTG)

Crystal materials exhibit different heat absorption and release properties when exposed to temperature changes. Relationships can be established between the physicochemical properties of a sample and changes in temperature. One of the main thermal analytical techniques is thermogravimetric analysis (TGA).

In a TGA, the mass changes of a sample are recorded in response to a change in temperature in a controlled atmosphere as a function of time or temperature. The resulting plot is called a thermogram or a thermal decomposition curve. The information provided from a TGA is quantitative but limited to oxidation and decomposition reactions as well as some physical processes (desorption, vaporisation and sublimation). The analysis requires precise weight, temperature and temperature change measurements. Derivative curves may reveal information that is not detectable in the ordinary thermogram. Derivative thermogravimetry (DTG) represents the rate of change in mass (dm/dt) as a function of temperature and could be used to distinguish the most apparent points where the greatest mass changes occur (Qiao *et al*., 2017; Skoog *et al*., 2007).

2.3.7. Field emission gun scanning electron microscopy (FEG-SEM) and energy-dispersive x-ray spectroscopy (EDS)

Scanning electron microscopy (SEM) is an analytical technique used for studying the physical nature of surfaces. It involves scanning a focused beam of high-energy electrons across the surface of solid sample material. Secondary and backscattered electron signals derived from electron-sample interactions are detected, providing detailed high-resolution images of the sample's external

morphology with over 50,000 times magnification enabling the observation of sub-micron-scale features. Energy-dispersive x-ray spectroscopy (EDS or EDX) can be used to identify and quantify composition information by absorbing emitted x-rays from ionisation. The absorbed x-rays are converted into electrical voltages of proportional size, which are characteristic of the element (Severin, 2004). SEM-EDS is commonly used to characterise material shapes and surface details including surface defects, stains and residues or contaminants on or within the sample, to assess reaction interfaces and degradation mechanisms, and to reveal spatial variations in chemical compositions.

3. Experimental

This chapter provides a detailed description of the processes involved in conducting the experimental work. It includes a description of the apparatus and materials used to conduct the experiments, a planning section that provides an outline of the experimental design showing the dependent and independent variables, and the methods used to conduct the experiments. Sufficient information is provided to enable a reader to repeat the work.

3.1. **Apparatus**

A measuring cylinder, micropipette, volumetric flask, burette, beakers and a RADWAG PS 6000/C1 laboratory scale were used for measurements. All leaching reactions were conducted batchwise (beakers with magnetic stirrers for mixing), with plastic wrap seals to avoid solution evaporation during experiments. Temperature and stirring speed were controlled using WiseStir MSH-20D hotplate stirrers. Vacuum filtration was performed using a Büchner funnel, Büchner flask, tubing, a rubber adapter and filter paper for each experiment. Wet filter cakes were dried in a Labotec EcoTherm laboratory oven.

Sample concentrations were determined using a Spectro-Acros ICP-OES analyser (for liquid samples) and a Thermo Fisher ARL Perform'X Sequential XRF instrument with Uniquant software (for solid samples). XRD was performed using a PANalytical X'Pert Pro powder diffractometer. Absorbance spectra were recorded on a Perkin Elmer Spectrum 100 using the single reflection ATR diamond crystal. N_2 physisorption analyses were performed using a Micromeretics TriStar II Surface Area and Porosity BET instrument. TGA was conducted using a Hitachi STA7300 thermogravimetric analyser. Surface morphologies were imaged with a Zeiss Gemini Ultra 540 Plus FEG-SEM and a Hitachi TM3030 Plus Benchtop SEM.

3.2. **Materials**

Phlogopite, mined in the town of Palabora, in South Africa's Limpopo Province, was supplied by Foskor. The phlogopite was received as 100 – 200 mm lumps which were then crushed, ground and sieved. According to the manufacturer, it is not possible to obtain phlogopite without other mineral impurities. The average composition of the ore mined at Foskor is shown in Table 4.

Table 4: Composition of raw phlogopite ore (from manufacturer)

Mineral	Composition (wt. %)
Diopside	50 – 60
Phlogopite	25 – 30
Apatite	12 – 16
Calcite	< 5

Nitric acid (55 %) obtained from Promark Chemicals was used as the leaching solvent. Sodium hydroxide (98 %) from Sigma-Aldrich was used to produce the base solution for titration, and phenolphthalein from Associated Chemical Enterprises was used as the titration indicator.

3.3. **Planning**

To model the leaching process, the following factors affecting leaching rates were considered: reaction time (t), temperature (T), and acid concentration ($[H^+]_0$). The effects of these independent variables on the gravimetric conversion (α_G) formed the basis for determining the best representative kinetic triplet (model, k_0, Ea). Figure 5 shows the values of each independent variable used and the sequence of experiments conducted for modelling.

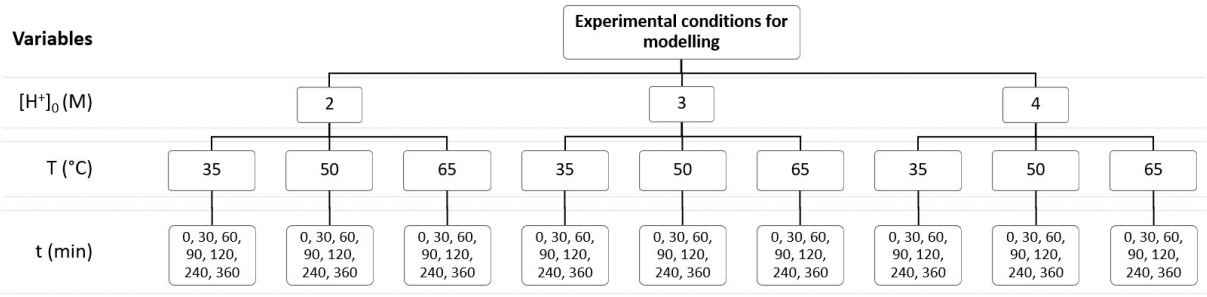

Figure 5: Schematic of experimental plan for modelling.

To ensure that the model accurately represents the leaching process, additional experiments were conducted to test the kinetic information obtained. These experiments were conducted under the conditions shown in Figure 6.

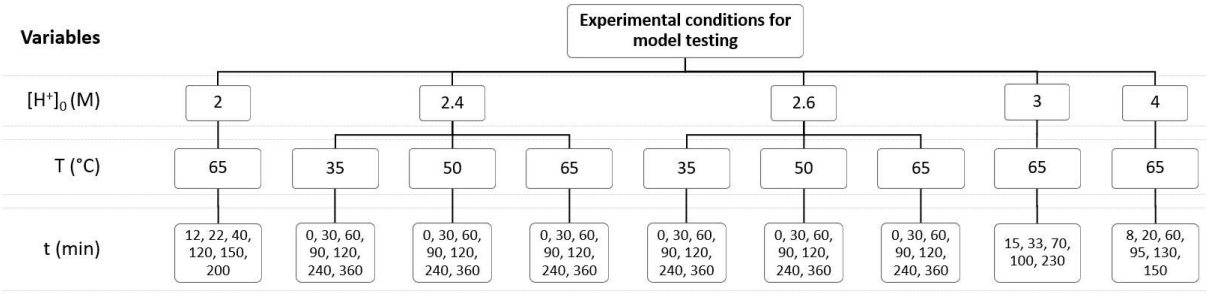

Figure 6: Schematic of experimental plan for model testing.

A reaction temperature of 65 °C was selected for $[H^+]_0$ = 2 M, 3 M and 4 M since it is sufficient for complete conversion to be obtained at a relatively fast rate.

For all experiments, the variables shown in Table 5 were kept constant.

Table 5: Variables kept constant for all experiments.

Variable	Values	Units
Particle size range	250 – 600	µm
Phlogopite mass	20	g
S:L	1:10	g mL^{-1}

To confirm the selection of the kinetic triplet, the composition, structure and physical properties of solids from progressive leaching stages (see Table 6) were characterised.

Table 6: Naming convention of solid residues for analytical characterisation.

Sample name	Degree of leaching (α_G in %)	
	Range	Average
RP	0	0
LP1	10 – 20	14.3
LP2	40 – 50	44.2
LP3	100	100

Results from the complementary analytical techniques employed give an indication of the behaviour of the particles when leached with acid. These techniques include XRF, XRD, FTIR, BET, TGA and SEM-EDS.

3.4. Methods

3.4.1. Leaching

20 g of phlogopite particles of size range 250 – 600 µm were leached with 200 mL nitric acid (Table 5) of various concentrations for different reaction times and temperatures (see Figure 5). These experiments were conducted to obtain kinetic information about the leaching process. Further experiments were conducted to test the kinetic information obtained. These data points will be referred to as "testing data" throughout this report. The experimental conditions for these additional experiments are provided in Figure 6.

For all the experiments, stirring speed was controlled to ensure complete solid suspension within the solvent (no settling) whilst avoiding excessive splashing and vortex formation. Temperature and stirring speed were controlled using hotplate stirrers. All leaching reactions were conducted batchwise, with plastic wrap seals to avoid solution evaporation during experiments. After leaching, the reactor contents were vacuum filtered to separate the solid residue from the leach liquor. The leach liquor was collected and the filter cake was washed three times with distilled water (400 mL in total). After washing, the filter cake was dried at 100 °C overnight. The dried solids were then weighed immediately upon removal from the oven to avoid moisture adsorption and the weights were recorded. These gravimetric values (m_t) were used in equation 3 to calculate the gravimetric conversion, while the leach liquor concentrations were used to calculate elemental conversion (equation 4), volumetric conversion (equation 5), and H^+ concentration. Experiments were repeated for accuracy. Repeat experiments were randomly selected to eliminate any unknown bias.

3.4.2. Solid residue

The solid residues examined were prepared by leaching phlogopite with HNO_3 of different concentrations at 65 °C, for different leaching periods. Batches of the partially leached samples (LP1 and LP2) were obtained by combining acid-leached products from experiments where 10 – 20 %, and 40 – 50 % conversions were respectively obtained. The average conversion values for samples LP1 and LP2 were 14.3 and 44.2 %, respectively. Sample LP3 was obtained by leaching phlogopite with 4 M HNO_3 for 24 hours to ensure complete conversion. A summary of the solid residue naming convention is shown in Table 6.

3.4.2.1. Analytical characterisation

The solid residues described above were analysed by XRF, XRD, FTIR, BET, TGA and SEM.

ICP-OES

A Spectro-Acros ICP-OES analyser was used to determine elemental concentrations within each leach liquor sample. Standard solutions were made using 50 mL, 100 mL, 150 mL, 200 mL and 250 mL of Mg and Ca, with corresponding 20 mL, 40 mL, 60 mL, 80 mL, 100 mL of Fe, Al, K, and Ti, respectively, to calibrate the ICP-OES. Leach liquor samples were diluted with distilled water to a 1:100 volumetric ratio to prevent damage to the equipment, and so that the detected concentrations would be within the calibration range. Standard samples were analysed after every 5 – 10 experimental samples to monitor concentration drift.

XRF

The solid residue samples were roasted in alumina refractory crucibles at 1000° C to determine Loss On Ignition (LOI). 1 g of sample was mixed with 6 g lithium tetraborate flux and fused at 1050 °C to form a stable fused glass bead. The Thermo Fisher ARL Perform'X Sequential XRF instrument with Uniquant software was used for analyses. The software analysed for all elements in the periodic table between Na and U, however, only elements found above the detection limits were reported. Standard sample material was prepared and analysed in the same manner as the experimental samples.

XRD

The solid samples were prepared according to the standardised Panalytical backloading system, which provides a nearly random distribution of the particles.

The samples were analysed using a PANalytical X'Pert Pro powder diffractometer in $\theta - \theta$ configuration with an X'Celerator detector and variable divergence- and fixed receiving slits with Fe filtered Co-Kα radiation (λ=1.789Å). The mineralogy was determined by selecting the best–fitting pattern from the ICSD database to the measured diffraction pattern, using X'Pert Highscore plus software. Data was collected in the angular range of $5° < \theta < 90°$ with a step size of $2\theta = 0.008°$.

ATR-FTIR

Absorbance spectra were recorded on a Perkin Elmer Spectrum 100 using the single reflection ATR diamond crystal. All spectrograms were obtained between 4000 – 550 cm^{-1} at a resolution of 4 cm^{-1} with an average of 32 scans.

BET

The N_2 physisorption analysis was performed using a Micromeretics TriStar II Surface Area and Porosity BET instrument at 77.35 K. Sample measurements were conducted after degassing under vacuum at 110 °C for 24 h to remove surface contaminants while retaining the nature of the solid surface and the sample integrity. N_2 adsorption and desorption isotherms were generated within the relative pressure range of 0.0001 – 0.99.

BET specific surface areas were calculated using the BET method (Brunauer *et al.*, 1938), and pore size distributions (PSD) were determined by the Barrett-Joyner-Halenda (BJH) method (Barrett *et al.*, 1951) for the adsorption isotherms within the pore width range of 2 – 20 nm. According to Rouquerol *et al.*

(2013), the BJH method can be used to provide a useful assessment of mesopore size distributions. The total pore volume was calculated from the maximum amount of nitrogen gas adsorption at $p/p_0 = 0.99$.

TGA

A TGA was conducted using a Hitachi STA7300 thermogravimetric analyser. 10 mg samples were placed in open 70 µL alumina pans. TGA-DTG curves were generated for temperatures up to 1000 °C at a heating rate of 10 °C min^{-1} and a nitrogen flow rate of 100 mL min^{-1}.

FEG-SEM

The surface morphologies of the raw and completely leached phlogopite samples were imaged with a Zeiss Gemini Ultra 540 Plus Field Emission Gun Scanning Electron Microscope (FEG-SEM) with BS, EDS and EBSD detectors. Prior to scanning, samples were mounted on an aluminium stub using carbon tape. High-pressure argon was used to remove loosely bounded surface atoms for cleaner surfaces. The samples were then carbon coated for conductivity using a Quorum Q150T ES sample preparation system. The SEM images were generated using 1 kV and 3 kV acceleration voltages.

To properly understand the attack proton mechanism, delaminated phlogopite sheets were leached with 4 M HNO_3 for 1 hour at 70 °C. The leached products were analysed by SEM and EDS using a Hitachi TM3030 Plus Benchtop SEM. This experiment will be referred to as “LP4”.

3.4.2.2. Modelling

Because goodness of fit is closely related to model selection (Joseph, 2019), goodness of fit criteria was used to evaluate how well the experimental data fit the regression function based on R^2 values of models with the same amounts of included parameters and data points. This method was first used to compare R^2 values of the integral forms ($g(\alpha)$) of the reaction models in Table 2 versus time using Microsoft Excel®. It was also used to determine whether certain models obeyed the Arrhenius equation. Relationships were established between kinetic parameters (k_0 and Ea) and initial acid concentration based on goodness of fit of the regression model to the experimental data in the Arrhenius plot. Predictions from the selected model were compared to experimental data and the R^2 value was used to determine the proportion of data points that fit the best-fitting regression line.

3.4.3. Leach liquor

The leach liquor was analysed by ICP-OES and by titration using sodium hydroxide as the base solution and phenolphthalein as the indicator. The data obtained was mainly used to verify observations from analysing the solids in terms of elemental conversion, volumetric conversion and H^+ concentration.

4. Results and Discussion

This chapter includes the results obtained from the experimental work, presented in tabular and graphical forms with some additional data (raw data, intermediate trivial results, and computer codes) provided in the appendices. Technical results have been justified based on correlations between variables. The significance of all results has been discussed and supported with additional results and/ or literature. This chapter has been sub-divided into a characterisation section, and a leaching section and all products (acid-leached solid residue and leach liquor) were analysed to provide important information about the leaching process and to confirm complimentary results. Results obtained from the characterisation of the raw phlogopite and acid-leached solid residues are reported first so that the particles can be better understood on a molecular level before the process is modelled.

4.1. **Characterisation of the raw phlogopite and acid-leached solid residue**

4.1.1. Chemical composition analysis (XRF)

Table 7 shows the chemical compositions of the raw and leached phlogopite samples obtained by XRF analysis. The results for the raw phlogopite sample generally correspond with the literature values in Table 1. This is indicated by the standard deviation in the final column of Table 7. The raw phlogopite used in this study contains more Fe_2O_3, CaO, and P_2O_5, with less Al_2O_3 than the typical phlogopite sample (Table 1). This is indicated by the larger standard deviations for these constituents.

Table 7: Chemical compositions (wt. %) of the raw and leached phlogopite samples obtained by XRF, with standard deviations of RP from literature values shown.

Sample	RP	LP1	LP2	LP3	Standard deviation of RP from literature
SiO_2	40.5	46.4	51.8	95.3	0.05
MgO	25.0	26.1	23.4	1.67	0.15
Al_2O_3	9.62	9.81	7.94	0.10	3.83
K_2O	9.21	8.10	6.04	0.15	0.41
Fe_2O_3	7.13	7.17	6.13	0.56	2.70
CaO	2.68	0.02	0.07	0.01	1.45
P_2O_5	4.51	1.15	3.52	1.71	2.93
TiO_2	0.87	0.86	0.80	0.37	0.04
TOTAL	99.5	99.7	99.7	99.8	-
LOI	2.18	5.58	6.18	8.19	-

The results in Table 7 were normalised to exclude LOI contents for a more direct comparison between samples and so that the results would be more representative of the gravimetric data recorded for the modelling experiments (Figure 5). The gravimetric data corresponds with the solid masses that were dried at 100 °C, whereby most of the moisture contents is removed (see Section 4.1.5. Thermal Analysis (TGA-DTG)). The LOI contents are shown below the total wt. % values and represent the total volatile contents.

The amounts of Mg, Al, K, Fe, Ca, and Ti present in the leached samples decreases, as expected, with leaching. Consequently, the SiO_2 concentration increases dramatically as a result of the cationic extractions. Sample LP3 is almost completely SiO_2, with <5 % of the other components present. Figure

7 compares the conversion rates of the various elements present in the phlogopite and was developed based on equation 13,

$$\alpha_i = \frac{|m_{i,0} - m_{i,t(s)}|}{m_{i,0}} \quad (13)$$

where $m_{i,0}$ is the mass of element i (= K, Mg, Fe or Al) present in the raw phlogopite sample, and $m_{i,t(s)}$ is the mass of element i present in the acid-leached solid residues.

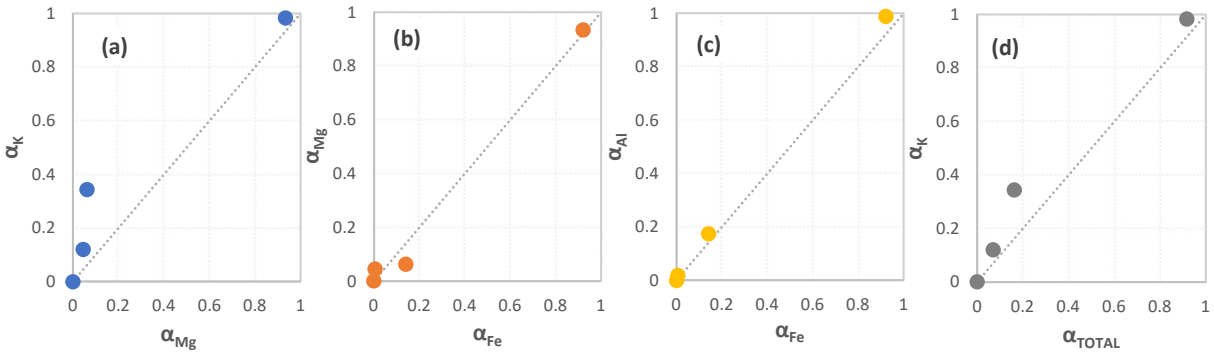

Figure 7: Comparison between elemental conversion rates based on XRF analysis.

It is shown in Figure 7(a), that K is released at a faster rate than Mg. For example, when α_{Mg} = 0.06 (6 % conversion of Mg is achieved), then at this point, the conversion of potassium (α_K) is 0.34 (34 %), so the conversion of potassium is clearly faster. The 1:1 lines indicate points of equal conversion. Therefore, the release rates of Mg and Fe (Figure 7 (b)) and Al and Fe (Figure 7 (c)) are similar since most of the points lie close to the identity lines. Because the release rates of both Mg and Al are similar to Fe, then, by association, the release rate of Mg must be similar to that of Al. It can thus be concluded that K is released faster than all these elements. This is confirmed in Figure 7 (d), where α_{TOTAL} is the conversion of the sum of the individual elements. This behaviour is expected since the K^+ ions occupy the interlayer sites of the phlogopite and are, therefore, more susceptible to proton attack than the other cations. Similar trends were observed by Kuwahara and Aoki (1995) and Wypych *et al*. (2005). The acid then progresses along the tetrahedral and octahedral sheets, resulting in the release of the remaining cations from the phlogopite structure. The stronger bonds occurring in the T-O-T layers are responsible for the slower conversion rates of these cations (Fe^{3+}, Mg^{2+}, and Al^{3+}). After prolonged leaching, cations are released at similar rates (i.e., the data points lie close to the identity lines) and since most of the potassium is extracted at this point, the potassium extraction rate may be slower than the extraction rates of the other cations.

4.1.2. Crystalline structure analysis (XRD)

Leaching affects the structures of crystalline materials, and the interplanar spacing (d) could, therefore, be affected due to structural collapse or expansion. XRD is effective for characterising crystalline structure variations. The XRD patterns, or diffractograms, for the raw phlogopite and the leached samples, are shown in Figure 8 with an enhanced view of the 20° ≤ 2θ ≤ 40° region for clarity of less intense peaks.

The XRD patterns show that phlogopite is present in all the samples with its primary peak around 10.14°, and secondary peaks around 20.35°, 30.73°, 41.37°, and 52.40° for the raw phlogopite. The counts of sample RP are very high with strong, sharp diffraction peaks indicating preferred orientation and high crystallinity of the raw phlogopite structure. Quartz (SiO_2), diopside, and apatite were also

detected in the raw phlogopite sample with primary peaks around 30°, 35° and 37°, respectively. Calcite could be present in the raw phlogopite sample with a primary peak also around 35°. These impurities are present in the phlogopite ore as mined from Foskor (Table 4).

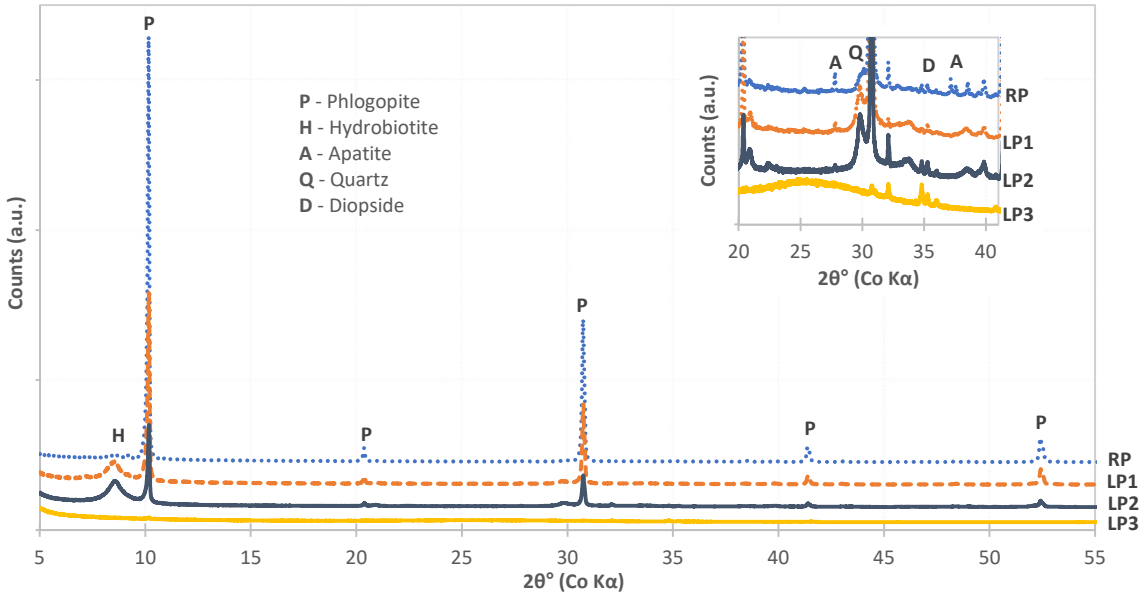

Figure 8: X-ray diffractograms for each sample with a magnified view of the 2θ = 20° - 40° region and characteristic peaks shown.

The diffractograms of the partially leached samples are similar to that of the raw phlogopite sample, however, the peaks are considerably less intense due to structural degradation of the raw phlogopite by the dissolution of the octahedral cations, and the peaks shift slightly to higher angles with the primary peaks of LP1 and LP2 at 10.16°. The reduction in peak intensity implies that there is a time-dependent loss in crystallinity of phlogopite upon acid leaching.

The locations of the highest XRD peaks are related to the interplanar distance (d) (Bigham *et al*., 2001; Niu *et al*., 2020). Since the d-spacing is based on Bragg's Law (Cullity, 1956), a peak shift to higher angles implies that there is a reduction in the interplanar spacing. Therefore, the interplanar spacing of phlogopite decreases by < 0.2 % with an increase in conversion, from 10.12 Å for the raw phlogopite to 10.11 Å for the partially leached samples. The slight reduction in the interplanar space could be due to an increase in lattice defects (vacancies) or electrostatic interaction between interlayers from the removal of cations from the lattice (Niu *et al*., 2020). Hydrobiotite, an alteration product of other micas, was also detected in the raw and partially leached samples. Hydrobiotite peaks are located around 8.5°, 10°, 20°, and 30°. Most of the impurity peaks are small in comparison to the phlogopite peaks, and are, therefore, enhanced for a better view between the 20°- 40° region on the 2θ axis.

The XRD pattern for LP3 shows a drastic decrease in the phlogopite peak intensities, with the formation of a halo at 2θ between 22° – 29° corresponding to an amorphous product. The most dominant peak for quartz occurs at 2θ = 30.8°. Peaks observed 35° and 41.5° indicate the presence of diopside in the material. The d-spacing decreased from 10.12 Å for the raw phlogopite sample to 9.83 Å for the completely leached sample. This means that the interplanar space of the (001) lattice plane decreased by 2.9 % (or 0.29 Å) under complete conversion. This could be attributed to lattice defects caused by the loss of ions which have considerable volume and charge causing electrostatic interactions between layers within the lattice and the interlayer (Niu *et al*., 2020).

Since the raw phlogopite is highly crystalline, the absence of defects in the lattice means that the motion of H^+ ions permeating into the lattice is restricted (Ropp, 2003; Schmalzried, 1995). This strongly suggests that the leaching is internal diffusion-controlled since the mobility of constituents into the system is the controlling factor. Therefore, the use of the D1 model for one-dimensional diffusion through a flat plate (Khawam & Flanagan, 2005) is the recommended model to represent the leaching process. This also confirms results found by Kaviratna and Pinnavaia (1994) who reported that the depletion of cations from the octahedral sheets and interlayers occur by proton attack at layer edge sites since cations cannot be effected through the highly ordered, unbroken silicon-oxygen layers which surround the basic components. Okada *et al*. (2006) reported that rapid leaching is associated with high S_{BET} and low crystallinity and that slow leaching is due to reduced Mg (Fe) content in the octahedral sheets and less Al substitution in the SiO_4 tetrahedral sheets. Therefore, despite the high crystallinity and low surface area of the raw phlogopite, it still undergoes rapid leaching due to its abundance of Mg and Fe in the octahedral sheets and Al in the tetrahedral sheets (refer to Table 7 for Mg, Al and Fe content). The presence of microfractures on the surface of the particles would provide additional access pathways for proton attack, thereby increasing leaching rates. A SEM analysis could be used to determine whether such fractures are present.

4.1.3. Chemical nature analysis (ATR-FTIR)

The chemical natures of the samples were confirmed by studying the FTIR fingerprints of each sample. The FTIR spectra for all the samples are shown in Figure 9 with a scaled view of the high energy bands in the 1350 – 550 cm^{-1} region of interest. Characteristic vibration bands of phlogopite are provided in Table 3 with their corresponding wavenumber positions.

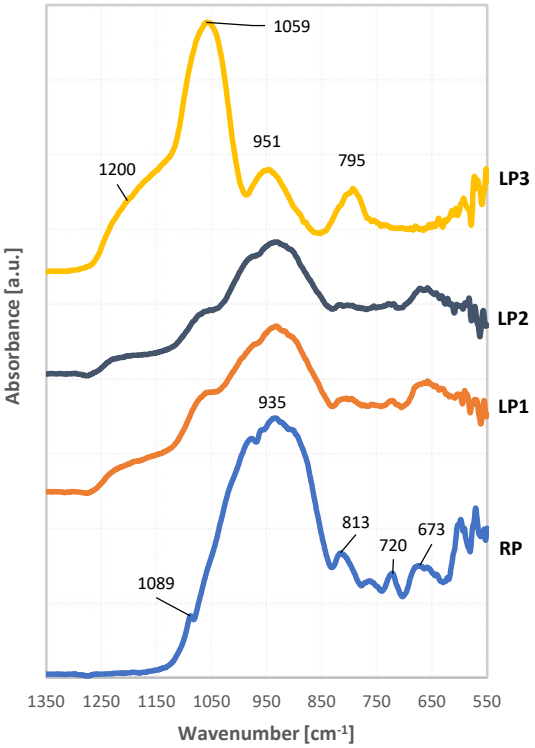

Figure 9: FTIR spectra of raw phlogopite and leached products.

The raw phlogopite sample exhibits characteristic vibration bands around 935, 813, 720, 673, and 571 cm^{-1} which corresponds with literature values (Beran, 2002; Jenkins, 1989). According to the Beer-

Lambert law (Stuart, 2004), the peak intensity in infrared spectra is proportionally related to the concentration of molecules in a sample. Therefore, the reduced intensities of absorbance bands around 935, 813, and 720 cm^{-1} as leaching increases, is due to the structural degradation of the phlogopite associated with the removal of the Mg^{2+}, Fe^{3+} and Al^{3+} cations (Farmer, 1974; Temuujin *et al*., 2004).

The raw phlogopite sample and the partially leached samples exhibit strong, well-defined vibration bands around 935 cm^{-1}. This band can be attributed to Si – OH vibrations (Mendelovici *et al*., 2001) and is formed by the hydroxylation of acid-leached apical oxygen atoms originally bound to the brucite-like sheet (Wypych *et al*., 2005). These silanol groups are expected to be hydrogen-bonded to water molecules on account of hydration (Wypych *et al*., 2005). The medium vibration bands observed at 720 and 813 cm^{-1} are ascribed to Al in the tetrahedral sheets of the phlogopite structure. This initiates Al/Si disorder as a result of Al – O – Si and Al – O – Al linkages, respectively (Beran, 2002). The reduced absorbance intensities of these bands in LP1 and LP2 and the absence of this band in sample LP3 verifies the removal of Al by leaching.

The absorbance spectra observed for the completely leached sample (LP3) displaying bands at 1059, 951, and 795 cm^{-1}, resembles that of amorphous silica gel (Costa *et al*., 1997; Ocaña *et al*., 1989). After complete leaching (LP3), an amorphous silica product is obtained as indicated by the dominant vibration band at 1059 cm^{-1} with a shoulder around 1200 cm^{-1}. These bands are associated with stretching and bending vibrations of SiO_4 tetrahedra (Awazu, 1999; Farmer, 1974). The presence of the band at 795 cm^{-1} further confirms the formation of a three-dimensional amorphous silica phase (Costa *et al*., 1997; Deysel *et al*., 2020; Madejová and Komadel, 2001; Okada *et al*., 2002; Temuujin *et al*., 2003) which confirms results obtained from the Crystalline structure analysis (XRD).

Si – O bending vibrations in the high energy regions of the mid-IR spectrum are often coupled with stretching and bending vibrations of the cation-oxygen octahedra occurring in corresponding spectral regions. Vibration bands of octahedral Mg are expected in the far IR spectral range. However, the 673 cm^{-1} band may be attributed to the combined effects of Si – O stretching vibration and Mg – O vibration (Si – O – Mg) (Beran, 2002). The reducing intensities of this band in the leached samples are likely due to the decreased abundance of Mg in the octahedral sheets. Kloprogge and Frost (1999) and Madejová and Komadel (2001) assigned bands around 620, and 660 cm^{-1} to OH – Mg – OH deformations.

Further details on the interpretation of vibration bands for the FTIR spectra of phlogopite and its amorphous silica product can be found in literature (Awazu, 1999; Beran, 2002; Farmer, 1974; Jenkins, 1989; Kloprogge and Frost, 1999; Madejová and Komadel, 2001; Scordari *et al*., 2006; Šontevska *et al*., 2008; Vedder, 1964; Wen *et al*., 1988).

4.1.4. Surface area and porosity analysis (BET)

N_2 adsorption-desorption isotherms

The nitrogen adsorption-desorption isotherms (Figure 10) obtained from the BET analysis are used to determine and compare the pore structure and surface area characteristics between the samples.

As shown in Figure 10 (a), the adsorption and desorption curves for sample LP3 overlap at low relative pressures, with narrow separations from relative pressures of around 0.4, creating hysteresis loops (Sing, 1985). Based on the IUPAC classification (Figure 4), these loops can be related to pore structure and shape (Rouquerol *et al*., 2013). The overlap of curves at low to medium relative pressures

indicates large adsorption volumes, and the narrow separations between the curves at medium to high relative pressures indicate capillary condensation. Adsorption hysteresis is generally associated with mesoporous adsorbents (Thommes *et al*., 2015).

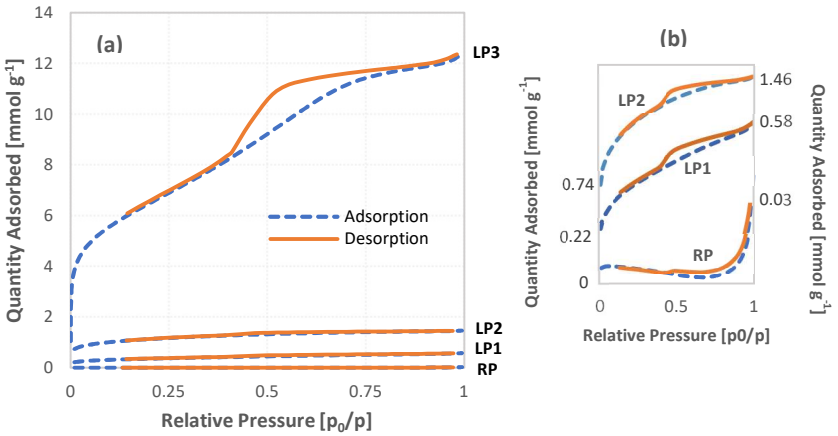

Figure 10: BET N_2 adsorption and desorption isotherms for all samples (a) with a scaled view for clarity of selected hysteresis loops (b).

Particles with larger surface areas are physically capable of adsorbing larger quantities of adsorbate onto their surfaces. Due to the significant amount of N_2 adsorbed in sample LP3, Figure 10 (a) illustrates how the surface area of LP3 is orders of magnitude greater than that of the partially leached and raw phlogopite samples, with the adsorption-desorption isotherms of sample RP barely visible in comparison. This makes it difficult to observe the hysteresis loops of the other samples. Therefore, a scaled view of the adsorption-desorption isotherms for samples RP, LP1, and LP2 is provided in Figure 10 (b).

All adsorption isotherms most closely resemble Type IV, with H3 and H4 hysteresis loops for RP and the leached samples (LP1 – LP3), respectively (see Figure 4). This means that all the samples have mixtures of mesopores and micropores and interactions between gas molecules and adsorbent mesopore surfaces lead to capillary condensation. The shape of H3 hysteresis loops (for sample RP) is similar to Type II isotherms, with deviations characteristic of solids containing aggregated non-rigid plate-like particles, such as certain clays (Yuan & Rezaee, 2019; Labani *et al*., 2013) with parallel plate-shaped pores. Hysteresis loops of Type H3 may also represent macropores partially filled with pore condensate (Thommes *et al*., 2015).

The adsorption-desorption isotherms of samples LP1 and LP2 are similar to that of LP3, whereby the N_2 adsorbed increases for all relative pressure values. There is a steep increase in N_2 adsorbed at low pressures for all leached samples (LP1 – LP3). As the relative pressure increases, the N_2 adsorbate continues to cover the external surface and pore walls of larger pores, forming the monolayer. According to Sing (1982), the monolayer of many samples is typically filled when a relative pressure of 0.1 is reached. After which, multilayer adsorption occurs on the external surface of the sample and within the larger pores. This corresponds to the gradual adsorption of N_2 with an increase in pressure. As the pressure approaches saturation pressure, the adsorbate continues filling the larger pores, until all smaller pores are completely filled with adsorbate. Larger macropores may remain only partially filled. The near-vertical adsorption isotherm at very low relative pressures ($p/p_0 < 0.05$) for LP3 is indicative of the presence of micropores in the completely leached phlogopite sample. This was not observed for the other samples. Smaller pore sizes correspond to the larger surface area of the leached phlogopite product (SiO_2). All the leached phlogopite samples (LP1 – LP3) represent Type H4 hysteresis, with higher uptake of adsorbents at low relative pressures. The H4 type hysteresis loop is characteristic of mesoporous, and possibly microporous substances, which experience capillary

condensation and contain narrow slit-like pores (Thommes *et al*., 2015). Slit-shaped micropores may form between adjacent tetrahedral silica sheets of selectively leached clays (Härkönen & Keiski, 1984; Kosuge *et al*., 1995; Okada *et al*., 1998; Temuujin *et al*., 2003). According to Milliken *et al*. (2013), brittle minerals and clay minerals generally form micropores and mesopores. This was further confirmed by Okada *et al*. (2002) who leached phlogopite with nitric acid. Härkönen and Keiski (1984) reported that micropores formed when interlayer K^+ cations fully dissolved, mesopores formed when cations from the octahedral sheets began to dissolve, and finer pores formed when Si tails near the plate edges became disordered and entangled.

In summation, it can be concluded that all samples contain mainly open pores, as exhibited by the hysteresis between the adsorption and desorption curves. The raw phlogopite contains parallel-plate and slit-shaped pores and the leached samples contain mainly slit-like pores. According to Xue *et al*. (2016), tapered plate pores and parallel-plate pores are associated with interlayer intraparticle pores or microfractures between the layers of clay minerals.

Pore Size Distributions (PSD)

The pore size distributions (Figure 11) were calculated from the N_2 adsorption isotherms (Figure 10).

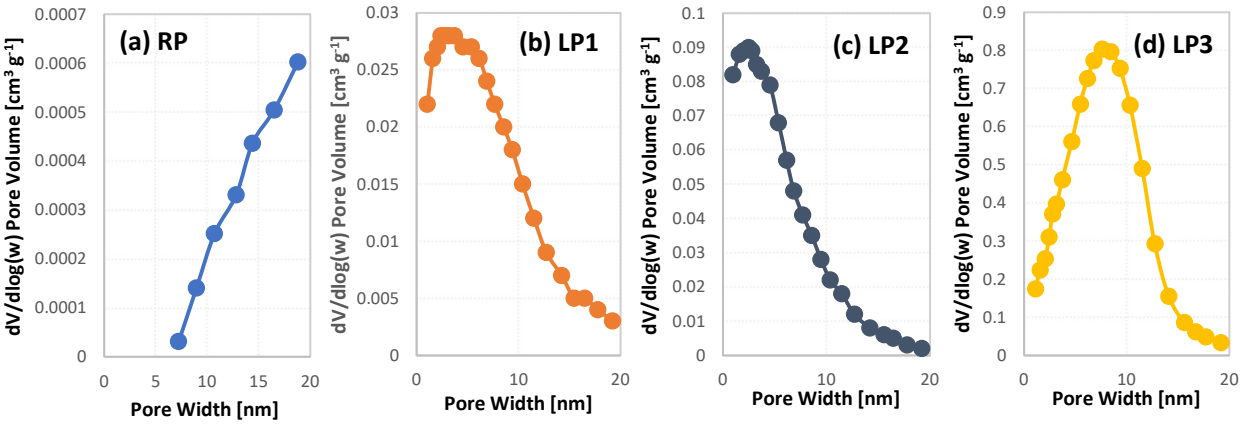

Figure 11: Pore size distributions in terms of adsorption pore volume and area for all samples.

As shown in Figure 11 (a), the pore widths range from 7 – 20 nm for the raw phlogopite sample, indicating mesoporosity (Rouquerol *et al*., 1994). There is a larger volume of pores (6.2 x 10^{-4} cm^3 g^{-1}) with widths around 20 nm. The absence of a distinct peak in the raw phlogopite sample substantiates its near "nonporous" state. Conversely, the leached samples (Figure 11 (b)-(d)) show higher peak values (0.028, 0.085, and 0.8 cm^3 g^{-1}) at pore widths around 2 nm and 4 nm for the partially leached samples, and completely leached sample, respectively. The drastic increase in peak pore volume values and the slight peak shifts are indicative of the increase in porosity, and hence surface area, of the samples with an increase in conversion. It can also be observed that the leached samples contain some micropores. According to Okada *et al*. (2005), micropores are expected to form from selectively leaching octahedral sheets of 2:1 type clay minerals. Micropore volumes were found to be 1.9 x 10^{-3}, 9.4 x 10^{-3}, 27.6 x 10^{-3} cm^3 g^{-1} for LP1, LP2 and LP3, respectively.

Summary

A summary of the pore sizes and specific surface areas from the BET analysis are shown in Figure 12. The average pore widths shown in Figure 12 (a) indicate that the samples are mostly mesoporous. Pore sizes dramatically decrease from raw, unleached phlogopite to completely leached phlogopite

(by ≈29 %). This decrease in the pore size corresponds with the higher specific surface areas of the leached phlogopite products, from a mere 0.22 $m^2 g^{-1}$ for the raw phlogopite to 28, 89 and 517 $m^2 g^{-1}$ for LP1, LP2 and LP3, respectively (Figure 12 (b)). The surface area increases by more than 2000 times the original value throughout the leaching process. Okada *et al*. (2005) suggest inhibiting the development of framework structure units and maximising the amount of layered structure units to increase the surface areas of the products formed. As shown in Figure 12 (b), the surface area of the raw phlogopite sample is very low. Some sources consider phlogopite to be nonporous (Härkönen & Keiski, 1984). Figure 12 (b) also indicates that the external surface areas or non-micropore areas of the leached products (LP1 – LP3) account for the majority of the BET surface area. This means that there are more larger pores than micropores. Micropores contribute 63 %, 44 %, 40 %, and 34 % of the total BET surface area of samples RP, LP1, LP2, and LP3 respectively. As leaching time increases, more pores are formed (mesopores and micropores). Some micropores may be unstable and become mesopores as leaching time increases.

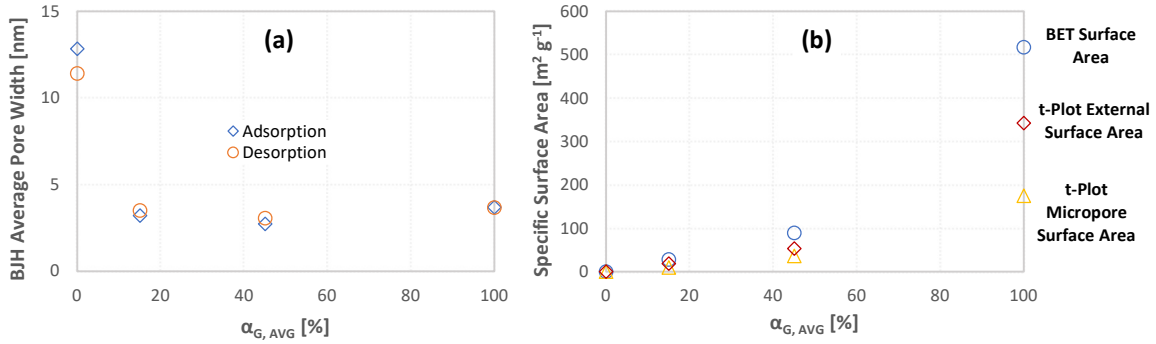

Figure 12: (a) Pore size and (b) surface area summary from BET analysis.

To summarise, as the phlogopite solids are leached, cations of K, Mg, Fe, and Al are removed from the layered structure leaving vacancies, or "pores" in the structure. These pores provide an increased surface area on the material for subsequent reactions. The final product is highly porous, which is favourable in various applications (Bardestani *et al*., 2019; Kaviratna & Pinnavaia, 1994; Wypych *et al*., 2005). This explains the shapes of the adsorption-desorption isotherms (Figure 10). The quantity of N_2 adsorbed increases with leaching extent. A more porous surface means that there is a greater area onto which N_2 atoms may be adsorbed. The maximum values of N_2 adsorbed are 0.026, 0.569, 1.46, 12.4 mmol g^{-1} at high pressures for the raw phlogopite (RP), partially leached phlogopite (LP1 and LP2), and the completely leached phlogopite (LP3) samples, respectively. It is also clear from the pore size distributions (Figure 11), that the leached particles contain both micropores, as well as mesopores of slit-shape. A very small area of pores occupies the raw phlogopite sample (0.217 $m^2 g^{-1}$) rendering it near nonporous. Figure 12 (b) displays the drastic increase in specific surface area from 0.217 $m^2 g^{-1}$ (RP) to 517 $m^2 g^{-1}$ (LP3). The SSA of completely leached phlogopite sample (LP3) is in accordance with previously recorded leached phlogopite values (Härkönen & Keiski, 1984; Okada *et al*., 2005, Okada *et al*., 2002; Venter, 2015).

4.1.5. Thermal Analysis (TGA-DTG)

A TGA was conducted on the raw material and the leached products to investigate the possible components present in each sample and to further confirm results obtained from prior analyses. Continuous TG mass loss curves were observed for each sample over the entire temperature range, as shown in Figure 13 (a). To easily compare the mass losses incurred in each sample, all TG curves were plotted on the same set of axes, with the mass losses at selected temperatures (dotted lines in Figure 13 (a) and Figure 13 (b)) shown in Figure 13 (c).

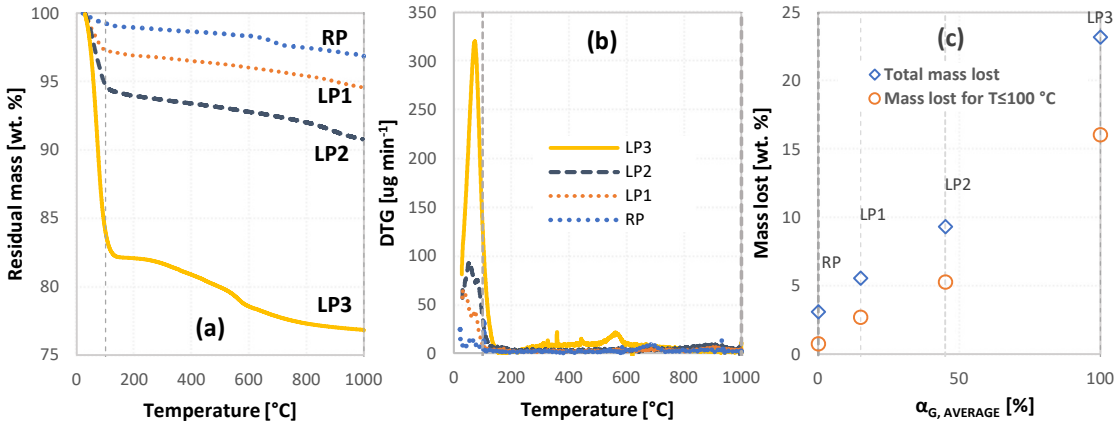

Figure 13: Comparison of TGA (a) and DTG (b) curves of all samples over the entire temperature range, and (c) masses lost selected temperatures (100 °C and 1000 °C).

Mass is lost from the RP sample in two main regions. Mass losses at temperatures below 200 °C correspond with desorption of physisorbed water molecules, and mass losses at temperatures above 600 °C are due to dehydroxylation reactions. The leached samples also experience dehydration for temperatures below 200 °C, with gradual weight losses above 300 °C which may represent condensation of the silanol Si – OH groups and subsequent release of strongly held interlayer water. The DTG curves emphasise the zones at which the reaction steps occur over the entire temperature range. The derivative curve peaks (Figure 13 (b)) denote the points at which the mass loss rate is maximised on the weight loss curve.

The TGA results confirm the observations made by the BET analysis. Since LP3 has a larger surface area than the other samples, a larger quantity of water may become physically adsorbed to its surface, hence, 17.5 % of the mass is lost compared to 0.9 – 6 % for the other samples within the first 10 minutes of heating (< 120 °C) (Figure 13 (c)). Furthermore, LP3 mass losses are more significant than RP and the partially leached samples since LP3 lacks the K, Mg, Fe, Al, Ti and Ca (Table 7) contents which are present in increasing quantities in LP2, LP1, and RP, respectively. These cations are retained in the structures of the samples and are not released within this temperature range, resulting in less significant weight losses in the raw and partially leached samples.

4.1.6. Morphology and composition distribution analysis (SEM-EDS)

Figure 14 shows the surface morphologies of the raw and completely leached phlogopite samples obtained by the FEG-SEM analysis.

The SEM micrographs indicate that the layered structure and platy morphology of the raw phlogopite is retained despite prolonged leaching. The raw phlogopite sample (Figure 14 (a) and (b)) exhibits faint cracks on its surface, while the cracks appear more pronounced for the completely leached sample (Figure 14 (c) and (d)). The completely leached sample appears to have deteriorated edges, supporting the notion of proton access by the edge attack mechanism (Kaviratna & Pinnavaia, 1994). However, the cracks could also provide entry for proton attack. The leaching behaviour at the edges and cracks were examined by SEM-EDS analyses (Figure 15 - Figure 16) for experiment LP4.

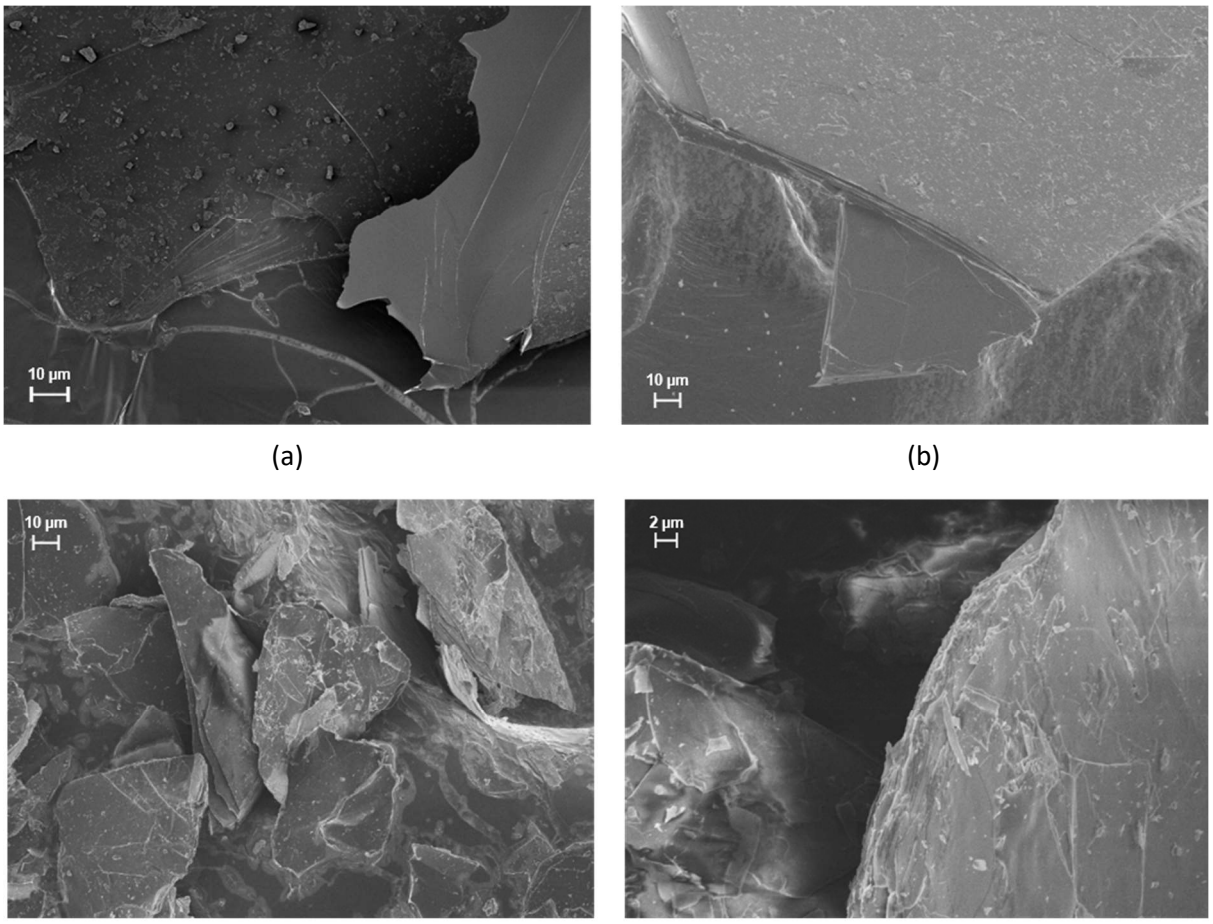

(a) (b)

(c) (d)

Figure 14: SEM images of the raw phlogopite (a) and (b), and the completely leached phlogopite (c) and (d).

The cracks observed in Figure 14 are more distinctively shown in Figure 15. The darker regions shown in Figure 15 indicate the most leached areas of the phlogopite sample. The intensity of the darker areas is proportional to the degree of leaching obtained at the corresponding sites. Therefore, it is clear that there is not always a smooth advancing front from the edges, but that the acid does, in fact, attack through the cracks as well.

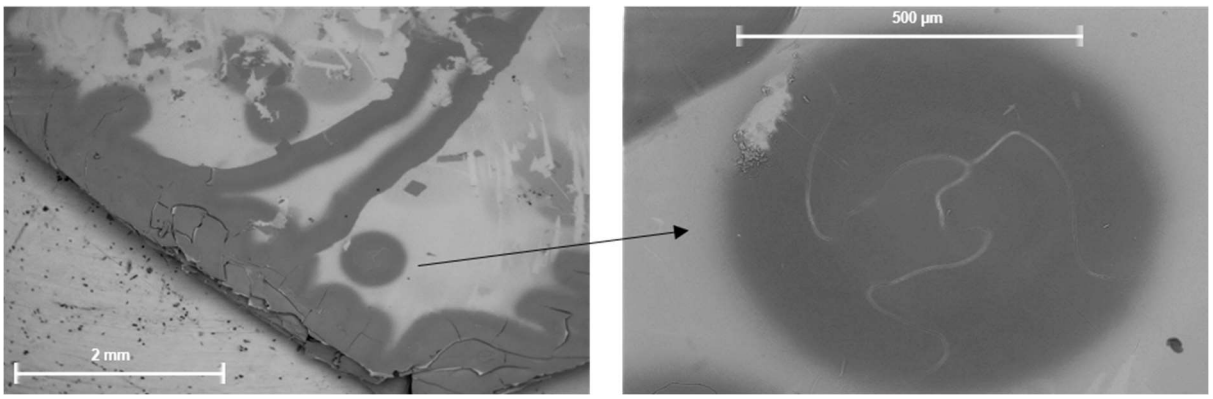

(a) (b)

Figure 15: SEM Images for LP4 emphasising edge deterioration and surface cracks (a), with an enhanced view of a surface crack shown (b).

The EDS analysis of sample LP4 is provided for the sample edges (Figure 16 (a)) and for the sample cracks (Figure 16 (b)). Letters A – E are provided to indicate points on the SEM images with their corresponding positions on the concentration profiles below.

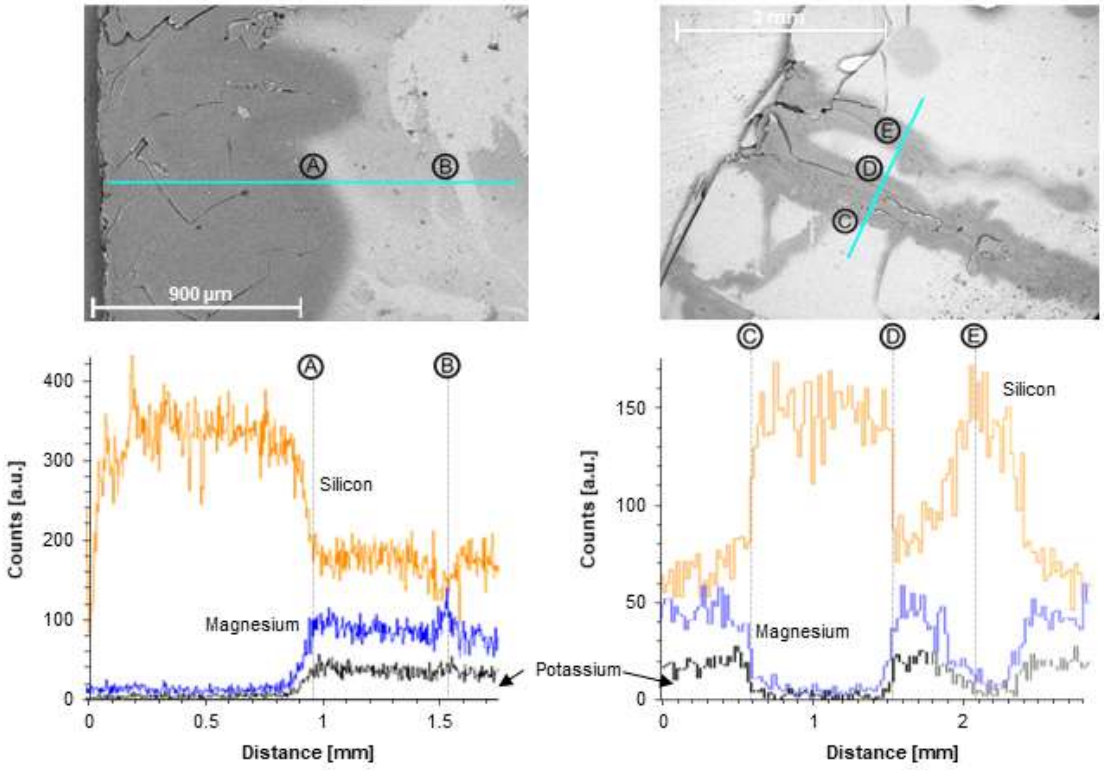

(a) (b)

Figure 16: EDS analysis focused on the edges (a) and cracks (b) of sample LP4 indicating the concentration profiles of potassium, silicon and magnesium along the spans shown.

Sharp decreases in both the potassium and magnesium concentrations can be observed at the leaching front, whether just from the edge (Figure 16 (a)) or due to cracks (Figure 16 (b)), which is an indication that the cations are leached from the phlogopite at similar rates at this temperature. Conversely, there was a corresponding increase in the Si concentration at the leaching front. This is because the Si does not dissolve in the HNO_3 solution as the other cations do.

4.2. **Leaching**

The leaching reaction is expected to proceed according to the balanced chemical equation 14, which follows the general scheme of equation 1.

$$[(Ti_{0.05}Fe_{0.38}Mg_{2.64})(Si_{2.87}Al_{0.8})O_{10}(OH)_2](K_{0.83}Ca_{0.34}) + 10.53HNO_3 \rightarrow 0.05Ti(NO_3)_4 + 0.38Fe(NO_3)_3 + 2.64Mg(NO_3)_2 + 2.87SiO_2 + 0.8Al(NO_3)_3 + 0.83KNO_3 + 0.34Ca(NO_3)_2 + 6.27H_2O \quad (14)$$

The structural formula (half-cell) of the raw phlogopite was calculated using the method prescribed by Foster (1960) for approximating the structural formula of trioctahedral micas and is based on the chemical composition of the raw phlogopite sample as shown in Table 7. The XRF data was also used to calculate the average molar mass of the raw phlogopite sample (430 g mol^{-1}). According to equation 14, and based on the XRF data in Table 7, 2.45 M HNO_3 (200 mL) is theoretically required to completely react the raw phlogopite (20 g).

4.2.1. Leached Solids

This section describes how, aside from the characterisation section (Section 4.1. Characterisation of the raw phlogopite and acid-leached solid residue), the acid-leached solid products (leaching residues) were also used to analyse the effects of temperature and acid concentration on α_G, to develop and test the kinetic model, and to develop kinetic triplet relationships which could be used to model the leaching process for different initial acid concentrations.

4.2.1.1. Overall Gravimetric Conversion

The masses of leached solids obtained from the leaching process can be used to determine the overall gravimetric conversion (α_G). The solids remaining after complete conversion are primarily SiO_2 as indicated by XRF, XRD, FTIR and SEM-EDS (Section 4.1). Deysel *et al*. (2020), Härkönen and Keiski (1984), Okada *et al*. (2002), Venter (2015), and Wypych *et al*. (2005) obtained similar results after complete leaching of phlogopite. The α_G data are presented in Figure 17 (concentration profiles) and Figure 18 (temperature profiles), with the raw data shown in Appendix A.

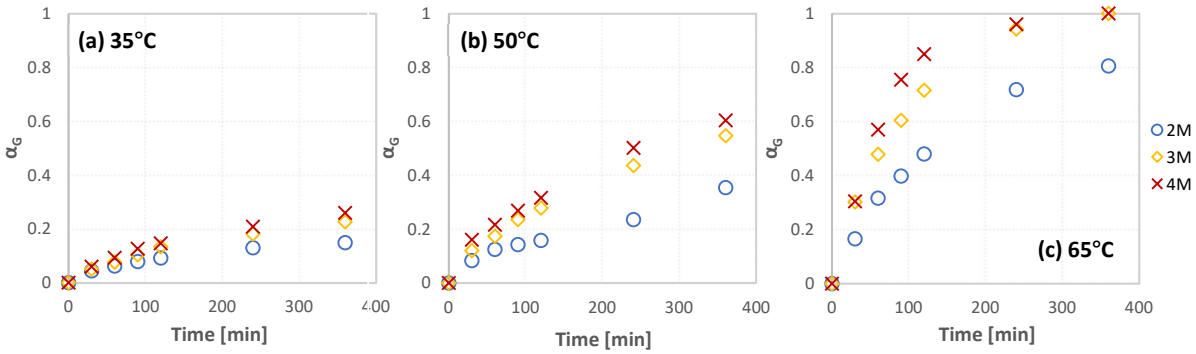

Figure 17: Concentration profiles of α_G vs time for different reaction temperatures.

It is clearly shown, in Figure 17, that conversion increases with an increase in acid concentration for each temperature. An increase in acid concentration means that more H^+ ions are available to react, thereby increasing the number of interactions between the reacting species, which increases the reaction rate (Kotz *et al*., 2012: 692).

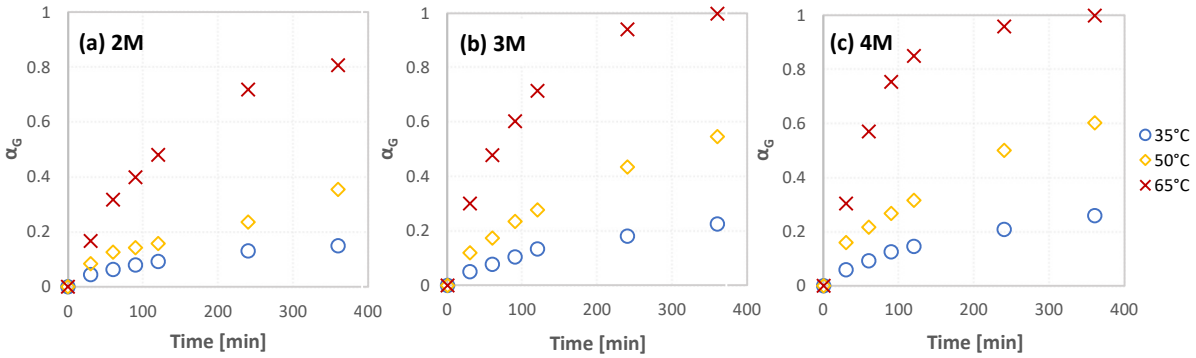

Figure 18: Temperature profiles of α_G vs time for different acid concentrations.

It can also be observed, from Figure 18, that conversion increases with an increase in temperature. This is because higher temperatures increase the kinetic energies (and hence, the movement) of the reacting species, thereby reducing the viscosity and density of the solvent (Liong et al., 1991; Perry and Green, 1999), and increasing the diffusion (Boundless, 2020; Liong *et al*. 1991). Additionally, once

these “energised” molecules have diffused into the solid particles, the reaction rate is also increased as the fraction of molecules with sufficient energy to effectively collide and overcome the activation energy of the reaction increases (Kotz *et al*., 2012: 696). The temperature effect on both the chemical and physical (diffusional) rate constants can be represented by Arrhenius-type equations (Dybkov, 2002, p. 28; Levenspiel, 1999, p. 390; Poling et al., 2001, p. 11.39; Ropp, 2003, p. 151), where it can be seen that temperature has a significant influence on the reaction and diffusion rates. However, the activation energy of the chemical reaction is generally higher than that of diffusion and the reaction rate is more temperature-sensitive than the diffusion rate (Dybkov, 2002, p. 29; Levenspiel, 1999, p. 390).

The effect of temperature on conversion is greater than the effect of concentration as indicated by the slopes of the curves in Figure 17 and Figure 18. The slope steepens between 2.95 – 10.8 % conversion min^{-1} as concentration increases from 2 M – 4 M and between 23.8 – 29.6 % conversion min^{-1} as temperature increases from 35 °C – 65 °C. Therefore, the average slope or conversion rate over time is 3.88 times more sensitive to temperature changes than concentration changes (within the given ranges).

4.2.1.2. Modelling

Model selection

The kinetic parameters were determined by conventional isothermal model-fitting techniques. The data points plotted in Figure 17 and Figure 18 (see Appendix A) were used to calculate the integral form (g(α)) of the reaction models for each model shown in Table 2. The slope of g(α) versus t provided the reaction rate constants (k) for each model at different temperatures and concentrations. Microsoft Excel® was used for these calculations. The results from this process are shown in Appendix B, with the determination coefficients (R^2) included. The power law models (P2 – P4) and the Avarami-Erofeyev models (A2 – A4) exhibited poor fits with the experimental data as the average R^2 values for each of these models were < 0.8. Therefore, there is a higher variation in the experimental data and not enough data points fit the regression line to justify its slope. Hence, the slope (k) value may not accurately represent the experimental data.

The slopes (k) and R^2 values were determined using the data points up to 240 minutes reaction time. After 240 minutes, the leaching rate slows down dramatically and is no longer constant (see Figure 17 - Figure 18). The average R^2 values and the standard deviations from each temperature and concentration were calculated and are shown in Table 8 for the best fitting models. The data bars are used to visibly indicate the degree of goodness of fit between g(α) and time. Since the A and P models exhibited poor fits with the experimental data, these models were not likely to represent the leaching reaction very well and are excluded from Table 8.

The diffusion models (D1 – D4) exhibit the highest R^2 values and the smallest standard deviations. The high R^2 values indicate that there are smaller differences between the experimental data and the fitted values. The low standard deviations indicate that the values tend to be close to the mean, or expected value. Therefore, the diffusion models are expected to accurately represent the leaching reaction.

Table 8: Average R^2 values and standard deviations of each model for the g(α) vs time relationships.

Model	R^2	
	Average	Standard Deviation
g_{R2}	0.93	0.04
g_{R3}	0.95	0.03
g_{D1}	0.98	0.03
g_{D2}	0.98	0.02
g_{D3}	0.98	0.02
g_{D4}	0.98	0.01
g_{F0}	0.90	0.06
g_{F1}	0.96	0.04
g_{F2}	0.94	0.04
g_{F3}	0.92	0.08

k_0 and Ea values were determined from the reaction rate constants of the diffusion models (shown in Appendix B) for each temperature and concentration using equation 7b to determine whether the diffusion models obey the Arrhenius equation. Results were once again obtained using Microsoft Excel®. The full set of Arrhenius results is supplied in Appendix C. The average R^2 values and the standard deviations for the diffusion models from each temperature and concentration were calculated and are shown in Table 9 with data bars to visibly indicate linearity between lnk and 1/T.

Table 9: Average R^2 values and standard deviations of the diffusion models for the lnk vs 1/T relationships.

Model	R^2	
	Average	Standard Deviation
g_{D1}	0.99	0.02
g_{D2}	0.98	0.03
g_{D3}	0.97	0.03
g_{D4}	0.98	0.03

From Table 9, the diffusion models seem to exhibit strong correlations for the Arrhenius plot (high R^2 values) with small variations from the average values. If the R^2 values for the Arrhenius plot were low, this would mean that the data points don't really fit on a straight line, and since a straight-line relationship is used to determine k_0 and E_a, these values would not be very accurate. Overall, model D1 displays the strongest correlation and the smallest standard deviation, and since model D1 represents one-dimensional diffusion through a flat plate, it is selected as the model of choice to represent the leaching reaction.

To confirm that model D1 represents the reaction, the k values for model D1 were substituted into the differential form of its rate equation and integrated using Python® to find analytical solutions for conversion as a function of time. The predicted values accurately represent the experimental values as shown by the linear relationship between these variables in Figure 19.

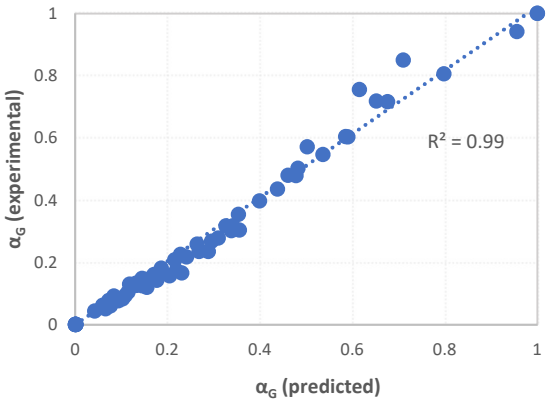

Figure 19: Relationship between α_G predicted from model D1 and α_G experimental.

The high R^2 value in Figure 19 indicates that most of the data points are close to or on the 1:1 line thereby satisfying the "perfect relationship" between the axes and confirming expectations that the predicted conversion values closely approximate the experimental data. Therefore, model D1, and its associated k_0 and Ea values were selected as the kinetic triplet to represent the leaching process. The Python® code used to model the reaction is shown in Appendix D, and the conversion-time plots comparing all the reaction models to the experimental data is shown in Appendix E.

Kinetic triplet relationships

It can be observed that the k_0 and Ea values vary with initial acid concentration (see Appendix C). The $\ln k_0$ and the Ea values for model D1 as a function of initial acid concentration are graphically illustrated in Figure 20. Both Ea and $\ln k_0$ exhibit linearity with respect to $[H^+]_0$ as indicated by the high R^2 values and can, therefore, be described by equation 15 and equation 16 for the preexponential factor and the activation energy, respectively.

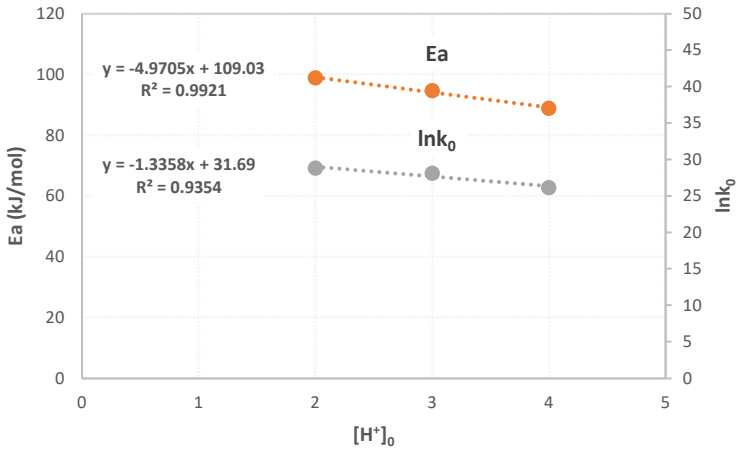

Figure 20: $\ln k_0$ and Ea relationships as functions of initial acid concentration for model D1.

$$k_0 = e^{(-1.3358[H^+]_0 + 31.69)}\ (\mathrm{min}^{-1}) \tag{15}$$

$$\mathrm{Ea} = -4.9705[H^+]_0 + 109.03\ (\mathrm{kJ\ mol}^{-1}) \tag{16}$$

As shown in Figure 20, the activation energies observed decrease with an increase in acid concentration. As previously discussed, the more H^+ ions present in solution, the higher the reaction rate due to the high probability of collisions. Since activation energy is inversely related to the rate

constant, this explains the decrease in activation energy. Activation energy dependence on pH has been discussed by Dockrey and Mattson (2016), and Kalinowski and Schweda (1996).

4.2.1.3. Simulation Tests of Conversion Model

A simulation was done to assess the accuracy of the leaching model. The model was tested with additional experimental data points obtained from the experimental conditions shown in Figure 6. The "testing data" is provided in Appendix F. Equation 15 and equation 16 were employed to model the reactions at 2.4 M and 2.6 M as shown in the Python® code (Appendix G).

Figure 21 shows that there is a relatively strong correlation between the predicted conversion and the experimental conversion for the testing data which further confirms that the D1 model describes the leaching reaction and that equation 15 and equation 16 describe the preexponential constant and activation energy dependencies on initial acid concentration.

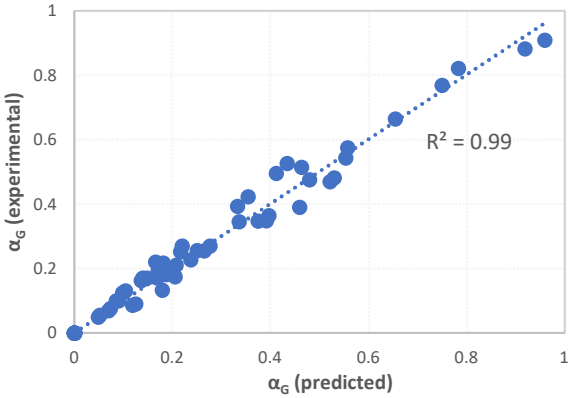

Figure 21: Relationship between α_G predicted from the reaction model and α_G experimental from the testing data.

All the experimental conversion data (from the initial modelling experiments and the testing experiments) are plotted over time with the modelled analytical solutions for each temperature and concentration in Figure 22.

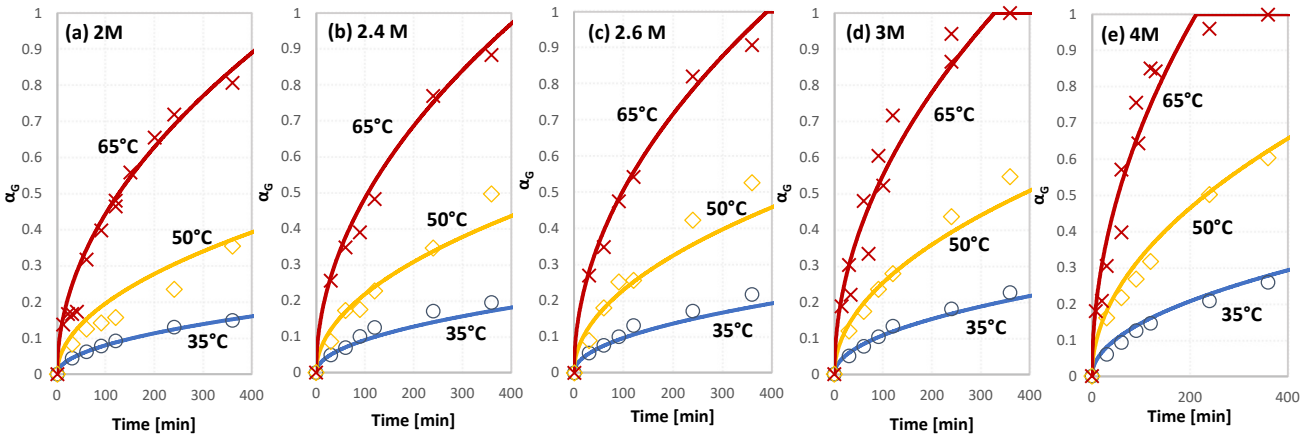

Figure 22: Conversion-time plots showing all experimental data points fitted to the modelled curves.

4.2.2. Leach Liquor

This section describes how the leach liquor was mainly used to verify observations from analysing the solids. The concentrations of leach liquors from different leaching stages were used to determine elemental conversions for individual elements compared to those from XRF. The volumetric conversion data was used to verify that all cations extracted from the solids were recovered in the solution. The [H^+] concentration data of the leach liquors were used to determine whether the amount of acid consumed is equivalent to the amount theoretically required.

4.2.2.1. Elemental Conversion

Since the weights of the individual elements in the solid residue are not easily measured, the leach liquor was analysed. ICP-OES was used to determine the concentrations of the cations in solution. According to Härkönen and Keiski (1984), Kalinowski and Schweda (1996), Kuwahara and Aoki (1995), Lin and Clemency (1981), Mamy (1970), and Wypych *et al*. (2005), potassium is preferentially extracted from phlogopite during leaching, therefore, its conversion rate is faster than the conversions of the other elements and the overall conversion of the sum of the cationic masses. This is shown in Figure 23, where the elemental conversions were calculated from ICP-OES data using equation 4.

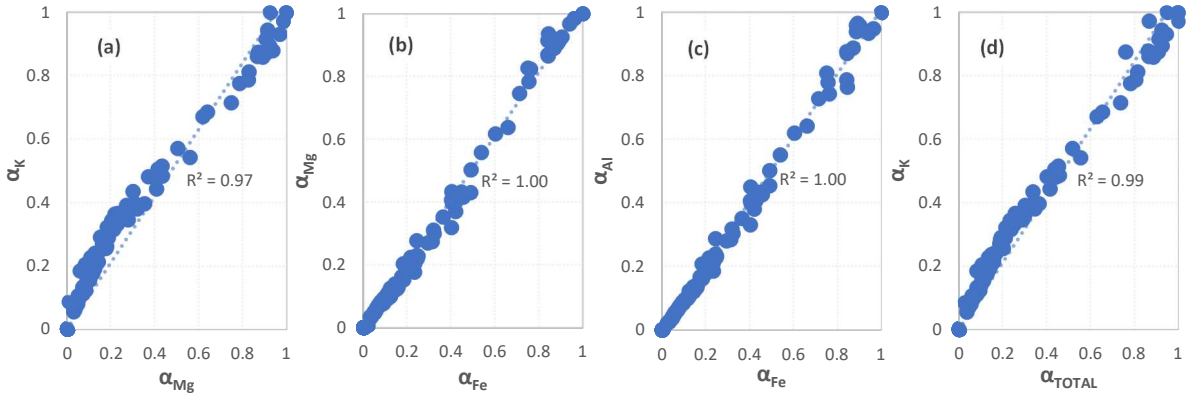

Figure 23: Elemental volumetric conversion relationships.

Since the K^+ ions are weakly bonded to the interlayer of the phlogopite structure (Rieder *et al*., 1998), they are easily accessible to acid attack and are readily available to be extracted. The weaker bond strengths indicate that less energy is required to break these bonds. Therefore, the activation energy for potassium conversion is expected to be less than that of the overall conversion. Conversely, the stronger bonds occurring in the T-O-T layers are responsible for the slower reaction rates as shown in Figure 23.

The direct proportionality between the conversion data of Mg^{2+}, Fe^{3+} and Al^{3+} in Figure 23 (b) and (c) implies that these cations are extracted at similar rates. It is clear, from Figure 23 (a) and (d), that K^+ is extracted faster than Mg^{2+}, and thus, faster than the other cations as well, especially at the start of the leaching process (for lower α values). All conversion data points exhibit linearity for higher α values, indicating that all cations are released at the same rate after prolonged leaching. The general descending order of the cation release rates is K^+ > (Mg^{2+}, Fe^{3+}, Al^{3+}), or $\alpha_K > \alpha_{TOTAL} > \alpha_{Mg,\ Fe,\ Al}$ in terms of conversion.

The trends exhibited in Figure 23 are similar to those observed in Figure 7 which were obtained from XRF data.

4.2.2.2. Gravimetric conversion versus volumetric conversion

The ICP-OES data was used to determine the volumetric elemental conversions of the leached species. The volumetric conversion (α_V) was calculated using equation 5. To confirm the accuracy of the different data sets against each other as shown in Figure 24.

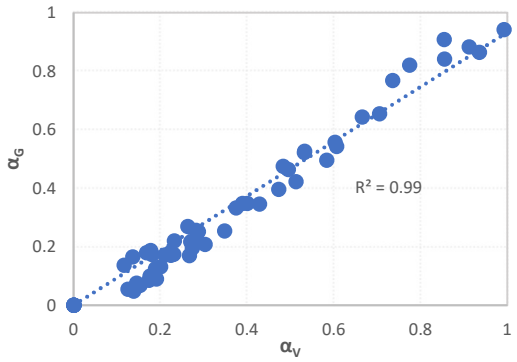

Figure 24: Comparison between gravimetric conversion and volumetric conversion.

A sufficient correlation is observed as the coefficient of determination (R^2) indicates that 99 % of the data fall on the regression line, and thus, are relatively proportional to one another. This confirms that the mass lost from the solid residues are recovered in the leach liquor solutions. The data plotted in Figure 24 was obtained from the leaching "test" experiments.

4.2.2.3. Acid Consumption

To determine whether the reaction (equation 14) proceeds stoichiometrically, [H^+] data of leach liquor solutions were plotted over time as shown in Figure 25. The experiments were conducted at 65 °C using different initial acid concentrations as indicated. The raw data is provided in Appendix H.

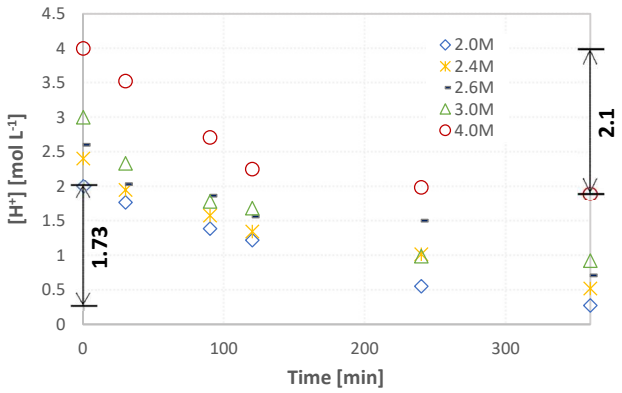

Figure 25: Experimental [H^+] data plotted over time for different initial acid concentrations.

As shown in Figure 25, the amount of acid consumed is inequivalent to the amount theoretically required. For example, based on the stoichiometric relationships in equation 14, and the quantities of each compound present in the raw phlogopite (Table 7), 2.45 M HNO_3 is required to react with 20 g of phlogopite using an S:L of 1:10 g mL^{-1}. However, a maximum value of only 2.1 M is consumed when 4 M HNO_3 is used for leaching. When 2.4 M and 2.6 M HNO_3 are used, only 1.75 and 1.90 M HNO_3 are consumed, respectively, leaving behind some excess H^+ ions in solution. This could be due to the fact that the theoretical [H^+] required was based on equation 14, which assumes that the cations present in solution have charges equal to the valence of those elements. However, the chemistry of certain elements, such as titanium and aluminium, in aqueous solution are complex and could form species

such as TiO^{2+} and $Al_2(OH)_2^{4+}$ in solution, which would consume less acid than initially expected. Another factor that may contribute to the observed inequivalence is the oxidation state of iron in the phlogopite. A large fraction may actually be present as Fe^{2+} and not Fe^{3+} requiring less acid to be extracted. The form of equation 14 suggests that the Fe is present in the octahedral position with Mg^{2+} suggesting that most of the iron may be present as Fe^{2+}. In addition, the oxidation of Fe^{2+} to Fe^{3+} would involve the release of brownish-coloured NO_2 gas, which was observed during experimentation. Figure 25 also shows how the leaching rates increase (steeper slopes) with acid concentration as more H^+ ions are consumed over time, up to a certain point (~120 minutes for $[H^+]_0$ = 4 M), whereby the acid consumption rate remains relatively constant.

5. Conclusion and Recommendations

All analyses revealed complementary results concerning the cationic extractions. It was found that the samples exhibit decreased cationic content, as expected, with leaching and that the raw phlogopite undergoes structural degradation due to the removal of the Mg^{2+}, Fe^{3+} and Al^{3+} cations (FTIR, XRD, SEM-EDS) resulting in the formation of an amorphous silica product. Sample LP3 is almost completely SiO_2, with <5 % of the other components present (XRF). The potassium content was released at a faster rate than the Al, Mg and Fe contents, as expected since the K^+ ions occupy the interlayer sites of the phlogopite and are, therefore, more susceptible to proton attack than the other cations (XRF, ICP). The acid then permeates through the tetrahedral and octahedral sheets, resulting in the release of the remaining cations from the phlogopite structure (SEM-EDS). The presence of microfractures on the surface of the particles provides additional access pathways for proton attack, thereby increasing leaching rates (SEM-EDS, BET) despite the high crystallinity (XRD) and low surface area (BET, TGA) of the raw phlogopite. The presence of Mg, Fe and Al contents in relatively large quantities (XRF) in the raw phlogopite also enhances leaching rates (Okada *et al*., 2006).

Since the raw phlogopite is highly crystalline (XRD), the absence of defects in the lattice means that the motion of H^+ ions permeating into the lattice is restricted (Ropp, 2003; Schmalzried, 1995). This strongly suggests that the leaching is internal diffusion-controlled since the mobility of constituents into the system is the controlling factor, and since the phlogopite particles are plate-like (SEM-EDS, BET) in shape (representative of a flat plane whereby the particle thickness is much smaller than its length), the use of the D1 model for one-dimensional diffusion through a flat plate is the recommended model to represent the leaching process.

The use of the D1 model was further confirmed by the strong regression of g(α) over time and of the Arrhenius plot. Simulation tests also revealed strong linearity between the experimental conversion data and the predicted conversion values obtained from the D1 model. Therefore, the kinetic triplet selected accurately approximates what occurs experimentally for the overall conversion.

Since phlogopite is a rich source of potassium, among other desirable elements, it could be useful in the fertiliser industry (Said *et al*., 2018; da Silva *et al*., 2008; van Straaten, 2002). It was observed that leaching phlogopite with HNO_3 results in the extraction of virtually all cations into solution, leaving SiO_2 residue. However, the leach liquor produced has a pH < 0 with excess H^+ ions in solution (see Section 4.2 - Figure 25). Therefore, extra OH^- ions would be required to neutralise the leach liquor if fertiliser is the desired final product. When the phlogopite is leached with the theoretically required molar concentration, less than 80 % of the cations are extracted into solution (Kgokong, 2017). Thus, the leaching process should be optimised so that the acidity of the leach liquor is minimised while obtaining complete leaching of all cations from the phlogopite particles into solution.

The efficiency of the leaching process could be improved by countercurrently reacting the phlogopite with leaching acid (of the theoretically required concentration to achieve complete conversion) in sequential semi-batch reactors, or by reacting phlogopite with fresh leach liquor in several subsequent steps until the phlogopite is completely leached. This would decrease the H^+ content and increase the concentrations of the extractable cations in solution.

To predict the conversion behaviours of the individual cations into solution, these cations (K^+, Mg^{2+}, Fe^{3+}, Al^{3+}) should be modelled in a similar manner as the overall conversion. A relationship should also be established between [H^+] as a function of its dependent variables. Furthermore, since the SiO_2 by-

product is highly porous (surface area of 517 m^2 g^{-1}), its application in industrial adsorbents, catalysts, polymers, pigments, cement, etc. should be further explored.

Although model D1 was found to provide an accurate representation of the leaching process, a plethora of models exists to describe solid-state kinetics. Therefore, the application of other models, or even isoconversional (model-free) methods could also be explored. Moreover, a complementary approach involving a combination of isoconversional and model-fitting methods (Khawam and Flanagan, 2005) could be attempted.

Lastly, since cracks in the particle surfaces increase leaching rates, methods of solid preparation should be explored whereby the number of surface cracks is increased while retaining the favourable physical properties of the material.

6. References

Adebayo, A.O. (2014) "Development of Kinetic Parameters for the Dealumination of Kaolinite Clay". Covenant University, Nigeria.

Apua, C., Kime, M.B. and Mukuna Patrick, M. (2013) "A Study of Leaching of Copper Oxide Ore by Sulphuric Acid", in: Proceedings of the 52nd Conference of Metallurgists (COM), paper presented at *Materials Science Technology Conference (MS&T)*, 27-31 October 2013, Montréal, Québec, Canada.

Awazu, K. (1999) "Oscillator strength of the infrared absorption band near 1080 cm^{-1} in SiO_2 films" *Journal of Non-Crystalline Solids*, 260 (2-3), 242–244.

Baedecker, P.A. (1987) "Methods for Geochemical Analysis", U.S. Geological Survey Bulletin, USA.

Baksheev, I., Damian, F., Damian, G., Prokof'ev, V., Bryzgalov and I., Marushchenko, L. (2016) "Chemical composition of phlogopite, tourmaline and illite from hydrothermal alterations of the Nistru deposit, Baia Mare, Romania" *Carpathian journal of earth and environmental sciences*, 11 (2), 547–564.

Balland, C., Poszwa, A., Leyval, C and, Mustin, C. (2010) "Dissolution rates of phyllosilicates as a function of bacterial metabolic diversity" *Geochimica et Cosmochimica Acta,* 74(19), 5478–5493.

Barabaszová, K.Č. and Valášková, M. (2013) "Characterization of vermiculite particles after different milling techniques" *Powder Technology*, 239, 277–283.

Bardestani, R., Patience, G.S. and Kaliaguine, S. (2019) "Experimental methods in chemical engineering: specific surface area and pore size distribution measurements—BET, BJH, and DFT" *The Canadian Journal of Chemical Engineering,* 97 (11), 2781–2791.

Barrett, E.P., Joyner, L.G. and Halenda, P.P. (1951) "The determination of pore volume and area distributions in porous substances. I. Computations from nitrogen isotherms" *Journal of the American Chemical Society*, 73 (1), 373–380.

Basmadjian, D. (2007) *Mass Transfer and Separation Processes: Principles and Applications*, 2nd ed. CRC Press: Taylor & Francis Group, LLC, Broken Sound Parkway, NW.

Bautista, R.G. (1974) "Hydrometallurgy" *Advances in Chemical Engineering*, 9 (1), 1–110.

Benedictus, A., Berendsen, P. and Hagni, A. (2008) "Quantitative characterisation of processed phlogopite ore from Silver City Dome District, Kansas, USA, by automated mineralogy" *Minerals Engineering*, 21 (15), 1083–1093.

Beran, A. (2002) "Infrared Spectroscopy of Micas" *Reviews in Mineralogy and Geochemistry*, 46 (1), 351–369.

Besson, G. and Drits, V.A. (1997) "Refined relationships between chemical composition of dioctahedral fine-grained mica minerals and their infrared spectra within the OH stretching region. Part I: Identification of the OH stretching bands" *Clays and Clay Minerals*, 45 (2), 158–169.

Biedermann, A.R., Bender Koch, C., Lorenz, W.E.A. and Hirt, A.M. (2014) "Low-temperature magnetic anisotropy in micas and chlorite" *Tectonophysics*, Methods and applications of magnetic anisotropy: A tribute to Graham Borradaile, 629, 63–74.

Bigham, J.M., Bhatti, T.M., Vuorinen, A. and Tuovinen, O.H. (2001) "Dissolution and structural alteration of phlogopite mediated by proton attack and bacterial oxidation of ferrous iron" *Hydrometallurgy*, 59 (2), 301–309.

Booth, F. (1948) "A note on the theory of surface diffusion reactions" *Transactions of the Faraday Society*, 44, 796–801.

Boss, C.B. and Fredeen, K.J. (2004) *Concepts, Instrumentation and Techniques in Inductively Coupled Plasma Optical Emission Spectrometry*, 3rd ed. PerkinElmer, Inc., USA.

Boundless (2020) “Biology LibreTexts: Diffusion” https://bio.libretexts.org/@go/page/13086 [2021, April 4].

Brindley, G.W. (1952) "Identification of clay minerals by x-ray diffraction analysis" *Clays and Clay Minerals,* 1 (1), 119–129.

Brown, M.E. (2005) "Stocktaking in the kinetics cupboard" *Journal of Thermal Analysis* and Calorimetry, 82 (3), 665–669.

Brunauer, S., Emmett, P.H. and Teller, E. (1938) "Adsorption of gases in multimolecular layers" *Journal of the American Chemical Society*, 60 (2), 309–319.

Burnham, A.K., Weese, R.K. and Weeks, B.L. (2004) “A distributed activation energy model of thermodynamically inhibited nucleation and growth reactions and its application to the β−δ phase transition of HMX” *The Journal of Physical Chemistry B*, 108 (50), 19432–19441.

Bybkov, V.I. (2002) *Reaction Diffusion and Solid State Kinetics*, The IPMS Publications, Kyiv.

Castilhos, R.M.V. and Meurer, E.J. (2001) "Potassium release kinetics in a Planosol of the state of Rio Grande do Sul" *Ciência Rural*, 31 (6), 979–983.

Chen, F., Lu, S. and Ding, X. (2018) Pore types and quantitative evaluation of pore volumes in the Longmaxi Formation shale of southeast Chongqing, China" *Acta Geologica Sinica* - English Edition, 92 (1), 342–353.

Chezom, D., Chimi, K., Choden, S., Wangmo, T. and Gupta, D.S.K. (2013) "Comparative study of different leaching procedures" *International Journal of Engineering Research and General Science*, 1 (2), 23-28.

Chute, J.H. and Quirk, J.P. (1967) "Diffusion of potassium from mica-like clay minerals" *Nature*, 213 (5081), 1156–1157.

Ciullo, P.A. (1996) "Mica", in: *Industrial Minerals and Their Uses - A Handbook and Formulary*, William Andrew Publishing/Noyes, Westwood, N.J., pp. 45–48.

Costa, T.M.H., Gallasa, M.R., Benvenutti, E.V. and da Jornada, J.A.H. (1997) "Infrared and thermogravimetric study of high pressure consolidation in alkoxide silica gel powders" *Journal of Non-Crystalline Solids*, 220 (2-3), 195–201.

Cullity, B.D. (1956) *Elements of X-Ray Diffraction*, Addison-Wesley, Massachusetts.

da Silva, A. d A.S., França, S.C.A., Ronconi, C.M., Sampaio, J.A., da Luz, A.B. and da Silva, D. (2008) “A study on the application of phlogopite as a slow release potassium fertilizer”, Institute of Chemistry - Federal University of Rio de Janeiro, San Juan, Argentina.

da Silva, A. d A.S., Sampaio, J.A., da Luz, A.B., França, S.C.A. and Ronconi, C.M. (2013) “Modeling controlled potassium release from phlogopite in solution: exploring the viability of using crushed phlogopitite rock as an alternative potassium source in Brazilian soil” *Journal of the Brazilian Chemical Society*, 24 (8), 1366–1372.

Deer, W., Howie, R. and Zussman, J. (1992) *An Introduction to the Rock-Forming Minerals*, 2nd ed. Longman Scientific & Technical, Harlow, Essex, England.

del Rey-Perez-Caballero, F. and Poncelet, G. (2000) "Preparation and characterization of microporous 18 Å Al-pillared structures from natural phlogopite micas" *Microporous and Mesoporous Materials*, 41 (1), 169–181.

Derry, R. (1978) "The Extraction of Uranium from Ores", in: Proceedings of European Aspects of the Technology and Economics of Uranium, paper presented at *Effective Management of the Nuclear Power Fuel Cycle*, International Business Communications Ltd.

Deysel, H.M., Berluti, K., du Plessis, B.J. and Focke, W.W. (2020) "Glass foams from acid-leached phlogopite waste" *Journal of Materials Science*, 55 (19), 8050–8060.

Dockrey, J. and Mattson, B. (2016) "Effects of pH on the Arrhenius paradigm", in: Proceedings IMWA, paper presented at *the Mining Meets Water – Conflicts and Solutions*, 2016, Freiberg/Germany, p. 7.

Dybkov, V.I. (2002) *Reaction Diffusion and Solid State Chemical Kinetics*. The IPMS Publications, Kyiv.

Dye, D.W. and Hartshorn, L. (1924) "The dielectric properties of mica" Proceedings of the Physical Society of London, 37 (1), 42–57.

Eriksson, S.C. (1982) "Aspects of the petrochemistry of the Phalaborwa complex", Northeastern Transvaal, University of the Witwatersrand, South Africa.

Farmer, V.C. (1974) *The Infrared Spectra of Minerals*, Mineralogical Society (Mineralogical Society monograph, 4), London.

Farmer, V.C. and Russell, J.D. (1964) "The infra-red spectra of layer silicates" *Spectrochimica Acta*, 20 (7), 1149–1173.

Favel, C.M. (2018) "The beneficiation of the leach liquor of phlogopite" Department of Chemical Engineering, University of Pretoria, Pretoria.

Fogler, H.S. (2006) "Rate Laws and Stoichiometry" in: *Elements of Chemical Reaction Engineering*, Prentice-Hall, Boston, pp. 91–92.

Foster, M. (1960) "Interpretation of the Composition of Trioctahedral Micas" United States Department of the Interior, Washington.

Friedman, H. (2019) "The mineral and gemstone kingdom. The mineral Phlogopite" https://www.minerals.net/mineral/phlogopite.aspx [2019, September 20].

Ganie, N. (2018) "Beneficiation of Phlogopite Leach Liquor", Master of Engineering (Chemical Engineering), Department of Chemical Engineering, University of Pretoria, Pretoria.

Ganie, N. and du Plessis, B.J. (2015) "Kinetics and optimum conditions for the leaching of phlogopite", Department of Chemical Engineering, University of Pretoria, Pretoria.

Geankoplis, C. (1993) *Transport Processes and Unit Operations*, 3rd ed. Prentice-Hall International. Inc., Englewood Cliffs, New Jersey.

Giletti, B.J. and Anderson, T.F. (1975) "Studies in diffusion, II. Oxygen in phlogopite mica" *Earth and Planetary Science Letters,* 28 (2), 225–233.

Gilkes, R.J. and Suddhiprakarn, A. (1975) "The influence of potassium level in extracting solution on the nature of alteration products present in potassium-depleted biotite", paper presented at *the International Clay Conference,* pp. 611–622.

Graetz, J. and Reilly, J.J. (2005) "Decomposition kinetics of the AlH_3 polymorphs" *The Journal of Physical Chemistry B*, 109 (47), 22181–22185.

Grim, R.E. (1968) *Clay Mineralogy*, 2nd ed. McGraw-Hill, New York.

Härkönen, M.A. and Keiski, R.L. (1984) "Porosity and surface area of acid-leached phlogopite: The effect of leaching conditions and thermal treatment" *Colloids and Surfaces*, 11 (3), 323–339.

Heckroodt, R.O. (1991) "Clay and clay materials in South Africa" *Journal of the South African Institute of Mining and Metallurgy*, 91 (10), 343–363.

IAEA (1993) "Uranium Extraction Technology", Technical Reports, Series No. 359. IAEA (International Atomic Energy Agency), Vienna.

Jenkins, D.M. (1989) "Empirical study of the infrared lattice vibrations (1100-350 cm^{-1}) of phlogopite" *Physics and Chemistry of Minerals*, 16, 408–414.

Joseph, L. (2019) "Goodness of Fit in Linear Regression" McGill University.

Kalinowski, B.E. and Schweda, P. (1996) "Kinetics of muscovite, phlogopite, and biotite dissolution and alteration at pH 1–4, room temperature" *Geochimica et Cosmochimica Acta*, (3) 60, 367–385.

Kaviratna, H. and Pinnavaia, T.J. (1994) "Acid hydrolysis of octahedral Mg2+ sites in 2:1 layered silicates: An assessment of edge attack and gallery access mechanisms" *Clays and Clay Minerals*, 42 (6), 717–723.

Kgokong, G.O. (2017) "Beneficiation of phlogopite: The mysterious hydrogen ion" University of Pretoria, Pretoria.

Khalighi, M. and Minkkinen, P. (1989) "The evaporation of potassium from phlogopite" *Journal of Thermal Analysis*, 35 (2), 379–390.

Khandpur, D.R.S. (2006) *Handbook of Analytical Instruments*, 2nd ed. McGraw-Hill Education, India.

Khawam, A. (2007) "Application of solid-state kinetics to desolvation reactions", University of Iowa.

Khawam, A. and Flanagan, D.R. (2006) "Solid-state kinetic models: Basics and mathematical fundamentals" *The Journal of Physical Chemistry*, 110 (35), 17315–17328.

Khawam, A. and Flanagan, D.R. (2005) "Complementary use of model-free and modelistic methods in the analysis of solid-state kinetics" *The Journal of Physical Chemistry B*, 109 (20), 10073–10080.

Kim, A.G. (2002) "CCB leaching summary: Survey of methods and results", in: Proceedings: Coal Combustion By-Products and Western Coal Mines: A Technical Interactive Forum. pp. 16–18.

Kloprogge, J.T. and Frost, R.L. (1999) "Fourier transform infrared and Raman spectroscopic study of the local structure of Mg-, Ni-, and Co-hydrotalcites" *Journal of Solid State Chemistry*, 146 (2), 506–515.

Kosuge, K., Shimada, K. and Tsunashima, A. (1995) "Micropore formation by acid treatment of antigorite" *Chemistry of Materials*, 7 (12), 2241–2246.

Kotz, J.C., Treichel, P.M. and Townsend, J.R. (2012) *Chemistry and Chemical Reactivity*, 8th ed. Brooks/Cole Cengage Learning, USA.

Kraevskaya, S.N., Belomestnova, É.N. and Zhuravlev, G.I. (1985) "Glass crystalline materials based on phlogopite" *Glass and Ceramics*, 42 (9), 396–399.

Kuwahara, Y. and Aoki, Y. (1995) "Dissolution process of phlogopite in acid solutions" *Clays and Clay Minerals*, 43 (1), 39–50.

Labani, M.M., Rezaee, R., Saeedi, A. and Hinai, A.A. (2013) "Evaluation of pore size spectrum of gas shale reservoirs using low pressure nitrogen adsorption, gas expansion and mercury porosimetry: A case study from the Perth and Canning Basins, Western Australia" *Journal of Petroleum Science and Engineering*, 112, 7–16.

Lammers, K., Smith, M.M. and Carroll, S.A. (2017) "Muscovite dissolution kinetics as a function of pH at elevated temperature" *Chemical Geology*, 466, 149–158.

Leonard, R.A. and Weed, S.B. (1970) "Mica weathering rates as related to mica type and composition" *Clays and Clay Minerals*, 18 (4), 187–195.

Levenspiel, O. (1999) "Fluid-Particle Reactions: Kinetics", in: *Chemical Reaction Engineering*, Wiley, New York.

Lin, F. C. and Clemency, C.V. (1981) "Dissolution kinetics of phlogopite. I. Closed system" *Clays and Clay Minerals*, 29 (2), 101–106.

Liong, K.K., Wells, P.A. and Foster, N.R. (1991) “Diffusion in supercritical fluids” *The Journal of Supercritical Fluids*, 4 (2), 91–108.

Madejová, J. and Komadel, P. (2001) "Baseline studies of the clay minerals society source clays: Infrared methods" *Clays and Clay Minerals*, 49 (5), 410–432.

Mamy, J. (1970) "Extraction of interlayer K from phlogopite specific effects of cations role of Na and H concentrations in extraction solutions" *Clays and Clay Minerals*, 18 (3), 157–163.

McDonald, J.H. (2020) “Linear Regression and Correlation”, https://stats.libretexts.org/@go/page/1746 [2021, April 25].

Mendelovici, E., Frost, R.L. and Kloprogge, J.T. (2001) "Modification of chrysotile surface by organosilanes: An IR–photoacoustic spectroscopy study" *Journal of Colloid and Interface Science*, 238 (2), 273–278.

Mgbeahuruike, L.U., Barrett, J., Potgieter, H.J., van Dyk, L. and Potgieter-Vermaak, S.S. (2019) "A comparison of batch, column and heap leaching efficiencies for the recovery of heavy metals from artificially contaminated simulated soil" *Journal of Environmental Protection*, 10, 632–650.

Michot, L.J. and Villiéras, F. (2013) "Chapter 2.10 - Surface Area and Porosity", in: Bergaya, F. and Lagaly, G. (Eds.), *Developments in Clay Science*, *Handbook of Clay Science*, Elsevier, pp. 319–332.

Micromeritics (2016) "Micrometrics Tristar II Surface Area and Porosity Instrument Brochure", Micromeritics Instrument Corporation.

Milliken, K.L., Rudnicki, M., Awwiller, D.N. and Zhang, T. (2013) "Organic matter–hosted pore system, Marcellus Formation (Devonian), Pennsylvania Geohorizon" AAPG Bulletin, 97 (2), 177–200.

Mortland, M.M. (1958) "Kinetics of potassium release from biotite" *Soil Science Society of America Journal*, 22 (6), 503–508.

Niu, H., Kinnunen, P., Sreenivasan, H., Adesanya, E. and Illikainen, M. (2020) "Structural collapse in phlogopite mica-rich mine tailings induced by mechanochemical treatment and implications to alkali activation potential" *Minerals Engineering*, 151, 106331.

Ocaña, M., Fornés, V. and Serna C.J. (1989) "The variability of the infrared powder spectrum of amorphous SiO2" *Journal of Non-Crystalline Solids*, 107 (2-3), 187–192.

Okada, K., Arimitsu, N., Kameshima, Y., Nakajima, A. and MacKenzie, K.J.D. (2006) "Solid acidity of 2:1 type clay minerals activated by selective leaching" *Applied Clay Science*, 31 (3), 185–193.

Okada, K., Arimitsu, N., Kameshima, Y., Nakajima, A. and MacKenzie, K.J.D. (2005) "Preparation of porous silica from chlorite by selective acid leaching" *Applied Clay Science*, 30 (2), 116–124.

Okada, K., Nakazawa, N., Kameshima, Y., Yasumori, A., Temuujin, J., MacKenzie, K.J.D. and Smith, M.E. (2002) "Preparation and porous properties of materials prepared by selective leaching of phlogopite" *Clays and Clay Minerals*, 50 (5), 624–632.

Okada, K., Shimaia, A., Takeia, T., Hayashia, S., Yasumori, A. and MacKenzie, K.J.D. (1998) "Preparation of microporous silica from metakaolinite by selective leaching method" *Microporous and Mesoporous Materials*, 21 (4-6), 289–296.

Perry, R.H. and Green, D.W. (1999) *Perry's Chemical Engineers' Handbook*, 7th ed. McGraw-Hill, New York.

Peterson, V.K., Neumann, D.A. and Livingston, R.A. (2005) "Hydration of tricalcium and dicalcium silicate mixtures studied using quasielastic neutron scattering" *The Journal of Physical Chemistry B*, 109 (30), 14449–14453.

Poling, B.E., Prausnitz, J.M. and O'Connell, J.P. (2001) "Diffusion Coefficients", in: *The Properties of Gases and Liquids*, McGraw-Hill Professional, New York, p. 11.1-11.55.

Porteus, M. (2018) "History and Future of Phosphate Mining and Beneficiation in South Africa" Beneficiation of Phosphates VIII. Foskor, South Africa.

Procópio, A.M.S., Ferreira, E.J.C., Oliveira, L.G., de Barros, M., de Freitas, M.R., da Silva and M.C., Moura Filho, F. (2020) "Caracterização de flogopita para processamento de filtros cerâmicos porosos pelo método da réplica" *Cerâmica*, 66 (380), 433–439.

Qiao, Y., Qiao, R., He, Y., Shi, C., Liu, Y., Hao, H., Su, J. and Zhong, J. (2017) Instrumental analytical techniques for the characterization of crystals in pharmaceutics and foods" *Crystal Growth & Design*, 17, 6138–6148.

Rausell-Colom, J A, Sweatman, T.R., Wells, C.B. and Norrish, K. (1965) "Studies in the Artificial Weathering of Mica", in: Hallworth, E.G. and Crawford, D.V. (Eds.), *Experimental Pedology*, Butterworths, pp. 40–72.

Reed, M.G. and Scott, A.D. (1962) "Kinetics of potassium release from biotite and muscovite in sodium tetraphenylboron solutions" *Soil Science Society of America Journal*, 26 (5), 437–440.

Reguir, E., Chakhmouradian, A., Halden, N., Malkovets, V. and Yang, P. (2009) "Major- and trace-element compositional variation of phlogopite from kimberlites and carbonatites as a petrogenetic indicator" *Lithos*, 112, 372–384.

Richardson, J., Harker, J. and Backhurst, J. (2002) *Coulson & Richardson's Chemical Engineering: Particle Technology and Particle Technology and Separation Processes*, 5th ed. Butterworth-Heinemann, Woburn, MA.

Rieder, M., Cavazzini, G., D'yakonov, Y.S., Frank-Kamenetskii, V.A., Gottardi, G., Guggenheim, S., Koval', P.W., Müller, G., Neiva, A.M.R., Radoslovich, E.W., Robert, J.-L., Sassi, F.P., Takeda, H., Weiss, Z. and Wones, D.R. (1998) "Nomenclature of the micas" *Clays and Clay Minerals*, 46 (5), 586–595.

Rogers, K. (2012) "Scientific modeling", in Encyclopedia Britannica. URL https://www.britannica.com/science/scientific-modeling [2020, 18 August].

Ropp, R.C. (2003) *Solid State Chemistry*, 1st ed. Elsevier Science B.V., New Jersey, USA.

Ross, G.J. and Rich, C.I. (1973) "Effect of particle thickness on potassium exchange from phlogopite" *Clays and Clay Minerals*, 21 (2), 77–81.

Rouquerol, J., Avnir, D., Fairbridge, C.W., Everett, D.H., Haynes, J.M., Pernicone, N., Ramsay, J.D.F., Sing, K.S.W. and Unger, K.K. (1994) "Recommendations for the characterization of porous solids (Technical Report)" *Pure and Applied Chemistry*, 66 (8), 1739–1758.

Rouquerol, J., Llewellyn, P., Maurin, G., Sing, K.S.W. and Rouquerol, F. (2013*) Adsorption by Powders and Porous Solids: Principles, Methodology and Applications*, Elsevier Science & Technology, London, United Kingdom.

Russell, J.D. and Fraser, A.R. (1994) "Clay Mineralogy: Spectroscopic and Chemical Determinative Methods", in: Wilson, M.J. (Ed.), *Infrared Methods*, Chapman & Hall, London, pp. 11–67.

Sahoo, R.N., Naik, P.K. and Das, S.C. (2001) "Leaching of manganese from low-grade manganese ore using oxalic acid as reductant in sulphuric acid solution" *Hydrometallurgy*, 62 (3), 157–163.

Said, A., Zhang, Q., Qu, J., Liu, Y., Lei, Z., Hu, H. and Xu, Z. (2018) "Mechanochemical activation of phlogopite to directly produce slow-release potassium fertilizer" *Applied Clay Science*, 165, 77–81.

Schipper, I. and Cowan, R. (2018) "Global Mica Mining", Stichting Onderzoek Multinationale Ondernemingen (SOMO): Centre for Research on Multinational Corporations, Netherlands.

Schmalzried, H. (1995) *Chemical Kinetics of Solids*, VCH Verlagsgesellschaf; VCH Publishers, Weinheim.

Schoeman, J.J. (1989) "Mica and vermiculite in South Africa" *Journal of the Southern African Institute of Mining and Metallurgy*, 89 (1), 1–12.

Schweitzer, P.A. (1979) *Handbook of Separation Techniques for Chemical Engineers*, McGraw-Hill, New York.

Scordari, F., Ventruti, G., Sabato, A., Bellatreccia, F., Ventura, G. and Pedrazzi, G. (2006) "Ti-rich phlogopite from Mt. Vulture (Potenza, Italy) investigated by a multianalytical approach: Substitutional mechanisms and orientation of the OH dipoles" *European Journal of Mineralogy*, 18, 379–391.

Seader, J.D. and Henley, E.J. (2006) "Chapter 16: Leaching and Washing", in: *Separation Process Principles*, John Wiley & Sons, Inc., Hoboken, NJ, pp. 623–642.

Šesták, J. and Berggren, G. (1971) "Study of the kinetics of the mechanism of solid-state reactions at increasing temperatures" *Thermochimica Acta*, 3 (1), 1–12.

Sethurajan, M., van Hullebusch, E.D., Fontana, D., Akcil, A., Deveci, H., Batinic, B., Leal, J.P., Gasche, T.A., Kucuker, M.A., Kuchta, K., Neto, I.F.F., Soares, H.M.V.M. and Chmielarz, A. (2019) "Recent advances on hydrometallurgical recovery of critical and precious elements from end of life electronic wastes - a review" *Environmental Science and Technology*, 43 (3), 212–275.

Severin, K.P. (Ed.) (2004) "Energy Dispersive Spectrometry", in: *Energy Dispersive Spectrometry of Common Rock Forming Minerals*, Springer Netherlands, Dordrecht, pp. 1–13.

Sijakova-Ivanova, T. and Cukovska, L.R. (2016) "Mineralogical characteristics of phlogopite from Dupen kamen, Republic of Macedonia" *IOSR Journal of Applied Geology and Geophysics*, 4 (5), 72–76.

Sing, K.S.W. (1985) "Reporting physisorption data for gas/solid systems with special reference to the determination of surface area and porosity (Recommendations 1984)" *Pure and Applied Chemistry*, 57 (4), 603–619.

Sing, K.S.W. (1982) "Reporting physisorption data for solid/gas systems with special reference to the determination of surface area and porosity" *Pure and Applied Chemistry*, 51 (11), 2201–2218.

Skoog, D.A., Holler, F.J. and Crouch, S.R. (2007) *Principles of Instrumental Analysis*, 6th ed., Thomson Brooks/Cole, Belmont, CA.

Smit, D.S. (2001) "The leaching behaviour of a Ni-Cu-Co sulphide ore in an oxidative pressure-acid medium" University of Potchefstroom, Potchefstroom.

Sohn, H.Y. and Wadsworth, M.E. (1979) *Rate Processes of Extractive Metallurgy*, Plenum Press, New York.

Šontevska, V., Jovanovski, G., Makreski, P., Raškovska, A. and Šoptrajanov, B. (2008) "Minerals from Macedonia. XXI. Vibrational spectroscopy as identificational tool for some phyllosilicate minerals" *Acta Chimica Slovenica*, 55 (4), 757–766.

Stuart, B.H. (2004) *Infrared Spectroscopy: Fundamentals and Applications*, John Wiley & Sons, Ltd. (Analytical techniques in the sciences), Chichester, England.

Stubičan, V. and Roy, R. (1961) "Isomorphous substitution and infra-red spectra of the layer lattice silicates" *The American Mineralogist*, 46 (1-2), 32–51.

Taylor, A.S., Blum, J.D., Lasaga, A.C. and MacInnis, I.N. (2000) "Kinetics of dissolution and Sr release during biotite and phlogopite weathering" *Geochimica et Cosmochimica Acta*, 64 (7), 1191–1208.

Temuujin, J., Jadambaa, Ts., Burmaa, G., Erdenechimeg, Sh., Amarsanaa, J. and MacKenzie, K.J.D. (2004) "Characterisation of acid activated montmorillonite clay from Tuulant (Mongolia)" *Ceramics International*, 30 (2), 251–255.

Temuujin, J., Okada, K. and MacKenzie, K.J.D. (2003) "Preparation of porous silica from vermiculite by selective leaching" *Applied Clay Science*, 22 (4), 187–195.

Thommes, M., Kaneko, K., Neimark, A.V., Olivier, J.P., Rodriguez-Reinoso, F., Rouquerol, J. and Sing, K.S.W. (2015) "Physisorption of gases, with special reference to the evaluation of surface area and pore size distribution (IUPAC Technical Report)" *Pure and Applied Chemistry*, 87 (9-10), 1051–1069.

Tiwari, M.K., Bajpai, S., Dewangan, U.K. and Tamrakar, R.K. (2015) "Suitability of leaching test methods for fly ash and slag: A review" *Journal of Radiation Research and Applied Sciences*, 8 (4), 523–537.

Treybal, R.E. (1980) "Leaching", in: *Mass-Transfer Operations, Chemical Engineering*, McGraw-Hill, Singapore, pp. 717–765.

Tuller, M., Or, D. and Dudley, L.M. (1999) "Adsorption and capillary condensation in porous media: Liquid retention and interfacial configurations in angular pores" *Water Resources Research*, 35 (7), 1949–1964.

Üçgül, E. and Girgin, İ. (2002) "Chemical exfoliation characteristics of Karakoç phlogopite in hydrogen peroxide solution" *Turkish Journal of Chemistry*, 26 (3), 431–440.

Udupa, A.R., Kawatra, S.K. and Prasad, M.S. (1990) "Developments in gold leaching: A literature survey" *Mineral Processing and Extractive Metallurgy Review*, 7 (2), 115–135.

Van Arsdale, G.D. (1953) *Hydrometallurgy of Base Metals*, 1st ed. McGraw-Hill, New York.

van Straaten, P. (2002) *Rocks for Crops: Agrominerals of sub-Saharan Africa*, ICRAF, Nairobi, Kenya.

Vedder, W. (1964) "Correlations between infrared spectrum and chemical composition of mica" *The American Mineralogist*, 49 (5-6), 33.

Venter, I. (2015) "Mesoporous Silica Recovery from Phlogopite by Aqua Regia Leaching" University of Pretoria, Pretoria.

Verbeek, C.J.R. (2002) "Highly filled polyethylene/phlogopite composites" *Materials Letters*, 52 (6), 453–457.

von Reichenbach, H.G. (1969) "Potassium release from muscovite as influenced by particle size" *Clays and Clay Minerals*, 17 (1), 23–29.

Wang, R., Sang, S., Zhu, D., Liu, S. and Yu, K. (2018) "Pore characteristics and controlling factors of the Lower Cambrian Hetang Formation shale in Northeast Jiangxi, China" *Energy Exploration & Exploitation*, 36 (1), 43–65.

Wang, Z., Jiang, X., Pan, M. and Shi, Y. (2020) "Nano-scale pore structure and its multi-fractal characteristics of tight sandstone by N2 adsorption/desorption analyses: A case study of Shihezi Formation from the Sulige Gas Filed, Ordos Basin, China" *Minerals*, 10 (4), 377.

Wen, L., Liang, W., Zhang, Z. and Huang, J. (1988) *The Infrared Spectroscopy of Minerals*, Chongqing University Press.

Whittington, B.I. and Muir, D. (2000) "Pressure acid leaching of nickel laterites: a review" *Mineral Processing and Extractive Metallurgy Review*, 21 (6), 527–599.

Woest, G.S. (2016) "Selective Leaching of Phlogopite", Department of Chemical Engineering, University of Pretoria, Pretoria.

Woollacott, L.C. and Eric, R.H. (1994) "Mineral and metal extraction: an overview" South African Institute of Mining and Metallurgy, Johannesburg.

Wright, B. and Stone, M. (1999) “Quality Control Plots for Evaluating Co-Relations”, in: *Measurement Essentials,* Wide Range, Wilmington, Delaware, pp. 183–189.

Wu, C., Wang, P., Yao, X., Liu, C., Chen, D., Lu, G.Q. and Cheng, H. (2005) “Effects of SWNT and metallic catalyst on hydrogen absorption/desorption performance of MgH_2” *The Journal of Physical Chemistry B*, 109 (47), 22217–22221.

Wypych, F., Adad, L.B., Mattoso, N., Marangon, A.a.S. and Schreiner, W.H. (2005) "Synthesis and characterization of disordered layered silica obtained by selective leaching of octahedral sheets from chrysotile and phlogopite structures" *Journal of Colloid and Interface Science*, 283 (1), 107–112.

Xue, B., Zhang, J., Tang, X., Yang, C., Chen, Q., Man, X. and Dang, W. (2016) "Micro-pore structure and gas accumulation characteristics of shale in the Longmaxi Formation, Northwest Guizhou" *Petroleum Research*, 1 (2), 191–204.

Yoshida, T. (2003) "Leaching of zinc oxide in acidic solution" *Materials Transactions*, 44 (12), 2489–2493.

Yuan, Y. and Rezaee, R. (2019) "Comparative porosity and pore structure assessment in Shales: Measurement techniques, influencing factors and implications for reservoir characterization" *Energies*, 12 (11), 2094.

Zeller, M.V. and Juszli, M.P. (1975) *Infrared comparison spectra from Minerals, Applied Infrared Spectroscopy* (German). Bodenseewerk Perkin-Elmer & Co GmbH, Überlingen.

Zeng, Y., Prasetyo, L., Tan, S.J., Fan, C., Do, D.D. and Nicholson, D. (2017) "On the hysteresis of adsorption and desorption of simple gases in open end and closed end pores" *Chemical Engineering Science*, 158, 462–479.

Appendix A

α_G data plotted in Figure 17 and Figure 18.

Table 10: α_G data over time for varying initial acid concentrations and temperatures.

Time	$[H^+]_0$ = 2 M			$[H^+]_0$ = 3 M			$[H^+]_0$ = 4 M		
(min)	35 °C	50 °C	65 °C	35 °C	50 °C	65 °C	35 °C	50 °C	65 °C
0	0.00	0.00	0.00	0.00	0.00	0.00	0.00	0.00	0.00
30	0.04	0.08	0.17	0.05	0.12	0.30	0.06	0.16	0.30
60	0.06	0.13	0.32	0.08	0.17	0.48	0.09	0.22	0.57
90	0.08	0.14	0.40	0.10	0.24	0.60	0.13	0.27	0.76
120	0.09	0.16	0.48	0.13	0.28	0.72	0.15	0.32	0.85
240	0.13	0.24	0.72	0.18	0.44	0.94	0.21	0.50	0.96
360	0.15	0.35	0.81	0.23	0.55	1.00	0.26	0.60	1.00

Appendix B

g(α) versus time data for overall conversion

Table 11: g(α) values calculated using α_G data for each reaction model with reaction rate constants and regression indicated.

Time (min)	$[H^+]_0$ (M)	Temp (°C)	g_{P2}	g_{P3}	g_{P4}	g_{A2}	g_{A3}	g_{A4}	g_{R2}	g_{R3}	g_{D1}	g_{D2}	g_{D3}	g_{D4}	g_{F0}	g_{F1}	g_{F2}	g_{F3}
0	2.00	35	0.00	0.00	0.00	0.00	0.00	0.00	0.00	0.00	0.00	0.00	0.00	0.00	0.00	0.00	0.00	0.00
30	2.00	35	2.09E-01	3.53E-01	4.58E-01	2.12E-01	3.55E-01	4.60E-01	2.22E-02	1.48E-02	1.92E-03	9.74E-04	2.20E-04	2.18E-04	4.38E-02	4.48E-02	4.58E-02	4.69E-02
60	2.00	35	2.50E-01	3.97E-01	5.00E-01	2.54E-01	4.01E-01	5.04E-01	3.17E-02	2.13E-02	3.90E-03	1.99E-03	4.52E-04	4.46E-04	6.24E-02	6.45E-02	6.66E-02	6.88E-02
90	2.00	35	2.80E-01	4.28E-01	5.29E-01	2.86E-01	4.34E-01	5.34E-01	4.00E-02	2.68E-02	6.13E-03	3.15E-03	7.19E-04	7.06E-04	7.83E-02	8.15E-02	8.50E-02	8.86E-02
120	2.00	35	3.03E-01	4.51E-01	5.50E-01	3.10E-01	4.58E-01	5.57E-01	4.70E-02	3.16E-02	8.42E-03	4.35E-03	9.97E-04	9.76E-04	9.18E-02	9.63E-02	1.01E-01	1.06E-01
240	2.00	35	3.60E-01	5.06E-01	6.00E-01	3.73E-01	5.18E-01	6.11E-01	6.71E-02	4.53E-02	1.68E-02	8.80E-03	2.05E-03	1.99E-03	1.30E-01	1.39E-01	1.49E-01	1.60E-01
360	2.00	35	3.86E-01	5.30E-01	6.21E-01	4.01E-01	5.44E-01	6.33E-01	7.74E-02	5.23E-02	2.21E-02	1.17E-02	2.73E-03	2.64E-03	1.49E-01	1.61E-01	1.75E-01	1.90E-01
	slope (k)		1.20E-03	1.57E-03	1.78E-03	1.25E-03	1.61E-03	1.82E-03	2.55E-04	1.72E-04	7.07E-05	3.70E-05	8.62E-06	8.36E-06	4.92E-04	5.31E-04	5.73E-04	6.20E-04
	R^2		0.66	0.54	0.47	0.67	0.55	0.48	0.90	0.91	1.00	1.00	1.00	1.00	0.90	0.91	0.92	0.94
0	2.00	50	0.00	0.00	0.00	0.00	0.00	0.00	0.00	0.00	0.00	0.00	0.00	0.00	0.00	0.00	0.00	0.00
30	2.00	50	2.89E-01	4.37E-01	5.37E-01	2.95E-01	4.43E-01	5.43E-01	4.25E-02	2.86E-02	6.94E-03	3.57E-03	8.16E-04	8.01E-04	8.33E-02	8.70E-02	9.08E-02	9.50E-02
60	2.00	50	3.54E-01	5.00E-01	5.95E-01	3.66E-01	5.12E-01	6.05E-01	6.48E-02	4.36E-02	1.57E-02	8.20E-03	1.91E-03	1.85E-03	1.25E-01	1.34E-01	1.43E-01	1.54E-01
90	2.00	50	3.77E-01	5.22E-01	6.14E-01	3.92E-01	5.35E-01	6.26E-01	7.39E-02	4.99E-02	2.02E-02	1.06E-02	2.49E-03	2.40E-03	1.42E-01	1.53E-01	1.66E-01	1.80E-01
120	2.00	50	3.97E-01	5.40E-01	6.30E-01	4.14E-01	5.55E-01	6.43E-01	8.21E-02	5.55E-02	2.48E-02	1.31E-02	3.08E-03	2.97E-03	1.57E-01	1.71E-01	1.87E-01	2.04E-01
240	2.00	50	4.84E-01	6.17E-01	6.96E-01	5.17E-01	6.44E-01	7.19E-01	1.25E-01	8.53E-02	5.51E-02	3.00E-02	7.28E-03	6.86E-03	2.35E-01	2.68E-01	3.07E-01	3.54E-01
360	2.00	50	5.95E-01	7.08E-01	7.71E-01	6.61E-01	7.59E-01	8.13E-01	1.96E-01	1.36E-01	1.26E-01	7.18E-02	1.84E-02	1.67E-02	3.54E-01	4.37E-01	5.49E-01	6.99E-01
	slope (k)		1.57E-03	1.88E-03	2.03E-03	1.70E-03	1.98E-03	2.12E-03	4.65E-04	3.18E-04	2.26E-04	1.23E-04	2.99E-05	2.82E-05	8.66E-04	1.00E-03	1.16E-03	1.36E-03
	R^2		0.63	0.52	0.45	0.66	0.54	0.47	0.89	0.90	0.99	0.99	0.99	0.99	0.88	0.91	0.93	0.95
0	2.00	65	0.00	0.00	0.00	0.00	0.00	0.00	0.00	0.00	0.00	0.00	0.00	0.00	0.00	0.00	0.00	0.00
30	2.00	65	4.08E-01	5.50E-01	6.39E-01	4.27E-01	5.67E-01	6.53E-01	8.69E-02	5.88E-02	2.77E-02	1.47E-02	3.46E-03	3.33E-03	1.66E-01	1.82E-01	2.00E-01	2.19E-01
60	2.00	65	5.63E-01	6.82E-01	7.50E-01	6.17E-01	7.25E-01	7.86E-01	1.73E-01	1.19E-01	1.00E-01	5.65E-02	1.42E-02	1.31E-02	3.17E-01	3.81E-01	4.64E-01	5.71E-01
90	2.00	65	6.31E-01	7.36E-01	7.94E-01	7.13E-01	7.98E-01	8.44E-01	2.24E-01	1.56E-01	1.59E-01	9.26E-02	2.43E-02	2.17E-02	3.98E-01	5.08E-01	6.62E-01	8.81E-01
120	2.00	65	6.93E-01	7.83E-01	8.32E-01	8.08E-01	8.68E-01	8.99E-01	2.79E-01	1.96E-01	2.30E-01	1.40E-01	3.83E-02	3.33E-02	4.80E-01	6.53E-01	9.22E-01	1.35E+00
240	2.00	65	8.47E-01	8.95E-01	9.20E-01	1.12E+00	1.08E+00	1.06E+00	4.69E-01	3.44E-01	5.15E-01	3.61E-01	1.18E-01	9.13E-02	7.18E-01	1.27E+00	2.55E+00	5.78E+00
360	2.00	65	8.98E-01	9.31E-01	9.48E-01	1.28E+00	1.18E+00	1.13E+00	5.60E-01	4.21E-01	6.50E-01	4.88E-01	1.77E-01	1.28E-01	8.06E-01	1.64E+00	4.15E+00	1.28E+01
	slope (k)		2.96E-03	2.90E-03	2.84E-03	4.14E-03	3.68E-03	3.43E-03	1.90E-03	1.40E-03	2.21E-03	1.55E-03	5.08E-04	3.92E-04	2.85E-03	5.20E-03	1.07E-02	2.44E-02
	R^2		0.73	0.60	0.52	0.85	0.71	0.61	0.98	0.99	0.99	0.98	0.96	0.97	0.94	1.00	0.97	0.91

(Table 11 continued)

Time (min)	$[H^+]_0$ (M)	Temp (°C)	g_{P2}	g_{P3}	g_{P4}	g_{A2}	g_{A3}	g_{A4}	g_{R2}	g_{R3}	g_{D1}	g_{D2}	g_{D3}	g_{D4}	g_{F0}	g_{F1}	g_{F2}	g_{F3}
0	3.00	35	0.00	0.00	0.00	0.00	0.00	0.00	0.00	0.00	0.00	0.00	0.00	0.00	0.00	0.00	0.00	0.00
30	3.00	35	2.25E-01	3.70E-01	4.74E-01	2.28E-01	3.73E-01	4.78E-01	2.57E-02	1.72E-02	2.57E-03	1.31E-03	2.96E-04	2.92E-04	5.07E-02	5.20E-02	5.34E-02	5.48E-02
60	3.00	35	2.77E-01	4.25E-01	5.26E-01	2.83E-01	4.31E-01	5.32E-01	3.92E-02	2.63E-02	5.90E-03	3.03E-03	6.91E-04	6.79E-04	7.68E-02	7.99E-02	8.32E-02	8.66E-02
90	3.00	35	3.23E-01	4.71E-01	5.68E-01	3.32E-01	4.79E-01	5.76E-01	5.35E-02	3.60E-02	1.09E-02	5.63E-03	1.30E-03	1.27E-03	1.04E-01	1.10E-01	1.16E-01	1.23E-01
120	3.00	35	3.65E-01	5.11E-01	6.04E-01	3.78E-01	5.23E-01	6.15E-01	6.90E-02	4.66E-02	1.78E-02	9.31E-03	2.17E-03	2.10E-03	1.33E-01	1.43E-01	1.54E-01	1.66E-01
240	3.00	35	4.26E-01	5.66E-01	6.53E-01	4.47E-01	5.85E-01	6.69E-01	9.53E-02	6.46E-02	3.29E-02	1.76E-02	4.17E-03	3.99E-03	1.81E-01	2.00E-01	2.22E-01	2.46E-01
360	3.00	35	4.66E-01	6.01E-01	6.83E-01	4.95E-01	6.26E-01	7.04E-01	1.15E-01	7.84E-02	4.72E-02	2.55E-02	6.15E-03	5.83E-03	2.17E-01	2.45E-01	2.78E-01	3.16E-01
	slope (k)		1.47E-03	1.81E-03	1.99E-03	1.56E-03	1.89E-03	2.06E-03	3.79E-04	2.57E-04	1.43E-04	7.62E-05	1.81E-05	1.73E-05	7.19E-04	8.00E-04	8.93E-04	1.00E-03
	R^2		0.70	0.58	0.50	0.72	0.59	0.52	0.93	0.93	0.99	0.99	0.99	0.99	0.92	0.93	0.95	0.96
0	3.00	50	0.00	0.00	0.00	0.00	0.00	0.00	0.00	0.00	0.00	0.00	0.00	0.00	0.00	0.00	0.00	0.00
30	3.00	50	3.46E-01	4.93E-01	5.88E-01	3.57E-01	5.04E-01	5.98E-01	6.18E-02	4.17E-02	1.44E-02	7.49E-03	1.74E-03	1.69E-03	1.20E-01	1.28E-01	1.36E-01	1.45E-01
60	3.00	50	4.17E-01	5.58E-01	6.46E-01	4.37E-01	5.76E-01	6.61E-01	9.12E-02	6.17E-02	3.03E-02	1.61E-02	3.81E-03	3.65E-03	1.74E-01	1.91E-01	2.11E-01	2.33E-01
90	3.00	50	4.85E-01	6.17E-01	6.96E-01	5.17E-01	6.44E-01	7.19E-01	1.25E-01	8.53E-02	5.51E-02	3.00E-02	7.28E-03	6.87E-03	2.35E-01	2.68E-01	3.07E-01	3.54E-01
120	3.00	50	5.27E-01	6.52E-01	7.26E-01	5.70E-01	6.88E-01	7.55E-01	1.50E-01	1.03E-01	7.71E-02	4.27E-02	1.06E-02	9.83E-03	2.78E-01	3.25E-01	3.84E-01	4.58E-01
240	3.00	50	6.60E-01	7.58E-01	8.12E-01	7.56E-01	8.30E-01	8.70E-01	2.49E-01	1.74E-01	1.90E-01	1.13E-01	3.01E-02	2.67E-02	4.36E-01	5.72E-01	7.72E-01	1.07E+00
360	3.00	50	7.40E-01	8.18E-01	8.60E-01	8.90E-01	9.25E-01	9.43E-01	3.27E-01	2.32E-01	2.99E-01	1.88E-01	5.38E-02	4.55E-02	5.47E-01	7.92E-01	1.21E+00	1.94E+00
	slope (k)		2.26E-03	2.42E-03	2.47E-03	2.67E-03	2.71E-03	2.71E-03	9.83E-04	6.88E-04	8.06E-04	4.80E-04	1.28E-04	1.13E-04	1.70E-03	2.28E-03	3.13E-03	4.40E-03
	R^2		0.73	0.59	0.51	0.79	0.64	0.56	0.97	0.98	0.99	0.98	0.97	0.97	0.95	0.98	1.00	0.99
0	3.00	65	0.00	0.00	0.00	0.00	0.00	0.00	0.00	0.00	0.00	0.00	0.00	0.00	0.00	0.00	0.00	0.00
30	3.00	65	5.49E-01	6.71E-01	7.41E-01	5.99E-01	7.11E-01	7.74E-01	1.64E-01	1.13E-01	9.10E-02	5.09E-02	1.27E-02	1.18E-02	3.02E-01	3.59E-01	4.32E-01	5.25E-01
60	3.00	65	6.92E-01	7.82E-01	8.32E-01	8.07E-01	8.67E-01	8.98E-01	2.78E-01	1.95E-01	2.29E-01	1.39E-01	3.81E-02	3.32E-02	4.79E-01	6.52E-01	9.19E-01	1.34E+00
90	3.00	65	7.77E-01	8.45E-01	8.82E-01	9.63E-01	9.75E-01	9.81E-01	3.71E-01	2.66E-01	3.65E-01	2.37E-01	7.07E-02	5.81E-02	6.04E-01	9.27E-01	1.53E+00	2.69E+00
120	3.00	65	8.46E-01	8.95E-01	9.20E-01	1.12E+00	1.08E+00	1.06E+00	4.67E-01	3.43E-01	5.12E-01	3.58E-01	1.17E-01	9.05E-02	7.16E-01	1.26E+00	2.52E+00	5.69E+00
240	3.00	65	9.71E-01	9.80E-01	9.85E-01	1.69E+00	1.42E+00	1.30E+00	7.59E-01	6.13E-01	8.87E-01	7.77E-01	3.75E-01	2.22E-01	9.42E-01	2.85E+00	1.62E+01	1.48E+02
360	3.00	65	1.00E+00	1.00E+00	1.00E+00	3.00E+00	2.10E+00	3.74E+00	9.90E-01	9.54E-01	1.00E+00	9.99E-01	9.09E-01	3.31E-01	1.00E+00	9.21E+00	1.00E+04	5.00E+07
	slope (k)		3.26E-03	3.06E-03	2.94E-03	6.29E-03	4.90E-03	4.26E-03	3.05E-03	2.49E-03	3.78E-03	3.33E-03	1.69E+00	9.53E-04	3.62E-03	1.18E-02	6.81E-02	6.17E-01
	R^2		0.65	0.53	0.47	0.91	0.76	0.66	0.97	0.99	0.99	0.99	0.95	0.98	0.87	0.99	0.86	0.78

(Table 11 continued)

Time (min)	$[H^+]_0$ (M)	Temp (°C)	g_{P2}	g_{P3}	g_{P4}	g_{A2}	g_{A3}	g_{A4}	g_{R2}	g_{R3}	g_{D1}	g_{D2}	g_{D3}	g_{D4}	g_{F0}	g_{F1}	g_{F2}	g_{F3}
0	4.00	35	0.00	0.00	0.00	0.00	0.00	0.00	0.00	0.00	0.00	0.00	0.00	0.00	0.00	0.00	0.00	0.00
30	4.00	35	2.45E-01	3.91E-01	4.95E-01	2.49E-01	3.95E-01	4.99E-01	3.05E-02	2.04E-02	3.60E-03	1.84E-03	4.16E-04	4.11E-04	6.00E-02	6.19E-02	6.38E-02	6.58E-02
60	4.00	35	3.04E-01	4.53E-01	5.52E-01	3.12E-01	4.60E-01	5.58E-01	4.75E-02	3.19E-02	8.59E-03	4.43E-03	1.02E-03	9.96E-04	9.27E-02	9.72E-02	1.02E-01	1.07E-01
90	4.00	35	3.55E-01	5.02E-01	5.96E-01	3.67E-01	5.13E-01	6.06E-01	6.53E-02	4.40E-02	1.60E-02	8.34E-03	1.94E-03	1.88E-03	1.26E-01	1.35E-01	1.45E-01	1.55E-01
120	4.00	35	3.82E-01	5.27E-01	6.18E-01	3.98E-01	5.41E-01	6.31E-01	7.60E-02	5.13E-02	2.14E-02	1.12E-02	2.63E-03	2.54E-03	1.46E-01	1.58E-01	1.71E-01	1.86E-01
240	4.00	35	4.57E-01	5.93E-01	6.76E-01	4.83E-01	6.16E-01	6.95E-01	1.10E-01	7.49E-02	4.34E-02	2.34E-02	5.62E-03	5.34E-03	2.08E-01	2.34E-01	2.63E-01	2.98E-01
360	4.00	35	5.09E-01	6.38E-01	7.14E-01	5.48E-01	6.69E-01	7.40E-01	1.39E-01	9.52E-02	6.72E-02	3.69E-02	9.06E-03	8.48E-03	2.59E-01	3.00E-01	3.50E-01	4.11E-01
	slope (k)		1.56E-03	1.88E-03	2.05E-03	1.67E-03	1.97E-03	2.13E-03	4.33E-04	2.94E-04	1.86E-04	1.00E-04	2.41E-05	2.28E-05	8.13E-04	9.21E-04	1.05E-03	1.20E-03
	R^2		0.69	0.56	0.49	0.72	0.58	0.51	0.92	0.93	1.00	1.00	1.00	1.00	0.91	0.93	0.95	0.97
0	4.00	50	0.00	0.00	0.00	0.00	0.00	0.00	0.00	0.00	0.00	0.00	0.00	0.00	0.00	0.00	0.00	0.00
30	4.00	50	4.01E-01	5.44E-01	6.33E-01	4.18E-01	5.59E-01	6.47E-01	8.38E-02	5.67E-02	2.58E-02	1.36E-02	3.21E-03	3.09E-03	1.61E-01	1.75E-01	1.91E-01	2.10E-01
60	4.00	50	4.66E-01	6.01E-01	6.82E-01	4.94E-01	6.25E-01	7.03E-01	1.15E-01	7.82E-02	4.70E-02	2.54E-02	6.12E-03	5.80E-03	2.17E-01	2.44E-01	2.77E-01	3.15E-01
90	4.00	50	5.18E-01	6.45E-01	7.20E-01	5.59E-01	6.78E-01	7.47E-01	1.45E-01	9.88E-02	7.19E-02	3.97E-02	9.77E-03	9.12E-03	2.68E-01	3.12E-01	3.66E-01	4.34E-01
120	4.00	50	5.63E-01	6.82E-01	7.50E-01	6.17E-01	7.25E-01	7.85E-01	1.73E-01	1.19E-01	1.00E-01	5.64E-02	1.42E-02	1.31E-02	3.17E-01	3.81E-01	4.63E-01	5.70E-01
240	4.00	50	7.08E-01	7.95E-01	8.42E-01	8.35E-01	8.87E-01	9.14E-01	2.94E-01	2.07E-01	2.52E-01	1.55E-01	4.30E-02	3.70E-02	5.02E-01	6.97E-01	1.01E+00	1.51E+00
360	4.00	50	7.77E-01	8.45E-01	8.81E-01	9.62E-01	9.74E-01	9.81E-01	3.70E-01	2.65E-01	3.64E-01	2.37E-01	7.04E-02	5.79E-02	6.03E-01	9.25E-01	1.52E+00	2.68E+00
	slope (k)		2.36E-03	2.47E-03	2.51E-03	2.88E-03	2.84E-03	2.80E-03	1.13E-03	8.03E-04	1.05E-03	6.48E-04	1.80E-04	1.55E-04	1.91E-03	2.73E-03	4.03E-03	6.18E-03
	R^2		0.70	0.56	0.49	0.78	0.63	0.54	0.96	0.97	0.98	0.97	0.96	0.97	0.94	0.98	0.99	0.98
0	4.00	65	0.00	0.00	0.00	0.00	0.00	0.00	0.00	0.00	0.00	0.00	0.00	0.00	0.00	0.00	0.00	0.00
30	4.00	65	5.52E-01	6.73E-01	7.43E-01	6.02E-01	7.13E-01	7.76E-01	1.66E-01	1.14E-01	9.25E-02	5.18E-02	1.30E-02	1.20E-02	3.04E-01	3.63E-01	4.37E-01	5.33E-01
60	4.00	65	7.55E-01	8.29E-01	8.69E-01	9.19E-01	9.46E-01	9.59E-01	3.45E-01	2.46E-01	3.26E-01	2.08E-01	6.03E-02	5.04E-02	5.71E-01	8.45E-01	1.33E+00	2.21E+00
90	4.00	65	8.69E-01	9.10E-01	9.32E-01	1.19E+00	1.12E+00	1.09E+00	5.05E-01	3.74E-01	5.70E-01	4.10E-01	1.40E-01	1.05E-01	7.55E-01	1.41E+00	3.08E+00	7.81E+00
120	4.00	65	9.22E-01	9.47E-01	9.60E-01	1.38E+00	1.24E+00	1.17E+00	6.13E-01	4.69E-01	7.23E-01	5.66E-01	2.20E-01	1.51E-01	8.50E-01	1.90E+00	5.67E+00	2.18E+01
240	4.00	65	9.80E-01	9.86E-01	9.90E-01	1.79E+00	1.48E+00	1.34E+00	8.00E-01	6.58E-01	9.21E-01	8.31E-01	4.33E-01	2.43E-01	9.60E-01	3.22E+00	2.39E+01	3.11E+02
360	4.00	65	1.00E+00	1.00E+00	1.00E+00	3.03E+00	2.10E+00	1.74E+00	9.90E-01	9.54E-01	1.00E+00	9.99E-01	9.09E-01	3.31E-01	1.00E+00	9.21E+00	1.00E+04	5.00E+07
	slope (k)		3.30E-03	3.09E-03	2.96E-03	6.85E-03	5.21E-03	4.47E-03	3.28E-03	2.74E-03	4.02E-03	3.67E-03	1.91E-03	1.08E-03	3.73E-03	1.37E-02	3.73E-03	1.37E-02
	R^2		0.59	0.50	0.44	0.86	0.73	0.63	0.89	0.93	0.89	0.95	0.98	0.97	0.76	0.99	0.91	0.80

Appendix C

Arrhenius plot data with associated kinetic triplets

Table 12: Arrhenius plot data with k_0, Ea and R^2 values indicated for the diffusion models.

	lnk			
	g_{D1}	g_{D2}	g_{D3}	g_{D4}
1/T	$[H^+]_0$ = 2M			
0.00325	-9.56	-10.20	-11.66	-11.69
0.00309	-8.40	-9.00	-10.42	-10.48
0.00296	-6.11	-6.47	-7.59	-7.85
k_0	3.30E+12	4.20E+13	4.30E+14	3.30E+13
Ea (kJ/mol)	98.83	107.15	116.90	110.38
R^2	0.96	0.95	0.94	0.95
1/T	$[H^+]_0$ = 3M			
0.00325	-8.85	-9.48	-10.92	-10.96
0.00309	-7.12	-7.64	-8.96	-9.08
0.00296	-5.58	-5.70	-6.43	-6.96
k_0	1.60E+12	2.20E+14	1.30E+17	6.30E+14
Ea (kJ/mol)	94.63	108.98	129.23	115.56
R^2	1.00	1.00	0.99	1.00
1/T	$[H^+]_0$ = 4M			
0.00325	-8.59	-9.21	-10.64	-10.69
0.00309	-6.86	-7.34	-8.62	-8.77
0.00296	-5.52	-5.61	-6.26	-6.83
k_0	2.30E+11	4.30E+13	5.30E+16	1.50E+14
Ea (kJ/mol)	88.89	104.02	126.14	111.16
R^2	1.00	1.00	0.99	1.00

Appendix D

Python code for comparing analytical conversion data to experimental data for model D1

Imports

In [1]:
```
from numpy import array, log, append, exp, linspace, asarray, interp
from scipy.integrate import odeint
import pandas as pd
import matplotlib
from matplotlib import pyplot as plt
%matplotlib inline
```

Data

In [2]:
```
#importing kinetic triplet raw data from excel

Raw_data = pd.read_excel (r'C:\Users\Cheri\Desktop\Varsity\Post grad\Masters\Code\Final Codes\Final\Reformatting.xlsx', shee
Raw_data.head(9) #displays the data
```

Out[2]:

	H0	k	T
0	2	0.000071	308.15
1	2	0.000226	323.15
2	2	0.002210	338.15
3	3	0.000143	308.15
4	3	0.000806	323.15
5	3	0.003781	338.15
6	4	0.000186	308.15
7	4	0.001051	323.15
8	4	0.004016	338.15

In [3]:
```
#assigning values to imported raw data
H0_vals  = Raw_data.values[:,0]
k_vals   = Raw_data.values[:,1]
T_vals   = Raw_data.values[:,2]
```

Model Fitting

In [4]:
```
#creating empty lists (which are later filled with t and a values for each model, respectively)
tspan_vals = []
aD1vals    = []

for k in k_vals:                        #for each rate constant the imported list
    def func1(var, t):                  #I define a function that takes in variables and time

        aD1 = var                       #defining the variables
        fD1 = 1/(2*aD1)                 #the differential form of model D1
        daD1dt = k*fD1                  #Arrhenius equation with differential rate equation

        return daD1dt                   #this function returns the differential (conversion over time) forms of model D1

    tspan = linspace(0, 360, 1000)      #timespan of integration with number of samples to generate

    #initial a value is 0. Using an initial ao = 0 would result in division of 0 and thus undefined
    #numbers which generate integration errors
    ao = [0.0001]                       #initial a for t = 0
    ai = odeint(func1, ao, tspan)       #integration using the 'odeint' function

    #model D1 is assigned it's values from integration
    aD1 = ai[:,0]

    #here, the time and conversion values are appended into the empty lists above
    tspan_vals.append(tspan)
    aD1vals.append(aD1)
```

α data

In [7]:
```
import pandas
print ('')
print ('Predicted values for α:')

heading = ["2-35", "2-50", "2-65", "3-35", "3-50", "3-65", "4-35", "4-50", "4-65"]
time    = ["0", "30", "60", "90", "120", "240", "360"]

data = array([[interp(0   , tspan_vals[0], aD1vals[0]), interp(0   , tspan_vals[1], aD1vals[1]), interp(0   , tspan_vals[2], aD
              [interp(30  , tspan_vals[0], aD1vals[0]), interp(30  , tspan_vals[1], aD1vals[1]), interp(30  , tspan_vals[2], aD
              [interp(60  , tspan_vals[0], aD1vals[0]), interp(60  , tspan_vals[1], aD1vals[1]), interp(60  , tspan_vals[2], aD
              [interp(90  , tspan_vals[0], aD1vals[0]), interp(90  , tspan_vals[1], aD1vals[1]), interp(90  , tspan_vals[2], aD
              [interp(120, tspan_vals[0], aD1vals[0]), interp(120, tspan_vals[1], aD1vals[1]), interp(120, tspan_vals[2], aD
              [interp(240, tspan_vals[0], aD1vals[0]), interp(240, tspan_vals[1], aD1vals[1]), interp(240, tspan_vals[2], aD
              [interp(360, tspan_vals[0], aD1vals[0]), interp(360, tspan_vals[1], aD1vals[1]), interp(360, tspan_vals[2], aD
display (pandas.DataFrame(data, time, heading))
```

Predicted values for α:

	2-35	2-50	2-65	3-35	3-50	3-65	4-35	4-50	4-65
0	0.000100	0.000100	0.000100	0.000100	0.000100	0.000100	0.000100	0.000100	0.000100
30	0.046052	0.082264	0.257461	0.065445	0.155488	0.336777	0.074626	0.177541	0.347104
60	0.065127	0.116339	0.364106	0.092553	0.219694	0.476275	0.105537	0.251082	0.490881
90	0.079764	0.142486	0.445937	0.113354	0.269314	0.583316	0.129256	0.307511	0.601204
120	0.092104	0.164528	0.514924	0.130890	0.310977	0.673555	0.149252	0.355063	0.694211
240	0.130255	0.232678	0.728213	0.185107	0.439788	0.952551	0.211074	0.502164	0.981762
360	0.159529	0.284971	0.891675	0.226709	0.538628	1.166632	0.258512	0.615022	1.202408

In [8]:

```
import pandas
print ('')
print ('Predicted values for α (2M):')
heading2, heading3, heading4 = ["2-65"], ["3-65"], ["4-65"]
time2, time3, time4    = ["12", "22", "40", "120", "150", "200"], ["15", "33", "70", "100", "230"], ["8", "20", "60", "95",
data2M_Extra = array([[interp(12  , tspan_vals[2], aD1vals[2])],
                      [interp(22 , tspan_vals[2], aD1vals[2])],
                      [interp(40 , tspan_vals[2], aD1vals[2])],
                      [interp(120 , tspan_vals[2], aD1vals[2])],
                      [interp(150, tspan_vals[2], aD1vals[2])],
                      [interp(200, tspan_vals[2], aD1vals[2])]])
display (pandas.DataFrame(data2M_Extra, time2, heading2))

print ('Predicted values for α (3M):')
data3M_Extra = array([[interp(15  , tspan_vals[2], aD1vals[2])],
                      [interp(33 , tspan_vals[2], aD1vals[2])],
                      [interp(70 , tspan_vals[2], aD1vals[2])],
                      [interp(100 , tspan_vals[2], aD1vals[2])],
                      [interp(230, tspan_vals[2], aD1vals[2])]])
display (pandas.DataFrame(data3M_Extra, time3, heading3))

print ('Predicted values for α (4M):')
data4M_Extra = array([[interp(8  , tspan_vals[2], aD1vals[2])],
                      [interp(20 , tspan_vals[2], aD1vals[2])],
                      [interp(60 , tspan_vals[2], aD1vals[2])],
                      [interp(95 , tspan_vals[2], aD1vals[2])],
                      [interp(130, tspan_vals[2], aD1vals[2])],
                      [interp(150, tspan_vals[2], aD1vals[2])]])
display (pandas.DataFrame(data4M_Extra, time4, heading4))
```

Predicted values for α (2M):

	2-65
12	0.162829
22	0.220477
40	0.297292
120	0.514924
150	0.575702
200	0.664764

Predicted values for α (3M):

	3-65
15	0.182050
33	0.270027
70	0.393279
100	0.470059
230	0.712880

Predicted values for α (4M):

	4-65
8	0.132947
20	0.210215
60	0.364106
95	0.458157
130	0.535950
150	0.575702

Appendix E

Conversion-time plots comparing all reaction models to experimental data.

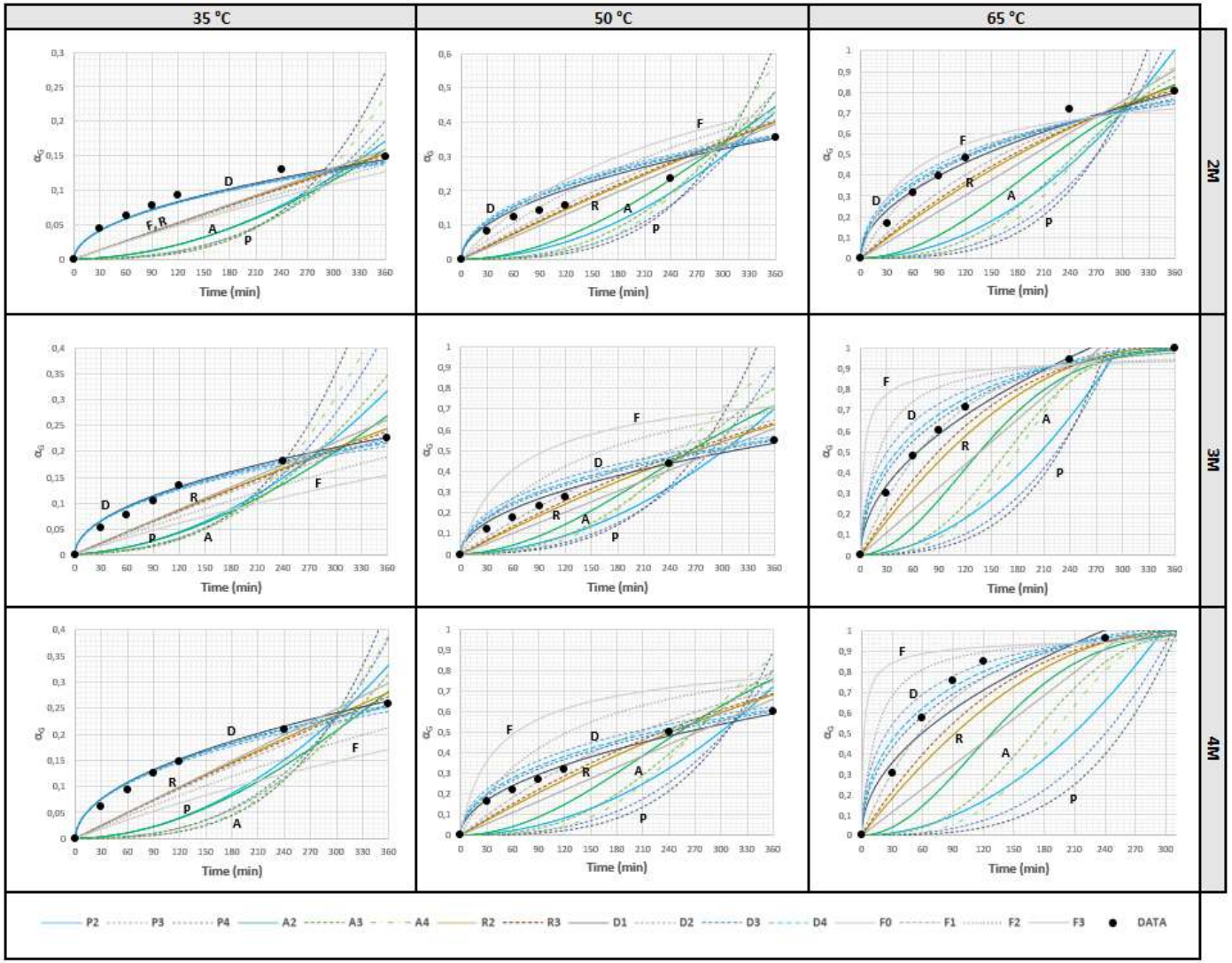

Appendix F

Testing data for Figure 21 and Figure 22.

Table 13: Conversion data for model testing (T = 65 °C).

t	$[H^+]_0$	α	t	$[H^+]_0$	α	t	$[H^+]_0$	α
12	2.00	0.14	15	3.00	0.19	8	4.00	0.18
22	2.00	0.17	33	3.00	0.22	20	4.00	0.21
40	2.00	0.17	70	3.00	0.33	60	4.00	0.40
120	2.00	0.46	100	3.00	0.52	95	4.00	0.64
150	2.00	0.56	230	3.00	0.87	130	4.00	0.84
200	2.00	0.66				150	4.00	0.94

Table 14: Conversion data for model testing at different concentrations.

		α for $[H^+]_0$ =	
	Time	2.4 M	2.6 M
35 °C	0	0.00	0.00
	30	0.05	0.06
	60	0.07	0.08
	90	0.10	0.10
	120	0.13	0.13
	240	0.17	0.17
	360	0.20	0.22
50 °C	0	0.00	0.00
	30	0.09	0.09
	60	0.17	0.18
	90	0.18	0.25
	120	0.23	0.26
	240	0.35	0.42
	360	0.50	0.53
65 °C	0	0.00	0.00
	30	0.26	0.27
	60	0.35	0.35
	90	0.39	0.48
	120	0.48	0.54
	240	0.77	0.82
	360	0.88	0.91

Appendix G

Python code for testing leaching model with additional "testing" experimental data

Imports

In [1]:
```
from numpy import array, append, exp, linspace, asarray, interp, ndarray
from scipy.integrate import odeint
from scipy.stats import linregress
import matplotlib
import pandas as pd
from matplotlib import pyplot as plt
%matplotlib inline
```

Raw Data

In [2]:
```
#importing raw α, T and [H+]0 data from excel (ALL temperatures)

Raw_data = pd.read_excel (r'C:\Users\Cheri\Desktop\Varsity\Post grad\Masters\Code\Data\Final Data Points.xlsx', sheet_name='
Raw_data.head(125) #displays the data
```

Out[2]:

	Time	Conc	α	Temp
0	0	2.0	0.000000	308.15
1	30	2.0	0.044000	308.15
2	60	2.0	0.082000	308.15
3	90	2.0	0.078000	308.15
4	120	2.0	0.092000	308.15
5	240	2.0	0.130000	308.15
6	360	2.0	0.149000	308.15
7	0	2.0	0.000000	323.15
8	30	2.0	0.083000	323.15
9	60	2.0	0.125000	323.15
10	90	2.0	0.142000	323.15
11	120	2.0	0.157000	323.15

In [3]:
```
#assigning values to imported raw data
time   = Raw_data.values[:,0]
H0_vals = Raw_data.values[:,1]
a_vals = Raw_data.values[:,2]
T_vals = Raw_data.values[:,3]
```

Equation 7a

Here I define the Arrhenius equation 7a which incorporates equation 15 and equation 16. The reaction rate constant is returned.

In [4]:
```
#Arrhenius equation for OVERALL conversion
def Arrhenius(H_IN, T):
    R = 8.314 #J/mol.K
    ko =   exp(-1.3358*H_IN + 31.69)      # equation 15
    Ea = ( -4.9705*H_IN + 109.03)*1000    # equation 16
    k  = ko*exp(-Ea/(R*T))                # equation 7a
    return k
```

Conversion equation for Model D1

This equation calculates the gravimetric conversion (α) over a reactor (for the entire reaction time range)

In [5]:
```
def α_equation(t_range, k, α_INITIAL):              # this function requires the reactor time range, rate constant and init
                                                    # α into a reactor as inputs

    # this function is used to solve the differential form of the rate equation
    def α_to_integrate(α, t, k):
        def f(α):
            fa = 1/(2*α)                            # differential form of reaction rate equation for model D1 (Table 2)
            return fa
        dαdt = k*f(α)
        return dαdt

    # integrating over the entire time range
    αt_vals = odeint(α_to_integrate, α_INITIAL, t_range, args=(k,)) # this solves the differential equation for α(t) over th
                                                                    # reactor time range from α0 (into reactor) to α out of
                                                                    # reactor


    # here I ensure that α can not be > 1
    def α_corrected(αt_vals):
        αt = []                                     # all corrected α values will be appended to this empty list
        for i in αt_vals:                           # 'i' indexes each α value calculated (from the integration)
            if i > 1:
                αtcorrected = 1                     # if that α > 1, the code returns α = 1
            else:
                αtcorrected = i                     # otherwise α calculated can be used
            αt.append(αtcorrected)                  # the corrected values are appended into the empty list 'αt'
        return αt
    return α_corrected(αt_vals)                     # the final values for α OUT of a reactor are returned
```

Printed Values For plotting in Excel:

In [7]:
```
dict = {'t_2'    : tspan,
        'α_2_35' : α_model_2_35,
        'α_2_50' : α_model_2_50,
        'α_2_65' : α_model_2_65,
        't_24'   : tspan,
        'α_24_35' : α_model_24_35,
        'α_24_50' : α_model_24_50,
        'α_24_65' : α_model_24_65,
        't_26'   : tspan,
        'α_26_35' : α_model_26_35,
        'α_26_50' : α_model_26_50,
        'α_26_65' : α_model_26_65,
        't_3'    : tspan,
        'α_3_35' : α_model_3_35,
        'α_3_50' : α_model_3_50,
        'α_3_65' : α_model_3_65,
        't_4'    : tspan,
        'α_4_35' : α_model_4_35,
        'α_4_50' : α_model_4_50,
        'α_4_65' : α_model_4_65}

df = pd.DataFrame(dict)

# displaying the DataFrame
df.style
```

Out[7]:

	t_2	α_2_35	α_2_50	α_2_65	t_24	α_24_35	α_24_50	α_24_65	t_26	α_26_35	α_26_50	
0	0	[0.001]	[0.001]	[0.001]	0	[0.001]	[0.001]	[0.001]	0	[0.001]	[0.001]	
1	0.400267	[0.00515421]	[0.01244751]	[0.02813264]	0.400267	[0.00579261]	[0.01378763]	[0.0306895]	0.400267	[0.00614323]	[0.01451149]	[0.0
2	0.800534	[0.00722022]	[0.01757499]	[0.03977297]	0.800534	[0.008131]	[0.01947297]	[0.04336167]	0.800534	[0.00863009]	[0.02049794]	[0.04
3	1.2008	[0.00881461]	[0.02151324]	[0.0487066]	1.2008	[0.00993327]	[0.02383891]	[0.05310227]	1.2008	[0.01054597]	[0.02509476]	[0.05
4	1.60107	[0.01016184]	[0.02483462]	[0.05623857]	1.60107	[0.0114554]	[0.02752074]	[0.0613145]	1.60107	[0.01216374]	[0.02897117]	[0.06
5	2.00133	[0.01135027]	[0.02776144]	[0.06287464]	2.00133	[0.01279777]	[0.03076505]	[0.06854967]	2.00133	[0.01359027]	[0.03238686]	[0.07
6	2.4016	[0.01242565]	[0.03040784]	[0.06887426]	2.4016	[0.01401211]	[0.03369645]	[0.07509128]	2.4016	[0.01488068]	[0.03547523]	[0.07
7	2.80187	[0.01341491]	[0.03284168]	[0.07439158]	2.80187	[0.0151293]	[0.03639619]	[0.08110683]	2.80187	[0.01606778]	[0.03831545]	[0.08
8	3.20213	[0.01433616]	[0.03510719]	[0.07952705]	3.20213	[0.01616948]	[0.03890732]	[0.08670602]	3.20213	[0.01717302]	[0.04096919]	[0.09
9	3.6024	[0.01520169]	[0.03723512]	[0.08435043]	3.6024	[0.01714668]	[0.04126593]	[0.09196495]	3.6024	[0.0182113]	[0.04344234]	[0.09
10	4.00267	[0.01602061]	[0.03924784]	[0.08891254]	4.00267	[0.01807111]	[0.04349683]	[0.09693899]	4.00267	[0.0191935]	[0.04579103]	[0.10

Printed Values For plotting in Excel (predicted vs experimental):

In [9]:
```
print("")
print ('Predicted values for α:')
heading = ["2.4-35", "2.4-50","2.4-65", "2.6-35", "2.6-50", "2.6-65"]
time    = ["0", "30", "60", "90", "120", "240", "360"]

dataAdd = array([[interp(0  , tspan, ndarray.flatten(asarray(α_model_24_35))), interp(0  , tspan, ndarray.flatten(asarray(α_
                 [interp(30 , tspan, ndarray.flatten(asarray(α_model_24_35))), interp(30 , tspan, ndarray.flatten(asarray(α_
                 [interp(60 , tspan, ndarray.flatten(asarray(α_model_24_35))), interp(60 , tspan, ndarray.flatten(asarray(α_
                 [interp(90 , tspan, ndarray.flatten(asarray(α_model_24_35))), interp(90 , tspan, ndarray.flatten(asarray(α_
                 [interp(120, tspan, ndarray.flatten(asarray(α_model_24_35))), interp(120, tspan, ndarray.flatten(asarray(α_
                 [interp(240, tspan, ndarray.flatten(asarray(α_model_24_35))), interp(240, tspan, ndarray.flatten(asarray(α_
                 [interp(360, tspan, ndarray.flatten(asarray(α_model_24_35))), interp(360, tspan, ndarray.flatten(asarray(α_
display (pd.DataFrame(dataAdd, time, heading))
```

Predicted values for α:

	2.4-35	2.4-50	2.4-65	2.6-35	2.6-50	2.6-65
0	0.001000	0.001000	0.001000	0.001000	0.001000	0.001000
30	0.049407	0.119054	0.265377	0.052484	0.125336	0.277098
60	0.069865	0.168365	0.375299	0.074217	0.177249	0.391875
90	0.085564	0.206203	0.459645	0.090894	0.217084	0.479946
120	0.098800	0.238102	0.530752	0.104954	0.250666	0.554194
240	0.139720	0.336725	0.750597	0.148424	0.354494	0.783748
360	0.171120	0.412402	0.919289	0.181780	0.434165	0.959891

Appendix H

$[H^+]$ data plotted in Figure 25.

Table 15: $[H^+]$ data used for testing the acid concentration relationships (T = 65 °C).

Time (min)	$[H^+]_0$ (M)	$[H^+]$ (M)
12	2.00	1.81
22	2.00	1.76
40	2.00	1.78
120	2.00	1.05
150	2.00	0.89
200	2.00	0.66
15	3.00	2.65
33	3.00	2.44
70	3.00	2.11
100	3.00	1.78
230	3.00	1.11
8	4.00	3.82
20	4.00	3.46
60	4.00	3.21
95	4.00	2.71
130	4.00	2.32

Table 16: $[H^+]$ data over time at 65 °C for different initial acid concentrations.

	$[H^+]_0$				
Time (min)	2M	2.4M	2.6M	3M	4M
0	2.00	2.40	2.60	3.00	4.00
30	1.77	1.95	2.03	2.34	3.53
60	1.68	1.58	1.86	2.06	2.96
90	1.39	1.34	1.56	1.78	2.71
120	1.22	1.02	1.50	1.69	2.25
240	0.55	0.52	0.71	0.99	1.99
360	0.27	0.66	0.71	0.92	1.90